An in-depth investigation of an innovative internally channeled tube (ICT) heat exchanger design

zur Erlangung des akademischen Grades

DOKTOR DER INGENIEURWISSENSCHAFTEN (Dr.-Ing.)

der Fakultät für Maschinenbau

der Universität Paderborn

genehmigte

DISSERTATION

von

M. Sc. Abbas Jarullah Sangoor Al-Lami

aus Misan/ Irak

Tag des Kolloquiums: 23.10.2025

Referent: Prof. Dr.-Ing. habil. Eugeny Kenig

Korreferent: Prof. Dr.-Ing. habil. Andrea Luke

"Patience in times of hardship makes reward abundant"

Ali Ibn Abi Talib

Acknowledgment

I would like to express my deepest gratitude to all who have supported me during my doctoral journey

First and foremost, I extend my sincere appreciation to my supervisor, Prof. Eugeny Kenig, for his outstanding mentorship, unwavering encouragement, and invaluable feedback. His guidance has been instrumental not only in shaping this dissertation but also in fostering my academic and professional development. He granted me the freedom to explore my research with passion while providing thoughtful direction at pivotal moments. I am especially grateful for his compassion and support during periods when I faced health issues, particularly with my optic nerve, which affected my ability to work. His understanding and reassurance during these times are deeply appreciated.

I am also sincerely thankful to the German Academic Exchange Service (DAAD) for their generous financial support throughout my PhD. Their funding enabled me to dedicate myself fully to my research — without it, this achievement would not have been possible.

My sincere appreciation extends to Prof. Dr.-Ing. habil. Andrea Luke for kindly taking on the role of second reviewer of this dissertation. I am also grateful to Prof. Dr.-Ing. Volker Schöppner, chair of the examination board and to Prof. Dr. rer. nat. Tina Kasper for her valued participation as a committee member. Their time, thoughtful feedback, and constructive discussions have greatly enriched this work and broadened its perspective.

I am deeply appreciative of the Chair of Fluid Process Engineering (FVT) for providing a stimulating research environment, experimental facilities, essential resources, and numerous academic opportunities that have contributed significantly to the completion of this dissertation. I am especially grateful to Astrid Bongard from the secretary's office

for her tireless support with administrative tasks, procurement of laboratory equipment, and practical advice. Her assistance has been indispensable throughout this process.

My sincere thanks go to my colleagues at FVT in Paderborn for their collaboration and encouragement. I would also like to acknowledge Kai Ingo Overkott, Lukas Degner, and Elena Sabanov for their dedicated technical support, assistance in laboratory work, and their helpful cooperation throughout my research.

Finally, I dedicate this dissertation to my late parents. Their love, sacrifices, and unwavering belief in me have been the foundation of all that I have achieved. Though they are no longer with me, their influence remains a guiding force in my life.

To my beloved son, Yazen, your joyful spirit and irresistible sweetness have been a constant source of strength. And to my wife, Elaf Al-Hajjaj, thank you for your patience, encouragement, and support — you have been my anchor and driving force in bringing this work to completion.

Abbas Jarullah Sangoor Al-Lami

Paderborn, November 2025

Kurzfassung

Der Internally Channeled Tube (ICT)-Wärmeübertrager ist ein neuartiges Designkonzept mit speziell gestalteten, gekrümmten Kanälen innerhalb eines zylindrischen Rohrs, das eine isolierte Außenfläche aufweist. Das ICT-Konzept deutlich erhöht die Wärmeübertragungsfläche zwischen Fluiden, verbessert die thermische Leistung und ermöglicht eine kompakte Bauweise, die ideal für platzsparende Installationen ist.

Es werden zwei innovative ICT-Designs untersucht, die jeweils sechs innere Kanäle in einem Rohr mit einem Durchmesser von 4 cm und einer Länge von 1 m aufweisen. Die Kanalgeometrien der ICTs werden mithilfe spezieller Kurvenfunktionen erzeugt. Strömungsdynamik und Wärmeübertragung in ICT-Wärmeübertragern werden durch dreidimensionale Computational Fluid Dynamics (CFD)-Simulationen erfasst, die die Einphasenströmung und den konjugierten Wärmeübergang unter turbulenten und laminaren Strömungsbedingungen beschreiben.

Die CFD-Simulationen werden anhand experimenteller Daten aus speziell gebauten Testeinrichtungen validiert. Die validierten numerischen Ergebnisse werden verwendet, um Auslegungsgleichungen für Druckverlust und Wärmeübertragung in den ICT-Kanälen für turbulenter erzwungener Konvektion zu entwickeln.

Abstract

The Internally Channeled Tube (ICT) heat exchanger is a novel design concept featuring specially designed curved channels within a circular tube that has an insulated exterior surface. The ICT concept significantly increases the heat transfer surface area between fluids, improving thermal performance and enabling a compact structure ideal for space-constrained installations.

Two innovative ICT designs are studied, each featuring six internal channels inside a tube that is 4 cm in diameter and 1 m in length. The channel geometries of ICTs are generated using special curve functions. The fluid dynamics and heat transfer in ICT heat exchangers are resolved using three-dimensional Computational Fluid Dynamics (CFD) simulations, which describe single-phase flow and conjugate heat transfer under turbulent and laminar flow conditions.

The CFD simulations are validated against experimental data obtained from purpose-built testing facilities. The validated numerical results are subsequently used to develop design methods for pressure drop and heat transfer characteristics in the ICT ducts for turbulent forced convection.

List of Publications

Journal articles

A.J.S. Al-Lami, V. Inguva, E.Y. Kenig, Numerical analysis of conjugate heat transfer within internally channeled tubes, Appl. Therm. Eng. 223 (2023). 119596. https://doi.org/10.1016/j.applthermaleng.2022.119596

A.J.S. Al-Lami, E.Y. Kenig, Experimental study of an internally channeled tube heat exchanger under turbulent flow conditions, Int. J. Heat Mass Transf. 214 (2023). 124425. https://doi.org/10.1016/j.ijheatmasstransfer.2023.124425

A.J.S. Al-Lami, E.Y. Kenig, New pressure drop and heat transfer correlations for turbulent forced convection in internally channeled tube heat exchanger ducts, Case Stud. Therm. Eng. 54 (2024). 103993. https://doi.org/10.1016/j.csite.2024.103993

A.J.S. Al-Lami, E.Y. Kenig, Investigation of fluid flow and heat transfer characteristics of an internally channeled tube heat exchanger under laminar flow conditions, Energies. 17 (2024). 17112637. https://doi.org/10.3390/en17112637

Conference contributions

A.J.S. Al-Lami, E.Y. Kenig, Heat transfer enhancement within internally channeled tubes, ACHEMA Pulse, online event, June 2021.

A.J.S. Al-Lami, E.Y. Kenig, Heat transfer enhancement within internally channeled tubes, Annual Meeting on Reaction Engineering and ProcessNet Subject Division Heat and Mass Transfer, Würzburg, July 2022.

Contents

List of Figures

List of Tables

Nomenclature

Latin Symbols

Symbol	Description	Units
A	area	m^2
a,b,c,e,s	geometrical parameters of ICT ducts	m
c_p	specific heat	$J\,kg^{-1}\,K^{-1}$
D	diameter	m
d_1	inner tube diameter	m
d_2	outer tube diameter	m
d_{co1}	inner diameter of core tube in DPHE	m
d_{co2}	outer diameter of core tube in DPHE	m
f	friction factor	–
$\vec{f}$	external force per unit volume.	Nm^{-3}
g	acceleration of gravity	ms^{-2}
h_{avg}	average heat transfer coefficient	$W\,m^{-2}\,K^{-1}$
k	turbulence kinetic energy	$J\,kg^{-1}$
l	length	m
$\dot{m}$	mass flow rate	kg s^{-1}
Nu	Nusselt number	–
P	perimeter	m
p	pressure	pa
Pr	Prandtl number	–
Pr_t	turbulent Prandtl number	–

Q	heat flow rate	W
q	heat flux	$W\ m^{-2}$
Re_h	Reynolds number based on hydraulic diameter	–
S	heat source	J
t	time	s
T	temperature	K
T_R	first set temperature for cold fluid in RE	K
T_L	first set temperature for hot fluid in LE	K
$\vec{\boldsymbol{v}}$	velocity vector	$m\ s^{-1}$
$\dot{V}$	volumetric flow rate	$m^3\ s^{-1}$
u	velocity	$m\ s^{-1}$
u_τ	shear velocity	$m\ s^{-1}$
u^+	dimensionless velocity vector	–
$\dot{W}$	overall pumping power	W
y^+	dimensionless wall coordinates of first layer	–
$\tilde{y}$	coordinate normal to the wall	m
x,y,z	cartesian coordinate	m

Greek symbols

Symbol	**Description**	**Units**
β	aspect ratio	–
δ	internal wall thickness	m
Δp	pressure drop	Pa
ϵ	dissipation rate	m^2/s^2
$\dot{\boldsymbol{\varepsilon}}$	thermo-hydraulic efficiency	–
λ	thermal conductivity	$W\ m^{-1}\ K^{-1}$
λ_{eff}	effective thermal conductivity	$W\ m^{-1}\ K^{-1}$
μ	dynamic viscosity	$Pa\ s$
μ_t	turbulent viscosity	$kg\ m^{-1}\ s^{-1}$
ν	kinematic viscosity	$m^2\ s^{-1}$
ρ	density	$kg\ m^{-3}$
τ_w	wall shear stress	Pa

Subscripts

Symbol	**Description**
b	bulk
cr	core region
ch	channel
cs	cross-section
e	equivalent
f	fluid
h	hydraulic
w	wall
m	mean value

Abbreviations	**definition**
DPHE	double pipe heat exchanger
ICTs	Internally channeled tubes
RE	right element
LE	left element
ME	middle element
PEC	performance evaluation criterion
CFD	computational fluid dynamics
HVAC	Heating, ventilation, and air conditioning

Terms	**definition**
ICT1	first design of ICTs
ICT2	second design of ICTs
duct	either core region or channel of the ICTs

1 Introduction

Heat exchangers are essential devices that enable the transfer of thermal energy between liquids and gases. They are crucial in a wide range of industrial processes, heating and cooling systems, and power generation applications. Heat exchangers are extensively employed in various industrial and domestic settings, including refrigeration, heating, steam condensation, and liquid evaporation in power plants, chemical processing, and waste heat recovery (Balaji et al., 2020).

Commonly heat exchangers with a high level of efficiency are required. Such efficiency is usually achieved by increasing exchanger size to reach a sufficient heat transfer area (Afgan & Da Graça Carvalho, 2000). However, a decision to make a heat exchanger bigger should be based on the specific requirements of the application and the trade-offs between improved heat transfer efficiency and the associated drawbacks. Increased costs and limited installation space are examples of such drawbacks (Mehendale, 2018). Furthermore, a larger heat exchanger may experience greater heat losses to the environment, particularly when insulation is inadequate, due to the increased surface area exposed to the surroundings (Savaş & Kocabas, 2022).

Among various applications for heat exchangers, those used in waste heat recovery systems—for high or low temperatures—are crucial components (Stehlik & Jegla, 2020). In such systems, there is a need for heat exchangers with a substantial heat transfer area or more efficient exchanger (Jouhara et al., 2018). Figure 1.1 shows a schematic of a typical waste heat recovery system utilizing ORC cycle. The primary function of heat exchangers in waste heat recovery is to efficiently capture and transfer thermal energy from high-temperature sources, such as hot flue gas or hot liquids encountered in industrial processes or exhaust gases emitted by engines (Stehlik & Jegla, 2020). This energy is then transferred

to another medium, usually a fluid like water or air, which can be employed for various practical applications such as electric power generation (Wehbi et al., 2023). Heat exchangers can also significantly contribute to emissions reduction in waste heat recovery systems. The cooling of hot steam, for example, can facilitate the solidification or conversion of harmful substances like carbon dioxide, methane, and polyfluoroalkyl compounds, thus making their removal from the system easier (Legros et al., 2014).

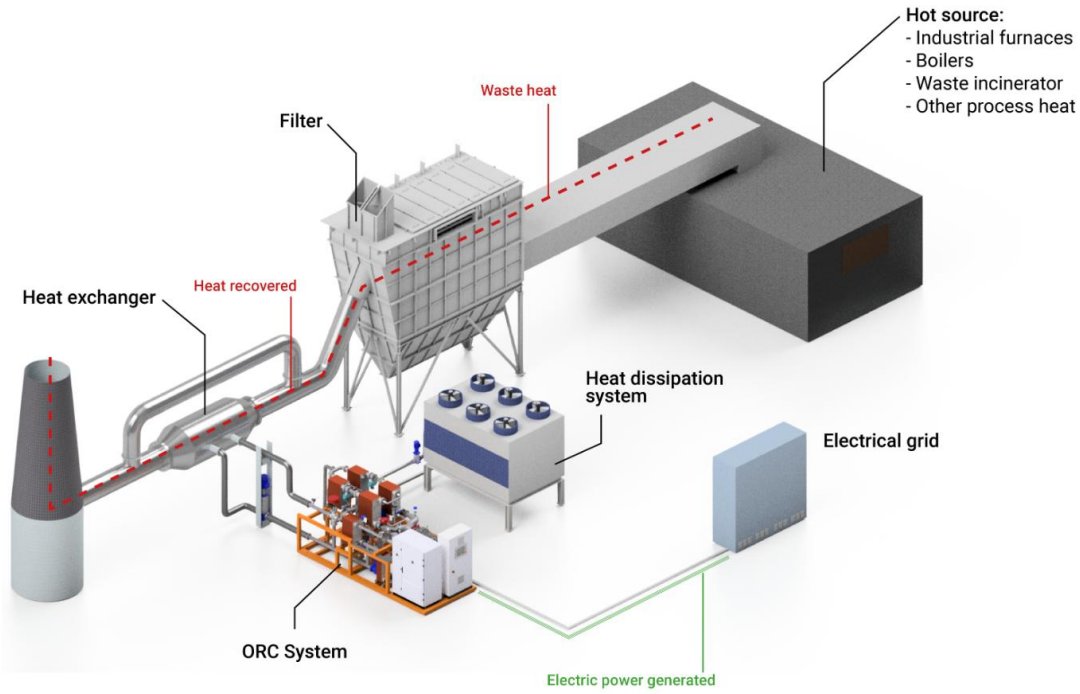

Figure 1.1: A typical schematic of waste heat recovery system (Zuccato Energia, accessed 10.04.2024).

Additionally, heat exchangers are widely used in a variety of other industrial settings, including chemical production plants and refineries (Reppich, 1999). They play an essential role in these settings by supporting critical processes. For instance, in a refinery, heat exchangers are integrated in processes to convert crude oil into valuable products like gasoline, diesel, and jet fuel (Jokar et al., 2016). These essential devices play a crucial role in the distillation process, where crude oil is separated into various components based on their boiling points. Heat exchangers enable precise temperature control during distillation, ensuring optimal separation and product quality (Luyben, 2018). Figure 1.2 shows a photo of large-scale tubular heat exchangers at an oil refinery.

Furthermore, heat exchangers in chemical production plants enhance safety by efficiently dissipating excess heat generated during chemical reactions. This not only prevents equipment overheating but also minimizes the risk of accidents (Vakylabad, 2023).

Figure 1.2: A photo of large-scale heat exchangers in an oil refinery (Torq N Seal Plugs, accessed 15.04.2024).

A further application of heat exchangers can be found in solar systems where heat exchangers transfer heat from solar collectors to working fluids such as water or antifreeze (Al-Mamun et al., 2023). This heat is used to provide energy for heating purposes. Such applications mostly require using highly efficient heat exchangers to ensure maximum utilization of solar energy (Mridha & Hasanuzzaman, 2022). Therefore, advancements in heat exchanger design can be essential for unlocking the full benefits of solar energy in various applications.

1.1 Motivation and structure of the dissertation

The motivation behind this research is to develop a more efficient and compact heat exchanger design. Current high-efficiency heat exchangers often face limitations, either

being too large for compact installation spaces or insufficiently sized to provide adequate heat exchange. Additionally, many enhancement techniques for traditional exchangers are difficult to implement and often come with significant drawbacks, including high-pressure requirements, fouling, increased costs, and added complexity. To address some of these challenges, this research introduces a novel design concept so-called the internally channeled tube (ICT) heat exchanger. The ICT concept is based on the channels-in-tube principle, using curved channels. This design can increase the heat transfer surface area, thereby enhancing the heat transfer rate while maintaining a compact configuration.

In the initial phase of this study, Computational Fluid Dynamics (CFD) simulations, a widely recognized and effective technique, were used to evaluate heat transfer and pressure drop in the ICT heat exchanger. However, the large computational domains associated with this technique can result in substantial computational expenses and extended processing times. To overcome this issue, a novel method was introduced to subdivide the large computational domain into smaller, more manageable elements. This domain-subdivision or splitting method can reduce the computational requirements per element when using a cluster or a local computer. In the subsequent phase, new experimental setups were developed to validate the CFD results, ensuring their reliability and accuracy. Furthermore, novel correlations for pressure drop and heat transfer were established due to the lack of existing correlations for the ICT exchanger design. These correlations can provide valuable data for design optimization, offering insights into heat transfer and fluid flow behavior in ICT heat exchangers. They are particularly useful in cases where experimental data is not readily available or feasible to obtain.

The dissertation is structured into eight chapters, each addressing a key aspect of the research. The introduction offered an overview of heat exchangers and their significance in industrial applications. **Chapter 2** follows, providing a comprehensive discussion of existing heat exchanger designs, enhancement techniques, and their performance limitations. This chapter also establishes the research gap and justifies the need for the proposed study.

Chapter 3 presents the fundamental principles governing heat transfer and fluid dynamics, including the mass, momentum, and energy conservation equations. It also describes turbulence modeling, conjugate heat transfer, and the computational approach adopted for simulating ICT heat exchangers. **Chapter 4** defines the ICT concept,

highlights key design considerations, and establishes the methodology for calculating geometrical parameters. The subsequent **Chapter 5** includes both numerical and experimental analyses. It describes the computational domains, boundary conditions, and meshing techniques used in CFD simulations, while also detailing the experimental setup, measurement procedures, and the validation process against numerical results. **Chapter 6** evaluates the thermal-hydraulic performance and economic feasibility of ICT heat exchangers compared to traditional designs.

Chapter 7 presents design methods developed for ICT. It examines the impact of duct geometry on fluid flow and heat transfer characteristics and provides correlations for performance prediction and optimization. Finally, **Chapter 8** concludes with a summary of the research findings and offers recommendations for future research endeavors.

2 Literature review

This chapter provides an overview of the current state of the art in heat exchangers, exploring their operational principles and classifications. It highlights the significant contribution of exchangers to various industrial applications. Furthermore, the chapter reviews various enhancement techniques focused on improving heat transfer efficiency, including those used in double-pipe heat exchangers, with particular emphasis on passive techniques.

2.1 Heat exchangers

The functionality of heat exchangers is based on the fundamental principles of heat transfer through conduction, convection, and radiation. Heat exchangers operate by facilitating the transfer of thermal energy between two or more fluids, which are typically at different temperatures. The fluids, which could be gases, liquids, or a combination of both, commonly pass through separate channels or ducts, recognized as the "hot side" and the "cold side." This process allows heat to flow from the hotter fluid to the cooler one through the walls of the channels, where heat transfer occurs through conduction. In addition to conduction, heat is often transferred by convection, in which fluid motion enhances the heat exchange process. In some cases, heat may transfer directly without a wall or barrier. Radiation may also play a role, depending on the design and the temperature differences between the fluids. These principles work together to enable heat transfer, either to heat or cool the fluids depending on the purpose of a system.

Heat exchangers can generally be categorized into two main types based on their function and construction: regenerative and recuperative, as summarized in Figure 2.1. Regenerative heat exchangers feature a single flow path through which hot and cold fluids

alternate. These exchangers can function in both static and dynamic modes. In static regenerative heat exchangers, the direction of fluid flow is periodically reversed to realize the transfer of heat (Ackermann, 1997). While dynamic regenerative heat exchangers involve a rotating or oscillating mechanism to achieve better thermal performance (cf. Figure 2.2) (Herraiz et al., 2015). Regenerative heat exchangers are commonly used for energy recovery, especially in buildings with high ventilation requirements and in gas turbine systems to preheat the air entering the turbine (Kanaś et al., 2022).

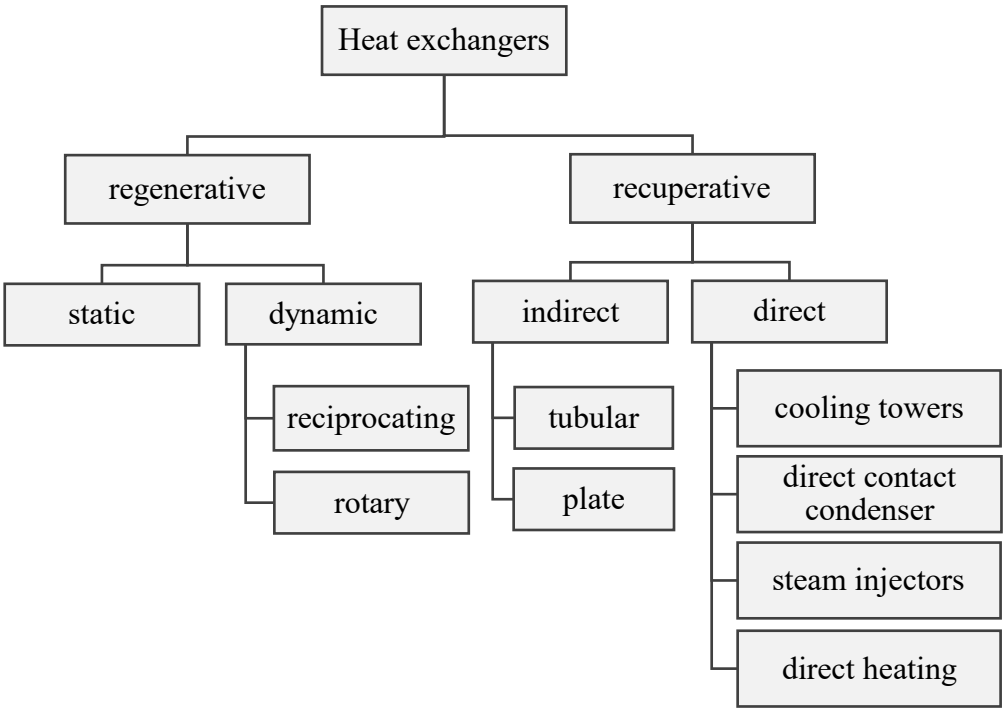

Figure 2.1: Heat exchanger classifications by construction (Brogan, 2011).

In contrast, recuperative heat exchangers involve two distinct fluid streams traveling along separate paths. Some of these heat exchangers feature a barrier that divides two flow channels, realizing an indirect interaction between the fluids (Brogan, 2011). Common examples include tubular and plate heat exchangers. Besides, recuperative heat exchangers can be based on direct contact between the fluids, as observed in applications such as cooling towers (Hensley, 2009).

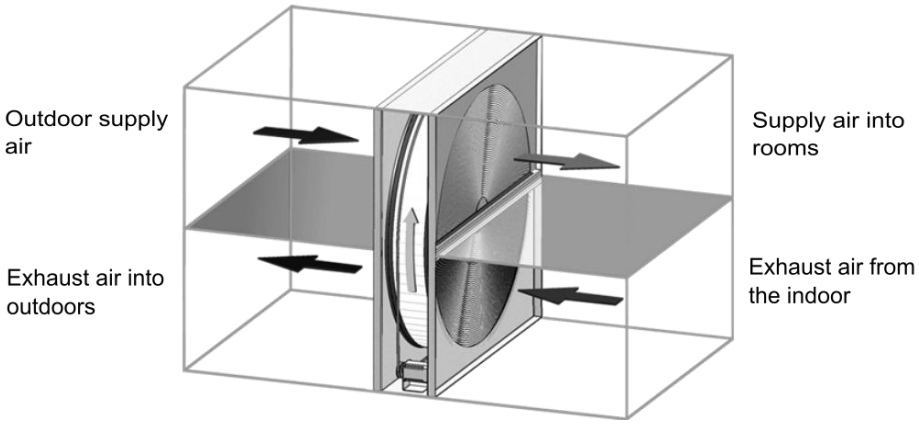

Figure 2.2: Schematic of a rotary regenerative heat exchanger used in HVAC systems (Komfovent., accessed 28.02.2025).

The right heat exchanger choice between a regenerator and a recuperator is based on key considerations including efficiency, costs, maintenance, and compatibility with industrial applications. Regenerators are more efficient due to their ability to store heat, making them ideal for processes with short-term operation, while this comes with greater complexity and higher potential costs. Recuperators, by contrast, offer simpler designs with lower initial costs and easier maintenance but they can be less efficient in applications where heat storage is significant (Kanaś et al., 2022).

Recuperative heat exchangers are more commonly used for the reasons mentioned earlier and are widely applied across various industries. Among the most common designs employed are shell-and-tube and plate heat exchangers. Shell-and-tube heat exchangers consist of multiple tubes housed within an outer shell. One fluid, known as the tube-side fluid, flows through the tubes, while the other fluid, referred to as the shell-side fluid, circulates around the tubes within the shell (Parisher & Rhea, 2022), as illustrated in Figure 2.3 (left). These exchangers are highly versatile and well-suited for handling significant pressure and temperature differences.

On the other hand, plate heat exchangers are constructed using a series of thin metal plates building small channels for fluid flow. These plates are stacked together and firmly pressed, creating alternating channels for hot and cold fluids (cf. Figure 2.3 (right)). Plate heat exchangers are prized for their high heat transfer efficiency, and ease of maintenance (Reppich, 1999).

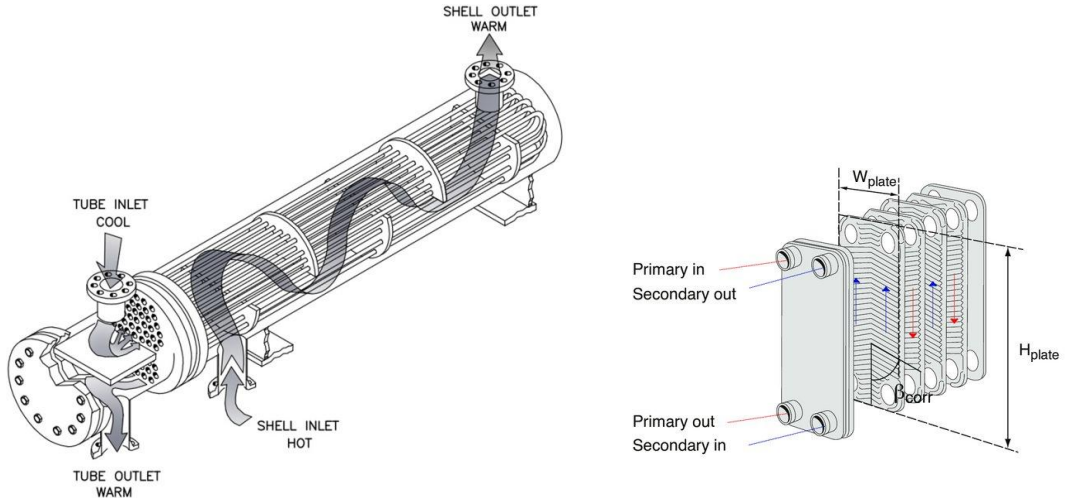

Figure 2.3: Recuperative heat exchangers (indirect type); internal view of shell and tube exchanger (left) (Parisher & Rhea, 2022); plate heat exchanger configuration (right) (Zehnder, 2004).

A further common type of recuperative heat exchanger is the traditional double-pipe heat exchanger (DPHE), a simplified version of the shell-and-tube heat exchanger (cf. Figure 2.4). The DPHE design consists of two pipes positioned concentrically, one inside the other (Forsberg, 2021). Its primary function is to enable heat exchange between two fluids, utilizing a simple and efficient operating mechanism. One of the fluids flows through the inner tube, while the other circulates through the annulus which is the space between the inner and outer pipes. Due to their durability and simplicity in transferring heat, double pipe heat exchangers are used in a wide variety of industrial and HVAC applications (Ghani et al., 2018). Most of its applications are in petrochemical processing, particularly in refineries for operations such as crude oil distillation and heat recovery. These processes involve regulating temperature during heating or cooling reactive chemicals (Coker, 2023). Double pipe heat exchangers are also used in solar thermal systems to transport thermal energy from solar collectors to water or other heat transfer fluids (Templeton et al., 2016). Furthermore, it is employed in HVAC to regulate the temperature of the air pumped in buildings through air conditioning systems (Ghani et al., 2018).

The suggested innovative design ICT heat exchanger closely resembles the double-pipe heat exchanger (DPHE) in design and functionality, primarily due to their shared

single outer pipe. Consequently, the DPHE serves as the reference design in this study to systematically assess and benchmark the performance of ICT heat exchangers.

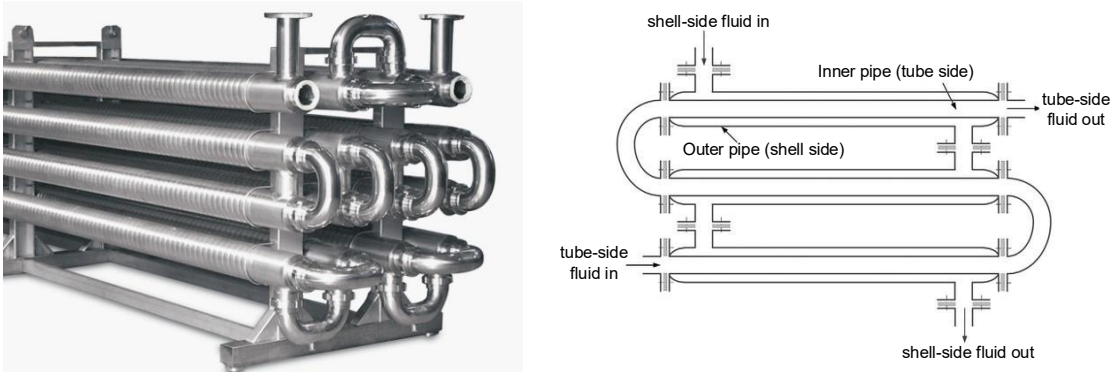

Figure 2.4: Double pipe heat exchanger: a photo of DPHE (left) (Teralba Industries, accessed 06.05.2024); a schematic representation of the DPHE configuration (right) (Hanshik et al., 2016).

2.2 Enhancement techniques in DPHE design

Global concerns about energy sustainability have led to a growing interest, both in industry and in academia, in energy savings based on heat transfer enhancement techniques (Jing et al., 2020). Such techniques have become increasingly attractive in a wide variety of applications related to the automotive and process industries and the energy sector (Maradiya et al., 2018).

Numerous studies have been conducted over the years to enhance heat exchanger performance, particularly through design modifications. These studies often focus on optimizing the geometry of heat exchangers—such as pipe arrangements, fin structures, and surface enhancements—to improve heat transfer efficiency. For example, the use of coiled, finned, and corrugated tubes in double pipe heat exchangers and wavy and dimpled surfaces in plate and pillow-plate heat exchangers has been suggested and examined (Maradiya et al., 2018; Piper et al., 2019). Compact designs are also explored to reduce the size of exchangers without compromising performance (Hesselgreaves, 2001). Heat exchangers used in low-temperature waste heat recovery, for instance, often require large transfer areas, leading to bulky equipment (Jouhara et al., 2018). Therefore, enhancing performance can allow for size reduction (Balaras, 1990), leading to significant savings in energy, materials, space, and costs (Zhang et al., 2019).

The most common method for enhancing heat transfer in heat exchangers is through the use of so-called passive techniques. This method improves heat transfer performance without the use of external power input. The techniques typically involve modifications to the heat exchanger design or the fluid flow that increase the surface area for heat transfer or induce turbulence, thereby reducing thermal resistance and enhancing heat exchange efficiency (Liebenberg & Meyer, 2007; Maradiya et al., 2018). Unlike active techniques that require external energy sources, passive methods are more energy-efficient and cost-effective (Mousa et al., 2021).

Increasing the heat transfer area between the hot and cold fluids is a promising way to enhance thermal performance of heat exchangers, and there are a variety of corresponding techniques available. Using finned walls is a common way in double-pipe heat exchangers (DPHE), as internally finned ducts or pipes result in a relatively larger heat transfer area and improved thermal efficiency. Duan et al. (2018) carried out experimental and numerical studies on DPHE with blossom-shaped internal fins in the annulus region, as shown in Figure 2.5a. With rising number of such fins, the wetted perimeter of the internally finned annulus region increases, resulting in a larger heat transfer area in the annulus region. However, these studies also showed a large pressure drop in the finned region.

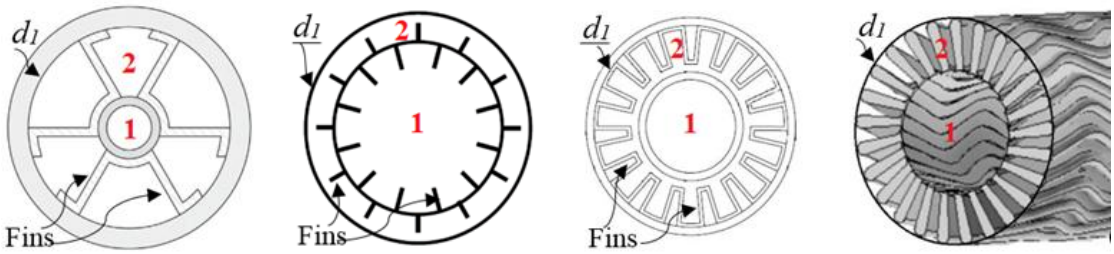

(a) (b) (c) (d)

Figure 2.5: Finned tube enhancement techniques in DPHE, adjusted from (Wang et al., 2008; Rao & Levy, 2008; Duan et al., 2018): blossom-shaped fins (a), plain fins in both regions (b), internal longitudinal fins (c), streamwise wavy fins (d): 1 - the inner pipe; 2 - the annulus region.

Further improvements can be achieved by adding fins, both to the inner tube and to the annulus region, as proposed by Rao and Levy (2008). This can result in a significant improvement in heat transfer rate as a result of expanding the heat transfer surface area (cf.

Figure 2.5b). Along with adding fins, heat transfer area can be significantly expanded when the fin height increases. By utilizing plain longitudinal fins shown in Figure 2.5c, Ma et al. (2010) proposed a design that extends fins and reduces the gap between the fin tip and the outer surface of the inner tube, thereby increasing the surface area of the annulus. It was found that heat transfer is enhanced as the gaps are reduced whereas wider gaps result in high pressure drop and pump costs.

Instead of plain fins, Wang et al. (2008) placed streamwise wavy fins in the annulus region, as illustrated in Figure 2.5d. Compared to plain fins, streamwise wavy fins improve heat transfer more efficiently. A larger wave height expands the heat transfer area within the annulus, which results in a higher heat transfer coefficient. Furthermore, with a wavy surface, fluid flow direction can be manipulated resulting in stronger turbulence. The surface curvature may result in eddy formation in a turbulent flow along a channel with a periodic wavy surface. This can disturb the boundary layer and enhance heat transfer. The flow over this fin type, however, results in a high friction factor. Liu and Jensen, (2001) investigated the heat transfer and resistance characteristics of three fin profiles - rectangle, triangle, and round crest. They found that fins of the first two types had similar characteristics, whereas turbulence was reduced with the third type. With a taller fin, more heat transfer area is added, improving the interaction between the fin tip and the fluid flow.

Another effective method to improve heat transfer in exchangers involves modifying duct shape. For instance, corrugated surfaces with transversal and cross-helical patterns in circular tubes were found to provide improvements in thermal efficiency (Azam et al., 2023). Experimental and numerical studies were conducted in Refs. (Rozzi et al. (2007); Harleß et al. (2017); Wang et al. (2018)) to examine the effects of different geometrical parameters on temperature and flow fields in circular tubes with corrugated surfaces under turbulent flow conditions (cf. Figure 2.6). The studies demonstrated that corrugated tube heat exchangers transfer heat at significantly higher rates than conventional heat exchangers with flat tube surface. Main flows in corrugated channels are accompanied by secondary flows, which provide stronger mixing of fluids. Moreover, corrugated walls may result in larger heat transfer surface areas (Navickaitė et al., 2019).

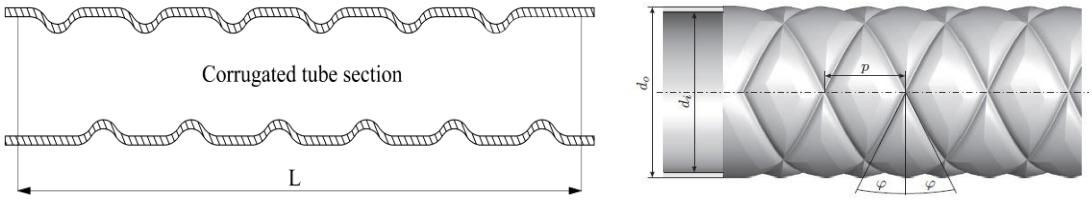

(a) (b)

Figure 2.6: Schematics of corrugated tubes: transversal and helical corrugated tube surface (a) (Wang et al., 2018); cross-corrugated tube: inner and outer diameter d_i and d_o, corrugation angle φ, and corrugation pitch p (b) (Harleß et al., 2017).

A further way that can increase the heat transfer area and initiate turbulence in the fluid flow is based on twisted geometries, such as twisted tubes or, alternatively, twisted tape inserts within cylindrical tubes or square ducts. The latter method was investigated in a number of studies. Experiments were conducted in (Eiamsaard et al. (2006); Sivashanmugam and Suresh (2007); Promvonge et al. (2014); Yang et al. (2020)) to analyze the effect of twist ratio of twisted tapes on heat transfer augmentation (cf. Figure 2.7). The results of these studies indicate that a significant enhancement of heat transfer rate is accompanied by an increase in pressure drop. The increase in heat transfer rate and pressure drop is explained by swirling flow caused by secondary flows. Rahimi et al. (2009) examined four types of twisted tapes, namely simple twisted tapes, perforated twisted tapes, notched twisted tapes, and jagged twisted tapes. As in the jagged type, the edge of the twisted tape is cut and warped upward, this results in a more intensive turbulence generation in the flow and, consequently, in higher Nusselt numbers than for other types. The twisted insert techniques were also applied to improve heat transfer under laminar flow conditions. A numerical investigation was carried out by Feng et al., (2017) to evaluate the influence of wire coil inserts on laminar flow in a rectangular microchannel at Reynolds numbers ranging from 200 to 1400. They showed that these inserts effectively enhance heat transfer, particularly at lower Reynolds numbers. Furthermore, the wire coil or twisted tape inserts are commonly demonstrated in a number of publications (e.g., Refs. [García et al. (2005); Saha and Saha (2010); Esmaeilzadeh et al. (2014); Kadam et al. (2022)] as an effective method of improving thermal performance within laminar flow.

The combination of multiple enhancement techniques is another approach. For instance, achieving a dual enhancement effect can be accomplished by employing both

twisted inserts and rough wall. Zhang et al. (2012) examined the turbulence generation in finned wall tubes and continuous twisted-tape inserts. They found that heat transfer and flow characteristics show clearly higher improvement with the combined technique than with finned walls only. Experiments were carried out by Pal and Saha (2015) using a circular duct with viscous oil under laminar flow conditions by incorporating both spiral rib and twisted tape with oblique teeth. The results revealed a significant improvement in performance compared to the variant with only a single enhancement technique.

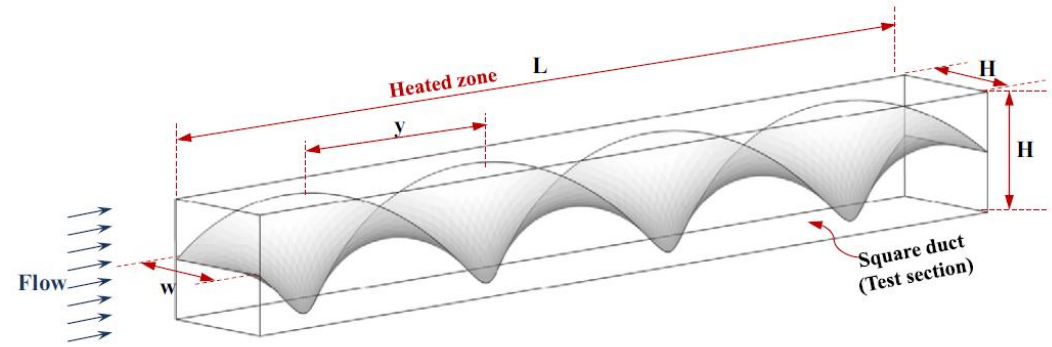

(a)

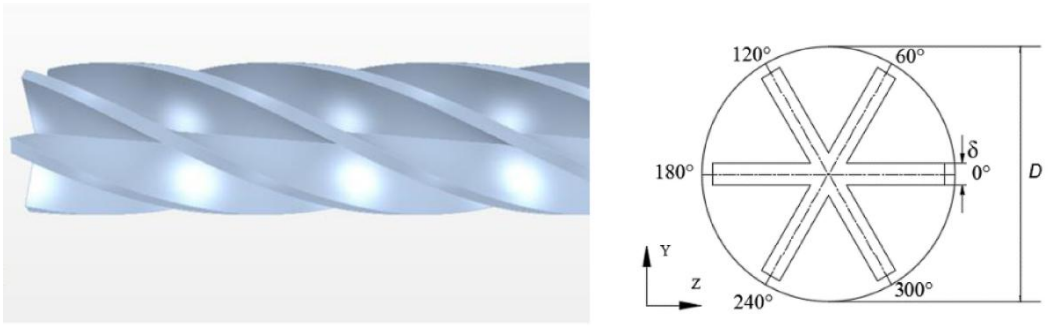

(b)

Figure 2.7: Twisted tape inserts: twisted tape within square duct (Promvonge et al., 2014) (a); cross-section view of the tubes with coaxial cross triple twisted tape (Yang et al., 2020) (b).

2.3 Conclusions and objectives

Efficient thermal management is crucial in optimizing energy systems, with heat exchangers serving as key components in this process. These devices operate based on the principles of conduction, convection, and radiation to facilitate heat transfer between

fluids. The classification of heat exchangers into regenerative and recuperative types highlights their varied operational modes and construction, offering a deeper understanding of their functionality.

Several enhancement techniques for traditional heat exchangers, including fin addition, duct shape modification, and twisted geometries, have been effective methods in improving the heat transfer rate. Optimized designs of heat exchangers further contribute to reduced energy consumption, lower material costs, and the promotion of environmentally sustainable solutions. However, the application of these techniques across different heat exchanger types, such as double pipe heat exchangers, reveals inherent limitations. Enhancements involving wire coils and twisted inserts, while promising, often lead to increased fouling susceptibility, necessitating more frequent maintenance or replacement. Furthermore, approaches to increase heat transfer area are predominantly confined to single-channel flows, and modifications to the fluid-fluid interface remain minimal. Consequently, these methods may not consistently yield substantial improvements in heat transfer rates, highlighting the need for innovative heat exchanger designs or more comprehensive enhancement methods.

The internally channeled tube (ICT) heat exchanger presents a novel approach to address some of the persistent challenges associated with traditional exchangers and thermal optimization techniques. This innovative design offers the potential to substantially increase the heat transfer area between the two fluids in contact, leading to significant improvements in heat transfer rates while maintaining a compact overall structure. The ICT configuration consists of two distinct flow regions—the core region and the channels—arranged within an insulated tube (cf. Figure 2.8). In this arrangement, a hot fluid flows through the core region, while a cold fluid flows countercurrently through the channels, enabling efficient heat exchange between the two fluids.

The ICT concept introduces new design configurations that require systematic investigation to fully realize its potential. In particular, this research aims to address the following objectives:

- Establishing a parametric design framework for ICT using mathematical curve functions to define channel profiles. This framework enables precise determination of complex geometrical parameters (e.g., hydraulic diameter,

cross-sectional asymmetry) and ensures adaptability for customization, scalability, and iterative design refinement.

- Developing a comprehensive numerical model to simulate the thermal-hydraulic behavior of the ICT heat exchanger, forming the basis for performance assessment.
- Exploring experimental approaches to investigate flow maldistribution and flow type characterization in ICT ducts—key aspects often overlooked in conventional studies of traditional designs—in order to address their impact on fluid dynamic and thermal efficiency.
- Developing novel experimental set-ups to investigate the thermal-hydraulic performance of the ICT heat exchanger, thereby providing empirical validation for the CFD models employed.
- Conducting a comparative study between the ICT heat exchanger and a conventional reference design to evaluate economic feasibility and highlight key performance metrics.
- Formulating novel design methods for predicting pressure drop and heat transfer characteristics in ICT heat exchangers, enabling design optimization and practical applications.

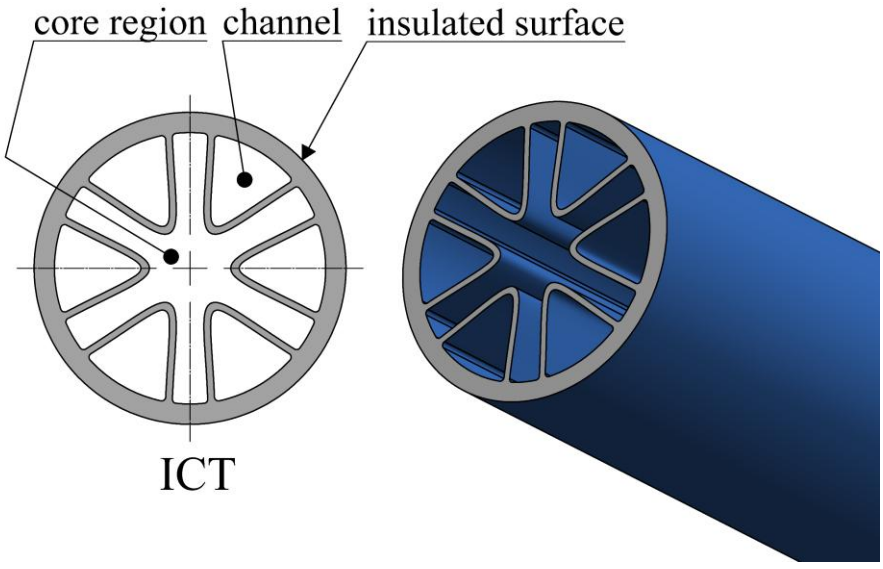

Figure 2.8: Cross-sectional view of the internally channeled tube (ICT).

3 Theoretical background and CFD modeling

This chapter presents the essential theoretical background of Computational Fluid Dynamics (CFD), a numerical method to solve the conservation equations for mass, momentum, and energy. Such solutions enable quantitative predictions of fluid flow and heat transfer phenomena. In this study, CFD techniques were applied to simulate fluid flow in the ICT heat exchangers under both laminar and turbulent conditions. An appropriate turbulence model was implemented to accurately capture turbulent characteristics when applicable. The chapter details the governing equations, modeling approaches, and numerical techniques used in this analysis.

3.1 Governing equations of fluid flow

The generic transport equation, also known as the convection-diffusion equation or scalar transport equation, is a fundamental mathematical model used to describe the transport of a scalar quantity in a fluid. It provides a unified framework for analysing the conservation of different quantities, including mass, momentum, and energy (Anderson, 2010). It is widely used in various fields of science and engineering (Zohuri, 2017). The generic equation accounts for temporal changes, convection, diffusion, and sources or sinks of the transported quantity, offering a versatile tool for simulating and understanding physical processes (Bird et al., 2007). The differential form of the generic transport equation can be written as follows:

$$\frac{\partial \phi}{\partial t} + \nabla \cdot (\phi \vec{v} + \mathcal{F}) - S = 0 \tag{3.1}$$

Here, ϕ represents any transported scalar quantity within a control volume, such as mass concentration, energy, or temperature. $\vec{v}$ is the velocity vector, $\mathcal{F}$ is the flux of ϕ, and S includes source or sink terms. The first term on the left-hand side (LHS) of Eq. (3.1) represents the rate of change of the transported quantity within a control volume, while the second term quantifies the convective transport due to fluid motion. The third term accounts for diffusive flux of ϕ, and the last term represents the generation or destruction of the transported quantity within the control volume.

3.1.1 Mass conservation equation

The principle of mass conservation, one of the fundamental laws of physics, states that mass can neither be created nor destroyed within a closed system. In fluid dynamics, this principle is mathematically expressed through the continuity equation, which ensures that the rate of mass change within a control volume equals the net mass flow across its boundaries. This equation can be derived by substituting $\phi = \rho$ (where ρ is the density, representing the amount of mass per unit volume), $\mathcal{F} = 0$ (since mass flux can only change due to transport), and S =0 (indicating that mass cannot be created or destroyed) into the general transport equation Eq. (3.1):

$$\frac{\partial \rho}{\partial t} + \nabla \cdot (\rho \vec{v}) = 0 \tag{3.2}$$

For steady-state and incompressible flows, the fluid density remains constant (ρ = constant) across the fluid domain. As a result, the time derivative term on the left-hand side (LHS) of Eq. (3.2) vanishes, simplifying the continuity equation:

$$\nabla \cdot (\rho \vec{v}) = 0 \tag{3.3}$$

For constant density flows, this can be further simplified to:

$$\nabla \cdot \vec{v} = 0 \tag{3.4}$$

This equation essentially states that the divergence of the velocity field must be zero, ensuring fluid flow conservation in any infinitesimal control volume. The continuity equation serves as a constraint on the velocity field and must be satisfied simultaneously with the momentum and energy equations to obtain physically realistic solutions in CFD simulations.

3.1.2 Momentum conservation equation

The motion of fluid particles is governed by Newton's second law of motion, which relates the rate of change of momentum to the forces acting on the fluid. In fluid dynamics, this principle leads to the momentum conservation equation. This equation accounts for various quantities including pressure gradients, viscous effects, and external forces, providing a description of fluid behavior.

Momentum conservation equation can be derived from the generic transport equation in the same way as continuity equation. However, momentum is a vector field, with the amount of momentum per unit volume expressed as $\phi = \rho\vec{v}$. Stress, defined as force per unit area (σ), can be viewed as a flux of force or $\mathcal{F} = -\sigma$. Body forces and external forces act as sources of momentum, represented by $S = \rho g + \vec{f}$. where g is the acceleration of gravity and $\vec{f}$ is external force per unit volume. Substituting these components into the generic transport equation (Eq. (3.1)) results in the momentum conservation equation known as the Navier-Stokes equation:

$$\rho\left(\frac{\partial\vec{v}}{\partial t} + (\vec{v}\cdot\nabla)\vec{v}\right) = \nabla\cdot\sigma + \rho g + \vec{f} \tag{3.5}$$

For viscous fluids, the stress tensor $\nabla\cdot\sigma$ in Eq. (3.5) can be decomposed into pressure and viscous stress components (Zohuri, 2017):

$$\rho\left(\frac{\partial\vec{v}}{\partial t} + (\vec{v}\cdot\nabla)\vec{v}\right) = -\nabla p + \nabla\cdot(\mu\nabla\vec{v}) + \rho g + \vec{f} \tag{3.6}$$

Under steady-state conditions with incompressible flow and no external or gravitational forces acting on the control volume, Eq. (3.6) can be simplified to:

$$\nabla \cdot (\rho \vec{v} \vec{v}) = -\nabla p + \nabla \cdot (\mu \nabla \vec{v}) \tag{3.7}$$

3.1.3 Energy conservation equation

The energy conservation equation is fundamental to understanding and modeling heat transfer within both fluid and solid regions of a system. It accounts for heat conduction in all phases, convection in fluids, and any energy sources or sinks present within the domain. In CFD modeling, this equation is essential for predicting temperature distributions and heat transfer rates. The energy conservation equation can also be derived from the generic transport equation Eq. (3.1). For a single-phase material, heat flux has two principal components: convection (or transport) and conduction. In a static, closed system, the convective transport scalar in the generic equation can be expressed as the internal energy per unit volume, $\phi = \rho c_p T$, where ρ is the density, c_p is the specific heat capacity, and T is the temperature. The conduction component, described by Fourier's law, is $\mathcal{F} = -\lambda \nabla T$, where λ represents thermal conductivity and ∇T denotes the temperature gradient. The negative sign indicates that heat flows from the hot region to the cold region. Radiative heat transfer is often neglected in heat exchanger modeling because the exchanger is enclosed and thermally insulated, minimizing radiative exchange with the surroundings, while conduction and convection remain the dominant heat transfer mechanisms. Additional heat sources or sinks, such as heat sinks, or viscous dissipation, can be incorporated into the source term *S*. By substituting all the above into the generic transport equation Eq. (3.1), the simplest form of the energy conservation equation can be written (Anderson, 2010; Zohuri, 2017; Patankar, 2018):

$$\rho c_p \left(\frac{\partial T}{\partial t} + (\vec{v} \cdot \nabla) T \right) = \nabla \cdot (\lambda \nabla T) + S_h \tag{3.8}$$

The first term on the left-hand side of Eq. (3.8) represents the rate of change of internal energy in the system due to the time-dependent variation of temperature. The second term on the right-hand side is the heat source term, accounting for any internal heat generation or dissipation within the system, such as viscous dissipation (heat produced by friction in the fluid), chemical reactions, or external heat sources or sinks. Under steady-state

conditions (i.e., no time dependence of temperature, $\partial T/\partial t = 0$), and neglecting external heat sources such as viscous dissipation, Eq. (3.8) can be simplified to:

$$\nabla \cdot \left(\rho \vec{v} c_p T\right) = \nabla \cdot \left(\lambda \nabla T\right) \tag{3.9}$$

The term on the left-hand side of Eq. (3.9) is convective heat transport, describing how heat is carried by the flow of the fluid. The term on the right-hand side of Eq. (3.9) represents heat conduction, illustrating how heat diffuses through a material as a result of temperature differences. Heat conduction takes place within a body (solid, liquid, or gas) or between bodies in contact. It is the direct microscopic exchange of the kinetic energy of particles due to a temperature gradient between two systems (Azadeh, 2017).

Eq. (3.9) governs heat transfer within the fluid, accounting for both convective and conductive heat mechanisms. However, in the solid region, where fluid motion is absent and heat transfer occurs only through conduction, Eq. (3.9) reduces to:

$$\nabla \cdot \left(\lambda_w \nabla T\right) = 0 \tag{3.10}$$

Here λ_w is the thermal conductivity of the solid wall.

3.2 Conjugate heat transfer

In the simulations of the ICT heat exchangers, conjugate heat transfer (CHT) formulations were employed to precisely predict temperature distributions and heat transfer phenomena within ICT ducts. This formulation considers heat transfer processes within solid and fluid regions simultaneously, addressing them as a single integrated system. This enables a detailed analysis of the heat flux interaction between the two domains, providing insights into complex thermal behavior. The CHT includes closely coupled heat conduction in a solid region and convective heat transfer in a neighboring fluid region (Chen & Han, 2000). This is achieved by solving the governing equations within both the fluid and solid domains, while ensuring that the interfacial boundary conditions are consistent (Cole, 2023).

In conjugate heat transfer (CHT), interface boundary conditions enforce continuity of temperature and heat flux across the solid-fluid interface. This ensures no energy

accumulation/loss and enables the assumption of local thermal equilibrium at the interface (Luna et al., 2002). Temperature continuity is expressed as:

$$T_w(\mathbf{x}) = T_f(\mathbf{x}) \qquad \text{for all } \mathbf{x} \in \Gamma_{\text{interface}} \tag{3.11}$$

Here, $\Gamma_{\text{interface}}$ denotes the solid–fluid interface, i.e., the boundary at which the solid domain and the fluid domain are in thermal contact. The continuity of heat flux is given by:

$$\lambda_w \nabla T_w \cdot \boldsymbol{n} = \lambda_f \nabla T_f \cdot \boldsymbol{n} \tag{3.12}$$

where λ is the thermal conductivity and $\boldsymbol{n}$ is the unit normal vector on the wall. Subscripts *f* and *w* indicate values corresponding to fluid and solid phases, respectively. In Eq. (3.12), the term on the left-hand side (LHS) represents the heat flux at the solid-side face, while the right-hand side (RHS) pertains to the fluid-side face. This condition applies specifically at the solid–fluid interface, where thermal energy is exchanged between the two domains. To ensure accurate representation of this heat transfer interaction, the governing equations in both domains must be coupled—either through simultaneous (monolithic) solution or through an iterative (partitioned) approach—so that the interfacial boundary conditions are consistently satisfied.

3.3 Turbulence modeling

Turbulence in fluid dynamics is characterized by the chaotic and unpredictable motion of fluid particles. This complex and fundamental phenomenon plays an essential role in both natural systems and human-engineered applications. A key concept in turbulence is the energy cascade, which describes the transfer of kinetic energy from large-scale eddies to smaller-scale structures (Pope, 2000). This process is especially prominent in flows with high Reynolds numbers, where inertial forces significantly outweigh viscous forces.

Turbulence modeling is crucial in various engineering fields. It involves developing and applying mathematical models to predict turbulence effects in fluid flow, typically by solving the Navier-Stokes equations through Computational Fluid Dynamics (CFD). While laminar flows can be solved with relatively straightforward numerical methods because of the smooth and predictable nature of the flow, turbulent flows present

significant challenges due to their chaotic and multi-scale nature (Liu et al., 2023). In turbulent flows, viscous effects primarily occur at smaller scales, which interact in complex ways with larger flow structures. This interaction usually requires advanced computational methods to resolve complex turbulent structures and precisely model the energy transfer across different scales (Davidson, 2004).

Various numerical methods have been developed to compute turbulent flows, which are typically categorized into three main approaches.

1. Direct Numerical Simulations (DNS)
2. Large Eddy Simulations (LES)
3. Reynolds-Averaged Navier-Stokes (RANS) models

Direct Numerical Simulation (DNS) involves solving Navier-Stokes and continuity equations to resolve all fluid scales of motion. DNS requires exceptionally fine grid spacing to account for every scale within the fluid. While this method produces highly detailed flow data, it also demands significant computational resources (Zhou, 2018). Large Eddy Simulation (LES) is an alternative method for simulating turbulent flows. It approximates smaller scales of turbulence while resolving larger ones. The core concept of LES turbulence modeling is to separate large- and small-scale turbulence by applying a filter to the velocity field, effectively splitting it into filtered (resolved) and modeled (sub-grid) components (Zhiyin, 2015). LES has demonstrated accuracy in a wide range of industrial and non-industrial applications while requiring fewer computational resources compared to DNS (Zhou, 2018). However, LES still exceeds the computational cost of RANS simulations. The third method, RANS, is discussed in the following section.

3.3.1 Reynolds-Averaged Navier-Stokes equations (RANS)

Reynolds-Averaged Navier-Stokes (RANS) is a common approach used to compute turbulent flow. It is computationally more efficient than DNS and LES, making it suitable for a wide range of engineering applications where a balance between accuracy and computational cost is required (Dastbelaraki et al., 2018). For these reasons, RANS was found to be more suitable for modeling the flow in ICT heat exchangers.

The RANS equations are obtained by applying an averaging operation to the Navier-Stokes equations. This results in mean equations of fluid flows that are similar to the

original momentum equation (Eq. (3.7)) but contain additional terms called Reynolds stress terms (Davidson, 2004). For steady state and an incompressible turbulent flow, the Eq. (3.7) can be re-written as:

$$\nabla \cdot (\rho \vec{v} \vec{v}) = -\nabla p + \nabla \cdot [(\mu + \mu_t)(\nabla \vec{v} + (\nabla \vec{v})^T)] \tag{3.13}$$

The second term on the right-hand side of Eq. (3.13) represents the sum of the viscous and turbulent (Reynolds) stresses (Pope, 2000; Canli et al., 2021). In turbulent flow, Reynolds stresses are determined by the Boussinesq approximation (Pope, 2000). The eddy (or turbulent) viscosity μ_t is obtained by combining two scalars: the turbulent kinetic energy k and its dissipation rate ϵ:

$$\mu_t = \rho C_\mu \frac{k^2}{\epsilon} \tag{3.14}$$

Here, ρ is the fluid density, and C_μ, based on eddy viscosity models, is either an empirical constant or a function of turbulence fields, mean strain, and rotation rates (cf. Davidson (2004); Wang et al. (2009)).

Turbulence also has a substantial impact on heat transfer, primarily by enhancing thermal mixing. To incorporate this effect into the energy equation Eq. (3.9), an effective thermal conductivity λ_{eff} is introduced, which accounts for both molecular and turbulent contributions to heat transfer (Lienhard, 2020):

$$\lambda_{eff} = \lambda_f + \frac{c_p \mu_t}{Pr_t} \tag{3.15}$$

where Pr_t is the turbulent Prandtl number, assumed 0.85 (Reynolds, 1975), λ_f is the fluid thermal conductivity and μ_t is the eddy viscosity computed via turbulence model described in Eq (3.14).

Thus, the energy equation (Eq. (3.9)) can be written in terms of the effective thermal conductivity to include the effects of turbulence, as follows:

$$\nabla \cdot \left(\rho \vec{v} c_p T\right) = \nabla \cdot \left(\lambda_{eff} \nabla T\right) \tag{3.16}$$

The solution of RANS equations requires closure through determination of the turbulent viscosity μ_t. RANS-based turbulence models are commonly categorized based on the number of additional transport equations that must be solved alongside the RANS equations. Figure 3.1 outlines the most widely employed eddy viscosity models in engineering fields. Each turbulence model has its advantages and limitations, depending on its level of detail, accuracy, and suitability for specific flow cases. For simple flows where high accuracy is not required, a zero- or one-equation model might be sufficient. For more complex flows, two-equation models are generally preferred. Thus, selecting an appropriate turbulence model heavily depends on the nature of the fluid flow under study.

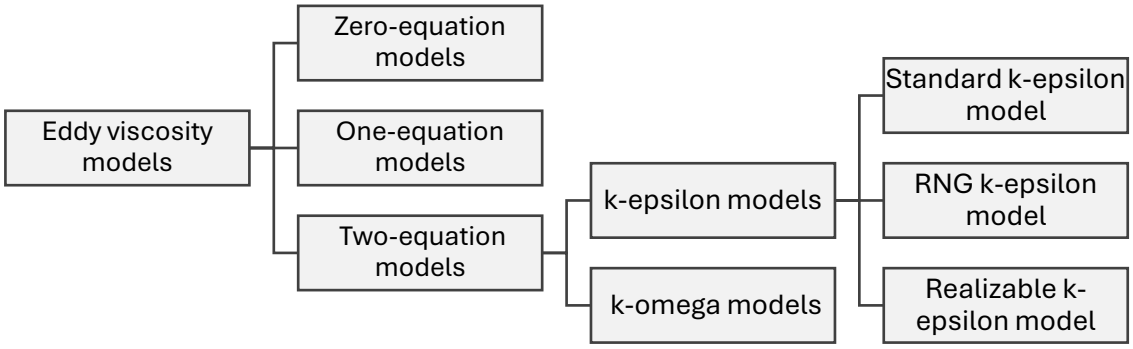

Figure 3.1: Overview of turbulence models (Zhai, 2020).

The $k-\epsilon$ models, which includes two additional equations for turbulent kinetic energy (k) and turbulent dissipation rate (ϵ), is most frequently used (Blazek, 2015). These equations are solved together with the RANS equations, while the eddy viscosity is determined according to Eq. (3.14). The standard $k-\epsilon$ model is frequently used due to its simplicity. However, it has limitations in complex geometries with strong pressure gradients and flow separations, leading to excessive dissipation and high turbulent viscosity that might dampen vortices (Blazek, 2015). The RNG $k-\epsilon$ model is an advanced turbulence model that improves upon the standard $k-\epsilon$ model by including an additional term in the turbulence dissipation equation. This enhancement makes the RNG model more accurate for flows with rapid strain and swirl effects. It also provides better predictions for turbulent viscosity and Prandtl numbers, especially in low-Reynolds-number conditions (Pope, 2000).

The realizable $k-\epsilon$ model is a more recently developed approach that differs in its treatment of turbulent viscosity and dissipation rate equations. It aligns well with the physics of turbulence and generally outperforms the standard and RNG models in complex geometries, especially in flows with strong curvature, vortices, and rotation (Pope, 2000; Blazek, 2015). Based on performance and computational cost considerations, the realizable $k-\epsilon$ model is suggested as the suitable model for simulating turbulent flow in the ducts of the ICT heat exchangers, with a detailed discussion provided in the following section.

3.3.2 Realizable $k-\epsilon$ model

The $k-\epsilon$ model is robust and reasonably accurate for a wide range of applications (Singh et al., 2020). It provides superior performance with enhanced wall treatment implementation for flows involving boundary layers under strong adverse pressure gradients, separation, and recirculation (Aupoix, 2002). Unlike the $k-\omega$ model, which can be overly sensitive to the specification of free-stream values for ω and requires careful attention to inlet boundary conditions, the realizable $k-\epsilon$ model is generally more robust, less sensitive to inlet conditions, and less computationally costly (Zhai, 2020).

A model is considered "realizable" if it satisfies specific mathematical restrictions on the Reynolds stresses that align with the physics of turbulent flows, as described in (Shih et al., 1995). Both the standard and RNG $k-\epsilon$ models are not realizable. Furthermore, C_μ in the realizable $k-\epsilon$ model is no longer constant as in the standard model. Instead, it becomes a function of the turbulence fields, mean strain, and rotation rates (cf. Shih et al. (1995); Wang et al. (2009)).

The full description of the realizable $k-\epsilon$ model equations can be found in (Shih et al., 1995).

3.3.3 Near-wall treatment

In fluid dynamics and heat transfer problems, boundaries are often specified by walls. At high Reynolds numbers, the region adjacent to these walls—referred to as the boundary layer—experiences significant fluctuations in velocity. This is because the velocity starts at zero precisely at the wall (due to the no-slip condition) and rapidly transitions to the bulk velocity over a relatively short distance. This rapid transition creates steep velocity

gradients within the boundary layer. These velocity gradients, along with the associated shear stresses and turbulent fluctuations, significantly influence fluid flow characteristics and heat transfer rates near walls.

The turbulent eddy and swirling motions cease in zones very close to a solid wall, and the fluid velocity at the wall surface is zero. Thus, viscous shear stresses dominate the fluid flow in this region rather than turbulent shear stresses (Pope, 2000). The velocity profile within the near-wall region has a defined shape, which can be accurately characterized by the "law of the wall" (cf. Figure 3.2). The viscous sublayer, the first layer adjacent to the wall, is extremely thin and exists within dimensionless wall distance $y^+ < 5$. The velocity and distance to the wall in this region are commonly expressed using the following dimensionless parameters (Davidson, 2004):

$$u^+ = u/u_\tau \tag{3.17}$$

$$y^+ = u_\tau \tilde{y}/\nu \tag{3.18}$$

where $\tilde{y}$ is normal distance to the wall and u is the fluid velocity . Both parameters u^+ and y^+ are based on the friction velocity u_τ, which is directly associated with the wall shear stress defined by:

$$u_\tau = \sqrt{\tau_w/\rho} \tag{3.19}$$

In the viscous sublayer, the velocity profile exhibits almost linear behavior (Davidson, 2004) and can be expressed as follows:

$$u^+ = y^+ \tag{3.20}$$

In the log-law layer or region ($y^+ > 30$), the turbulent viscosity is much greater than the molecular viscosity. The velocity profile can be described by a logarithmic function:

$$u^+ = \frac{1}{k} ln(y^+) + 5.5 \tag{3.21}$$

Here, k is Karman constant, and typically 0.41 (Pope, 2000). The third layer is called "buffer layer" which is the region between the viscus sublayer and the log-law layer ($5 < y^+ < 30$) (cf. Figure 3.2). In this layer, viscous and turbulent stresses have approximately similar magnitude ($\mu \approx \mu_t$). Thus, the velocity profile is not clearly described, and the original wall functions avoid the first cell center located in this region (Zhang et al., 2022).

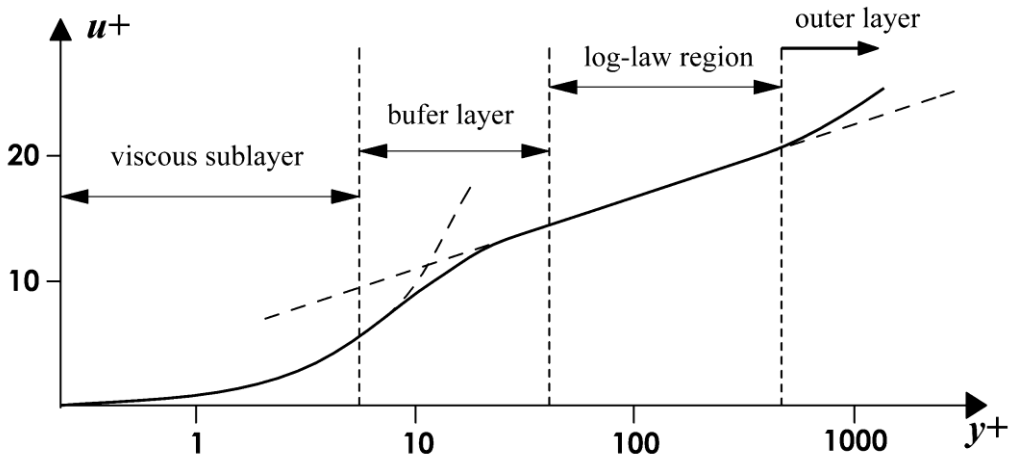

Figure 3.2: Boundary layer profile (Christopher & Weller, 2022).

Accurately modeling fluid behavior near walls in complex geometries presents significant challenges in computational fluid dynamics (CFD). Identifying the first cell within the viscous sublayer or log-law region is difficult due to varying distances of cell centers from the wall. Steep velocity gradients near walls necessitate finely discretized grids to capture boundary layer characteristics accurately. Additionally, turbulence models such as the $k - \epsilon$ models exhibit higher accuracy in fully developed turbulent regions and demonstrate insufficient performance in the vicinity of the wall. These challenges make near-wall modeling critical in CFD simulations of complex geometries. To address these issues, near-wall treatments or wall functions are employed alongside the $k - \epsilon$ turbulence model to effectively capture flow dynamics in these regions. This approach improves predictions of wall-bounded flows, especially at high Reynolds numbers, by bridging the gap between turbulence models and wall effects (Nazif & Tabrizi, 2014). Wall functions

reduce the need for highly refined grids while ensuring a smooth transition between the viscous sublayer and turbulent layers, significantly decreasing computational costs by reducing the number of required cells (Canli et al., 2021).

Among available wall functions, enhanced wall function or enhanced wall treatment was used in this study and adopted with the realizable $k-\epsilon$ model. Enhanced wall function is a two-layer model which resolves the entire boundary layer until the viscous sub-layer (Wolfshtein, 1969; Kader, 1981). This technique partitions the domain into two different regions: one affected by viscosity and the other characterized by full turbulent flow. This function also enables a smoother transition between these regions by using a blending function. A full description of enhanced wall function approach can be found in Refs. (Wolfshtein, 1969; Davidson, 2004).

3.4 Computational fluid dynamics (CFD)

The differential equations presented by Eq. (3.3), (3.7), and (3.9), together with the turbulence model equations and the corresponding boundary conditions, constitute a complete set of thermal and fluid dynamic equations governing the system. Due to their non-linear partial differential nature, these equations could not be solved analytically, making numerical methods essential for obtaining solutions. These methods involve discretizing the differential transport equations into algebraic equations. The set of algebraic equations is then solved using standard matrix approaches, which are executed numerically on a computer.

The three methods—the finite difference method (FDM), the finite element method (FEM), and the finite volume method (FVM)—are the most commonly employed discretization approaches in computational fluid dynamics (CFD).

The Finite Difference Method (FDM) is a numerical technique for solving differential equations by approximating derivatives—quantifying the rates of change of a dependent variable with respect to its independent variables—using finite difference formulas. These approximations are systematically derived from truncated Taylor series expansions and are applied following the discretization of the computational domain into a structured grid. This allows the derivative at a given point to be estimated based on functional values at adjacent grid nodes (Roache, 1976). Due to its conceptual simplicity and straightforward

implementation, FDM is especially efficient and appropriate for problems defined over regular domains with structured grids. However, its applicability becomes constrained when dealing with complex or irregular geometries, particularly near curved boundaries or when higher-order accuracy is required (Baker, 1983). In contrast, the finite element method (FEM) is well-suited for handling complex geometries and is widely used in solid mechanics analysis. However, its application in CFD poses challenges due to its mathematical complexity and generally lower accuracy compared to FDM (Baker, 1983). Alternatively, the finite volume method (FVM) is often preferred for its ability to retain most physical data, achieving an optimal balance between flexibility and reliability. In addition to its simplicity and robustness, FVM can be effectively adapted to complex geometries, making it a versatile choice in CFD (Patankar, 2018).

The FVM is based on a division of a computational domain into a finite number of sub-volumes or control volumes (CVs), within which differential conservation equations are integrated (Patankar, 2018). Each sub-volume corresponds to a computational node, enabling the calculation of independent variables (e.g. velocity, pressure, temperature, etc.). This approach simplifies the solution of complex equations by breaking them down into more manageable problems. The size and shape of the sub-volumes can be adjusted to improve the accuracy and efficiency of the solution (Roache, 1976; Patankar, 2018).

Various grid types, including structured grids, unstructured grids, and adaptive grids, are employed to discretize computational domains and create sub-volume grids. Structured grids, also referred to as structured meshes, feature a regular and predefined arrangement of grid points. This uniformity makes them highly efficient and easy to implement, particularly for simple geometries such as rectangles or cylinders. Structured grids typically use hexahedron elements for modeling 3D flows and require significantly less memory compared to unstructured grids with an equivalent number of grid points (Bern & Plassmann, 2000). However, the rigid structure limits their adaptability to complex geometries.

In contrast, unstructured grids are indeed well-suited for complex geometries due to their irregular and flexible arrangement of grid points and elements. Nodes in unstructured grids are placed at arbitrary locations in the computational domain, and elements (e.g., triangles, tetrahedra, cf. Figure 3.3) can vary in shape and size. This flexibility allows

unstructured grids to accurately represent intricate geometries, but the connectivity between nodes must be explicitly defined and stored (Patankar, 2018).

Adaptive grids are particularly useful in regions where the solution exhibits rapid variations or where high precision is required. These grids adaptively refine or coarsen the mesh to capture critical features of the solution more effectively (Roache, 1976).

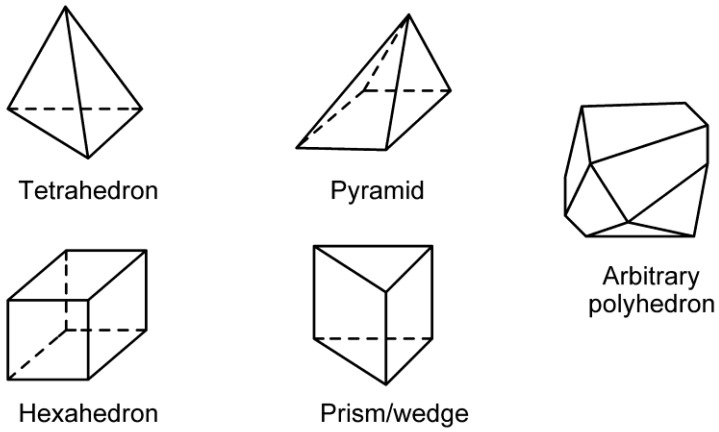

Figure 3.3: Different types of grid elements (SimuTech Group, accessed 22.09.2023).

Structured grids can be used effectively for complex geometries when employing a multi-block topology (Ali et al., 2016). In this method, the CFD domain is partitioned into multiple regions or subdomains, which enhances grid management efficiency and flexibility (see Figure 3.4a). This partitioning facilitates the generation of structured grids within each subdomain. Additionally, the structured grids can be aligned in such a way that the cell faces of adjacent fluid-phase domains (e.g., fluid_1 and fluid_2, as shown in Figure 3.4c) coincide with the corresponding faces of the solid domain cells near the wall surface. This alignment is particularly beneficial for minimizing interpolation errors, especially in simulations involving heat transfer between solid and fluid domains (Zibart & Kenig, 2021).

The stability and accuracy of the Finite Volume Method (FVM) solution are significantly influenced by the quality of the grid cells. This crucial aspect of grid generation extends beyond the choice of grid type. Grid quality involves several key factors, among others, cell skewness, aspect ratio, and orthogonality, all of which play a vital role in determining the reliability and precision of the FVM solution.

- **Aspect Ratio**: This parameter is defined as the ratio of the longest to the shortest lengths of grid elements in different directions. High-quality grids should maintain balanced aspect ratios to avoid elongated or compressed elements, which can lead to numerical inaccuracies (Christopher & Weller, 2022).
- **Grid Skewness**: This factor measures the deviation of grid elements from their ideal shapes. Lower skewness values indicate cells that are closer to regular shapes, which enhances simulation accuracy (Katz & Sankaran, 2011).
- **Grid Orthogonality**: This quantity refers to the angles between grid lines or faces. In well-structured grids, these angles are close to 90 degrees, which promotes superior numerical convergence and minimizes interpolation errors (Christopher & Weller, 2022).

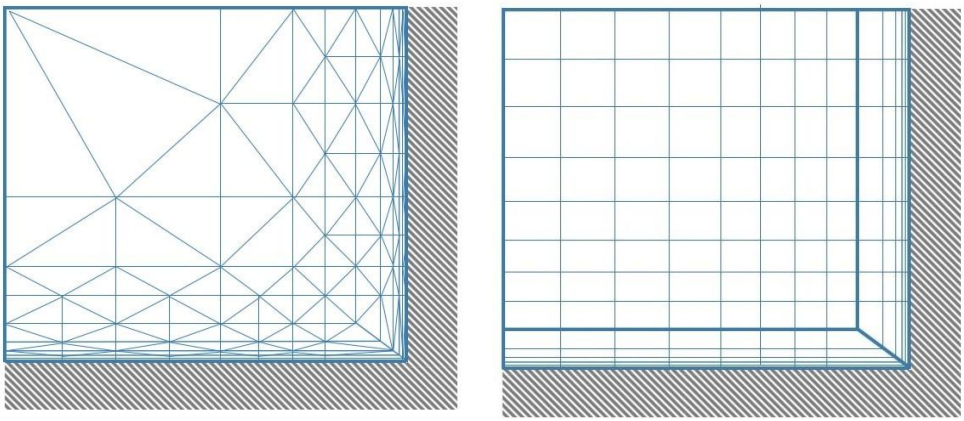

(a) (b)

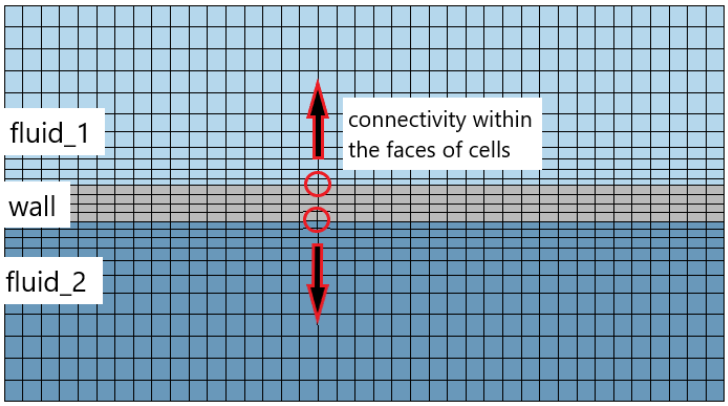

(c)

Figure 3.4: Mesh topology (SSG AERO - Agile Aerodynamic Design, accessed 01.04.2024): Unstructured mesh (a); multi-block-structured mesh (b), structured mesh, showing faces fluid domains coinciding with corresponding cell faces of solid domain [c].

3.5 Conclusions

This chapter presents the theoretical and methodological framework necessary for conducting CFD analyses of ICT heat exchangers. In Computational Fluid Dynamics, the simulation of fluid flow and heat transfer is based on the conservation equations of mass, momentum, and energy. These equations, derived from a generalized transport formulation, are adapted to reflect specific conditions such as steady-state and incompressible flows. Conjugate Heat Transfer modeling is essential for accurately simulating the interaction between solid and fluid domains. This is achieved by ensuring the continuity of temperature and heat flux at interfaces through a combined treatment of conduction and convection.

Turbulence is commonly modeled using Reynolds-Averaged Navier-Stokes (RANS) approaches, which represent a broad class of turbulence models balancing accuracy and computational cost. Within this framework, the realizable $k - \epsilon$ model is one widely used variant, valued for its robustness. Furthermore, the Finite Volume Method is often used for discretization because of its robustness, ability to conserve physical quantities, and flexibility in handling complex geometries and high-quality grids.

4 The geometry of ICT heat exchangers

The fundamental design principles of ICT heat exchangers aim to achieve higher thermal performance and a compact size. The method for improving thermal efficiency in the ICT involves extending the heat transfer surface area between hot and cold fluids without increasing the unit size. This is accomplished by incorporating multiple curved-shaped channels within a circular tube that has an insulated exterior surface. The use of curved channels can improve heat transfer capabilities compared to flat-surfaced channels (e.g., square or triangle shapes) (Brodnianská & Kotšmíd, 2023; Guo et al., 2023), contributing to an overall optimized performance.

The structure of the ICT exchangers was established based on preliminary CFD simulations, using a variety of curved channel shapes, from which the most effective design was ultimately selected. The configurations of the channels are determined by curve functions, leading to the exploration of two different ICT designs in this study. ICT1 features a parabolic channel shape, while a channel ICT2 resembles a Gaussian function (bell-shaped function). This generative method, leveraging curve functions, provides practical flexibility for future optimization possibilities, allowing for the customization of channel shapes, scaling options, or the addition of more channels.

Determining geometrical parameters for heat exchangers is a crucial step in their design process. For simple designs, calculating parameters such as the heat transfer area, mean cross-sectional area, and hydraulic diameters are typically straightforward. However, this becomes challenging for ICT heat exchangers due to the complex shapes of ICT ducts. This challenge was addressed by adopting a mathematical representation of the curve functions, which enables accurate determination of such parameters.

4.1 The concept of ICT structures

The internally channeled tube (ICT) heat exchanger comprises two different flow regions: the core region and the curved channels. The channels are fitted in a tube geometry, insulated from the outer surface (cf. Figure 4.1). The hot fluid flows within the core region, while the cold fluid moves countercurrently through the channels. In Figure 4.1, the shaded areas with blue color represent a cold fluid, while the red color area indicates a hot fluid. This flow arrangement efficiently minimizes heat dissipation into the surrounding environment, thereby reducing the need for insulation material. This is because the insulated surface area on the core region side is smaller than that on the channel side. In this study, two different ICT configurations are explored, comprising six channels: so-called ICT1 and ICT2, shown in Figure 4.1.

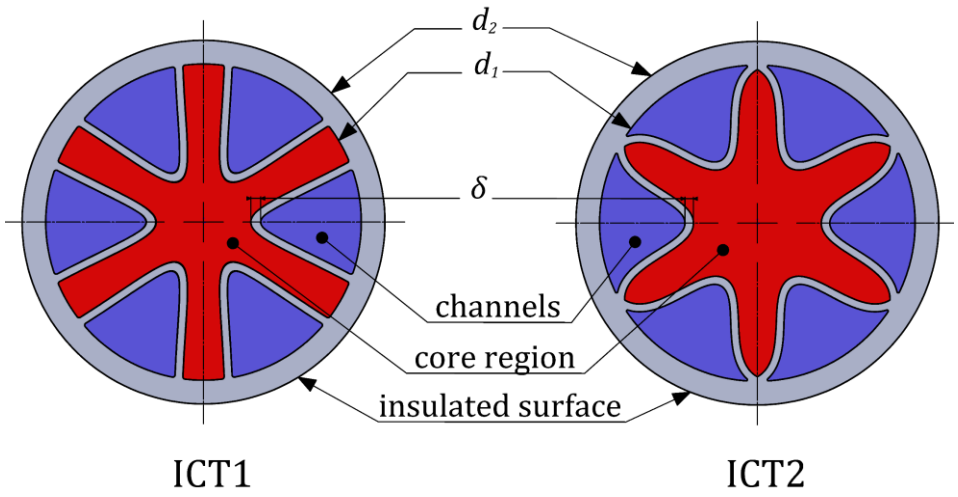

Figure 4.1: Cross-sectional view of the considered ICTs.

The geometries of ICTs, depicted in Figure 4.1, were determined based on the inner and outer curves. Computer-Aided Design (CAD) software was used to form the ICT geometry. The curves for ICT1, shown in Figure 4.2a, are described by Eq. (4.1), while the curves for ICT2, illustrated in Figure 4.2b, correspond to an adjusted Gaussian function given by Eq. (4.2):

$$x = f(y)_i = f(y)_o = c + 81 \cdot \alpha \cdot \left(\frac{y}{\alpha}\right)^{\Pi_1} - 32 \cdot \Gamma \cdot \left(\frac{y}{\Gamma}\right)^{\Pi_2} \tag{4.1}$$

$$x = f(y)_i = f(y)_o = \zeta - \frac{\sigma^2}{\Omega \cdot \sqrt{\pi}} e^{-1.2 \cdot \left(\frac{y}{\Omega}\right)^{\Pi_3}} \quad (4.2)$$

The indices i and o in Eq. (4.1) and (4.2) indicate that the equation is applied to the inner and outer curves, respectively. The configurations of the ICTs are fixed by the values of the corresponding parameters (c, α, Γ, ζ, Ω, and σ) along with exponents $\Pi_1 to\ \Pi_3$, as outlined in Eq. (4.1)-(4.2) and given in Table 4.1. In both ICT designs, the inner (d_1) and outer (d_2) diameters of the tubes (shown in Figure 4.1) are 40mm and 46mm, respectively. The selected total cross-sectional area of channels is slightly larger than that of the core region with the ratio (A_{ch}/A_{cr}) equal to 1.16. The internal wall thickness (δ) of the channels is 1mm (cf. Figure 4.1) and the total length of each exchanger is 1m.

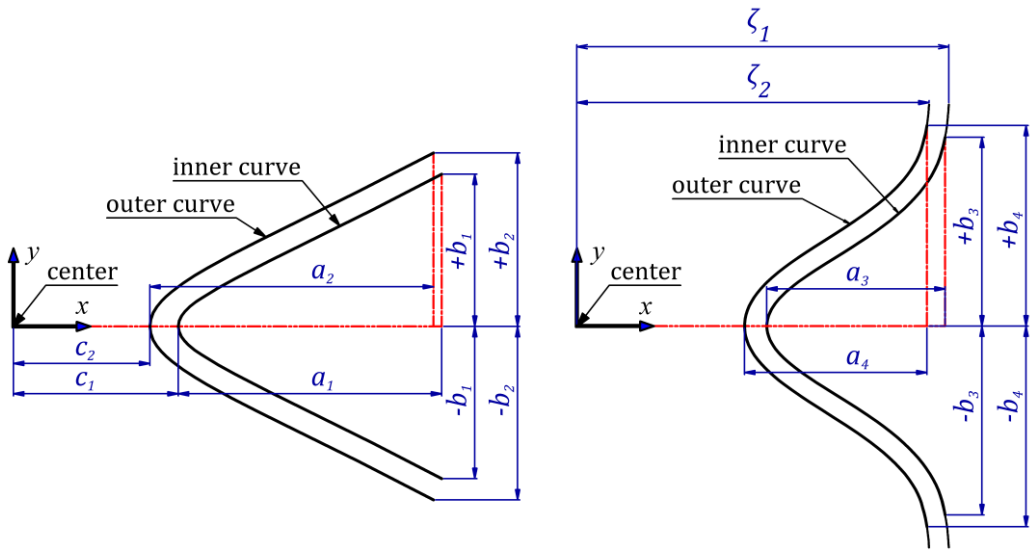

(a) (b)

Figure 4.2: ICT inner and outer curves: ICT1(a), ICT2 (b). c_i and ζ_i are parameters in Eq. (4.1)-(4.2), (i: 1, 2); a_m and b_m are dimensions given in Table 4.2 (m:1,2-4).

Table 4.1: Parameters of Eq. (4.1)-(4.2)

Curve	c [mm]	α [mm]	Γ [mm]	ζ [mm]	σ [mm]	Ω [mm]	Π_1 [-]	Π_2 [-]	Π_3 [-]
inner	7.252	37.983	14.41	18.03	9.111	5.280	1.927	2.035	2.00
outer	6.000	21.515	9.782	17.00	9.469	5.724	2.116	2.186	2.34

Table 4.2: Parameters of inner and outer curves

m	a_m [mm]	b_m [mm]
1	11.594	6.699
2	12.484	7.639
3	8.608	9.142
4	8.718	9.714

4.2 Determination of geometrical parameters

The determination of the geometrical parameters of ICTs ducts, including cross-sectional areas, hydraulic diameters, and heat transfer areas, is not straightforward. As mentioned earlier, this is primarily due to the complex structure of ICT geometry. Insufficient calculations of such parameters can lead to significant discrepancies in computed values such as the friction factor and Nusselt number. For accurate evaluation of geometrical parameters, a numerical integration technique based on the inner and outer curve functions, Eqs. (4.1)-(4.2), is employed. The channel cross-sectional area (A_{ch}) of ICTs is determined by integrating the area under the inner curves according to Eq. (4.3). This is realized using Eqs. (4.1)-(4.2), along with the equation of a circle ($x^2 + y^2 = (d_1/2)^2$). The integration is performed over the corresponding domain ($-b_m \leq y \leq +b_m$), as given in Table 4.2.

$$A_{ch} = \int_{-b_m}^{+b_m} \left[\left(\sqrt{\left(d_1/2\right)^2 - y^2} \right) - f(y)_i \right] dy \tag{4.3}$$

The cross-sectional area of the core region (A_{cr}) is determined by subtracting the total area enclosed by the outer curves from the area of the inner pipe, as expressed by the following equation:

$$A_{cr} = \left(\pi {d_1}^2/4\right) - 6 \cdot Area_{under\ outer\ curve} \tag{4.4}$$

The area under the outer curve is determined using the same method as for the inner curve, with the key difference being the use of the parameters defined in Eqs. (4.1)-(4.2) for the outer curves, along with the respective domains given in Table 4.2.

The area under the outer curve is determined by:

$$A_{under\ outer\ curve} = \int_{-b_m}^{+b_m} \left[\left(\sqrt{\left({}^{d_1}/_{2} \right)^2 - y^2} \right) - f(y)_o \right] dy \tag{4.5}$$

The core region and channels of ICTs are both characterized by ducts that are non-circular in shape. Therefore, the hydraulic diameter of the duct must be used when calculating dimensionless numbers such as the Nusselt number, friction factor, and Reynolds number. However, the existence of the insulated outer surface of ICTs gives rise to two different definitions of diameter. The equivalent diameter (D_e) is based on the perimeter (P_e) across which heat transfer occurs, whereas the hydraulic diameter (D_h) relies on the wetted perimeter (P_h):

$$D_e = \frac{4A_{cs}}{P_e} \tag{4.6}$$

$$D_h = \frac{4A_{cs}}{P_h} \tag{4.7}$$

Figure 4.3 illustrates the equivalent (P_e) and hydraulic (P_h) perimeters in the cross-sections of the core regions and channels. The red and light blue curves represent the equivalent perimeters on the hot and cold sides, respectively. They are determined using Eq. (4.8). In contrast, the length of the insulated perimeters is represented by the black and green curves, calculated by Eqs. (4.9)-to-(4.11). Detailed explanations of the hydraulic and equivalent perimeters can be found in the table presented in Figure 4.3.

In the core region of ICT2, shown in Figure 4.3, the equivalent and hydraulic diameter have identical values. This is due to the absence of insulated perimeters between the channels.

$$Arc\ length(perimeter) = \int_{-b_m}^{+b_m} \sqrt{1 + \left(f'(y)_{i,o} \right)^2}\, dy \tag{4.8}$$

$$Arc\ length_{\ D} = (d_1/2) \cdot \Phi_1 \cdot (\pi/180) \tag{4.9}$$

$$Arc\ length_{\ G} = (d_1/2) \cdot \Phi_3 \cdot (\pi/180) \tag{4.10}$$

$$Arc\ length_{\ C} = (\pi d_1/6) - [(d_1/2) \cdot \Phi_2 \cdot (\pi/180)] \tag{4.11}$$

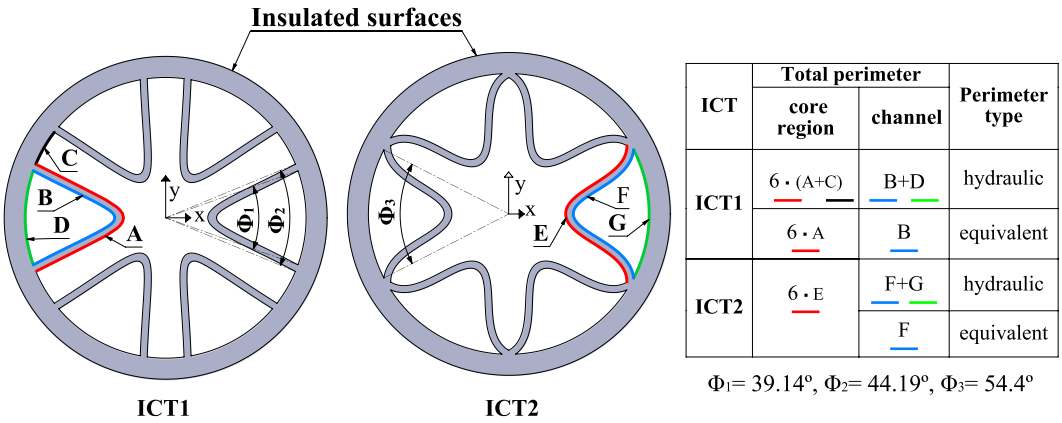

ICT	Total perimeter		Perimeter type
	core region	channel	
ICT1	6 · (A+C)	B+D	hydraulic
	6 · A	B	equivalent
ICT2	6 · E	F+G	hydraulic
		F	equivalent

Φ_1= 39.14°, Φ_2= 44.19°, Φ_3= 54.4°

Figure 4.3: Descriptions of equivalent and hydraulic perimeters of ICTs for both the core region and channels. The table classifies the curves and shows the total equivalent and hydraulic perimeters.

Since the outer surface of ICTs is insulated, no heat is transferred through this surface; instead, heat is transferred only through the interior walls, which is represented by the equivalent perimeter. Furthermore, it is expected that thermal boundary layers do not form on the insulated walls. However, hydrodynamic boundary layers are developed everywhere near the duct walls. This behavior will be explored in more detail in Section 5.3.3. Therefore, the determination of the equivalent diameter is based only on the perimeter of the fluid surface participating in heat transfer. This allows for reasonable evaluation of heat transfer when the Nusselt number is computed using equivalent diameters.

4.3 Conclusions

The ICT concept is based on extending the heat transfer surface area between two fluids in contact by using several curved channels within a circular tube. These curved channels are defined using two different curve functions — parabolic and Gaussian — resulting in two design variants, ICT1 and ICT2. These curve functions help to provide a mathematical method for accurately determining essential geometrical parameters despite the complexity of the channel shapes.

The presence of an insulated surface in the ICTs gives a rise to two different length scales: equivalent diameter and hydraulic diameter—for calculating the Nusselt number and friction factor, respectively. Recognizing these differences is essential for achieving accurate evaluation of critical performance metrics.

5 Fluid dynamics and heat transfer in ICTs

This chapter presents a combined numerical and experimental study to evaluate the fluid dynamics and heat transfer characteristics in ICT heat exchangers. The numerical study employed computational fluid dynamics (CFD) to solve the fundamental equations governing fluid flow and heat transfer within the ducts of ICTs. In turn, experimental investigations provided empirical validation data through precise measurements of pressure drop and temperature distribution under varying flow and thermal conditions.

The experimental setup and measurement procedures are described in detail, with particular attention given to addressing maldistribution issues and characterizing flow types within the ICT ducts.

5.1 Numerical study

The thermal-hydraulic simulations of ICT heat exchangers were preformed on a cluster at the Paderborn Center for Parallel Computing (PC^2), using the ANSYS Fluent software. As discussed in Chapter 3, the numerical determination of velocity, pressure, and temperature fields in the ducts of ICTs was achieved by solving the three-dimensional continuity, momentum, and energy equations using the finite volume method (FVM). Heat conduction in solid walls was coupled with convective heat transfer in adjacent fluid regions. This was considered (CHT) formulation (cf. Section 3.2).

This study includes both turbulent and laminar flow conditions. In turbulent flow conditions, the flow was described using the Reynolds-Averaged Navier-Stokes (RANS) equations. The realizable $k-\epsilon$ model was used to compute the Reynolds stresses as discussed in Section 3.3.

5.1.1 Computational domain

The computational fluid domain is the spatial region where CFD simulations are performed to solve thermal and fluid dynamic equations. As outlined in Chapter 3, this domain must be discretized with a computational grid to enable the solution of the governing equations. Accurate simulations over large domains often require a high number of grid points, which can lead to significant computational time and memory demands. This challenge can be addressed by leveraging symmetries in the geometry and modeling assumptions, enabling the simplification and reduction of the domain size without compromising accuracy.

For the ICT heat exchangers, the domain was reduced by using two symmetry planes oriented at a 60° angle, as illustrated in Figure 5.1. This figure depicts a schematic of the computational domain for conjugate heat transfer (CHT) analysis. The domain is enclosed and includes only one of the six available channels. It consists of two fluid regions—the core region and the channel—separated by a solid wall. The core region is bounded by two symmetry planes. The schematic on the right side of Figure 5.1, labeled section A-A, illustrates the computational domain, including heat conduction through the wall and the associated boundary conditions. The size of the computational domain for the ICTs is defined by the cross-sections of the duct geometry, as illustrated in Figure 4.1 to Figure 4.3, (Chapter 4). The total length of the domain is 1 meter for both the core region and the channel.

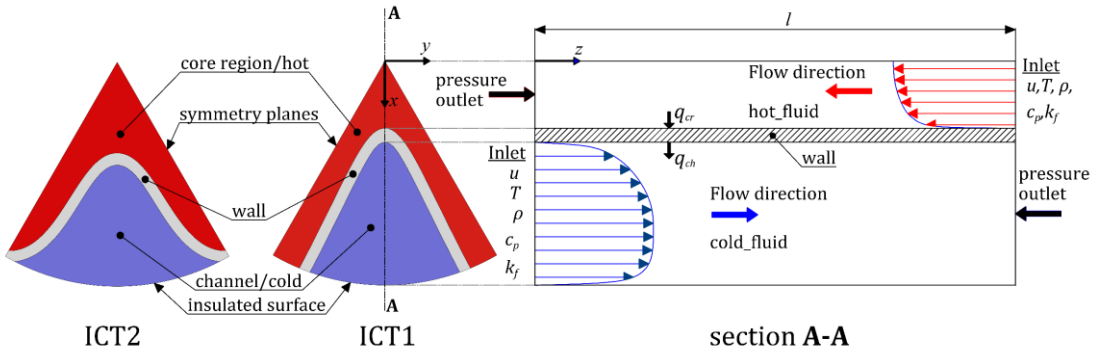

Figure 5.1: Schematic of the computational domain of conjugate heat transfer (CHT) for each element.

A further reduction in the computational domain was achieved by sub-dividing the total length of the ICTs into three elements, namely "middle" element (ME) of 0.5m, and two "entrance" elements of 0.25m. The latter can also be viewed as a right element (RE) and a left element (LE), as shown in Figure 5.2. This domain-splitting approach allows for a reduction in the number of processors required per simulation when using a cluster or local computer, enabling more manageable and scalable simulations. However, it may increase the total computational time due to sequential or partitioned execution.

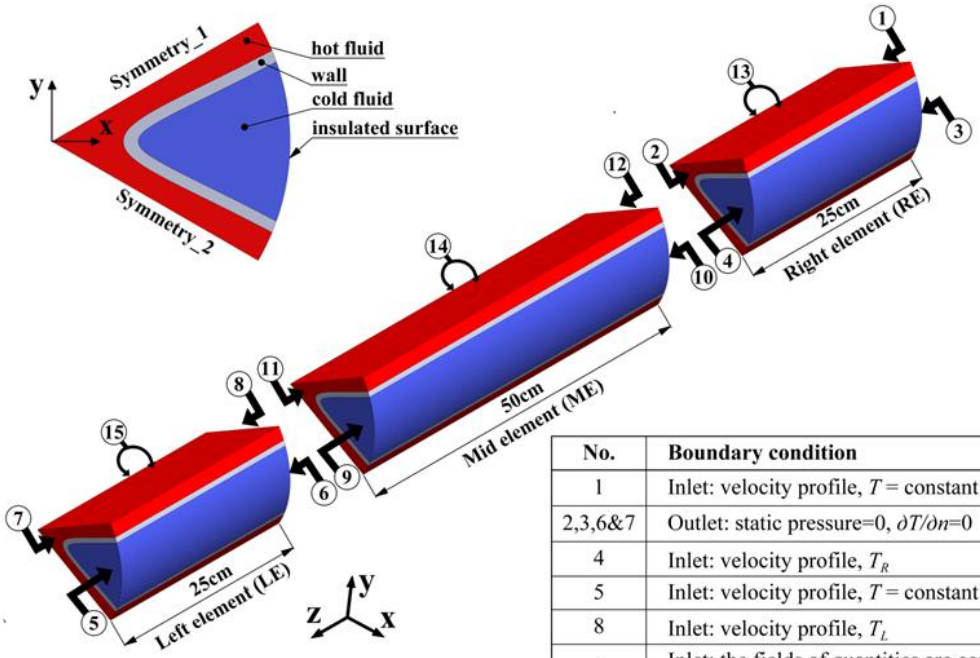

No.	Boundary condition
1	Inlet: velocity profile, T = constant value
2,3,6&7	Outlet: static pressure=0, $\partial T/\partial n$=0
4	Inlet: velocity profile, T_R
5	Inlet: velocity profile, T = constant value
8	Inlet: velocity profile, T_L
9	Inlet: the fields of quantities are copied from (6)
10&11	Outlet: static pressure=0, $\partial T/\partial n$=0
12	Inlet: the fields of quantities are copied from (2)
13,14&15	Symmetry
Heat flux = 0, applied to insulated surfaces.	
Solid and fluid regions are connected by contact interfaces.	

Figure 5.2: ICT1 domain comprising three elements, with applied boundary conditions (the same method is utilized for ICT2).

5.1.2 Boundary conditions

The boundary conditions for the ICT computational domain were defined by applying a conjugate boundary condition at the fluid-wall interfaces to ensure continuous heat flow

across the inner wall (see Section 3.2). The model assumed a hot fluid flowing through the core region, while a cold fluid flows countercurrently through the channel.

Zero-gradient boundary conditions were implemented for velocity components and temperature at the symmetry planes. The walls were described by a zero-value (Dirichlet) boundary condition for all velocity components, in accordance with no-slip condition. Additionally, the adiabatic boundary condition was applied on the outer-tube wall surface since the ICT is insulated from the outer surface, as illustrated in Figure 5.2.

To determine inlet velocities for the elements RE and LE (cf. Figure 5.2), uncoupled simulations were conducted for the core region and channel flow. These simulations provided fully developed velocity and turbulence fields, including turbulent kinetic energy and dissipation rate (under turbulent flow conditions). The fully developed velocity profiles were then used as inlet boundary conditions in the coupled simulations in the core region and channel flow. Given the assumption of a short thermal entrance length in a hydrodynamically fully developed flow, thermal stabilization can be achieved within the middle element (ME). Consequently, pressure drop and heat transfer characteristics were evaluated exclusively within the ME, while the LE and RE served as inlet sections where the flow developed thermally. At the outlet boundaries of the core region and channel, zero static pressure was specified.

Figure 5.3 illustrates the boundary conditions applied to the sub-divided computational domain in the thermal simulations of the ICTs. The inlet temperatures in the core region (for the hot fluid in RE) and in the channel (for the cold fluid in LE) were set to constant values at positions 1 and 5, respectively, as shown in Figure 5.2. The thermal boundary conditions at positions 4 and 8 in RE and LE were obtained through a preliminary simulation of the full-length ICT domain using a very coarse mesh. These temperatures, denoted as T_R and T_L, serve as bridging values between the individual elements RE, LE, and ME and were used only for the initial iteration (see Figure 5.2).

For the middle element (ME), the inlet boundary values were copied from the downstream outlet boundaries of RE and LE elements for most field variables, including velocity, temperature, and turbulence quantities, as depicted in Figure 5.2. Three to five iterations were required to achieve convergent temperature and total pressure values at the outlet of ME, with the percentage difference between the previous and final values being

less than 0.01%. The thermal boundary conditions applied to ME are illustrated in Figure 5.3. For the thermal boundary conditions at the outlets, a zero-gradient condition ($\boldsymbol{n}\cdot\nabla T = 0$) is adopted, where T is temperature and $\boldsymbol{n}$ is the normal vector at the outlet section.

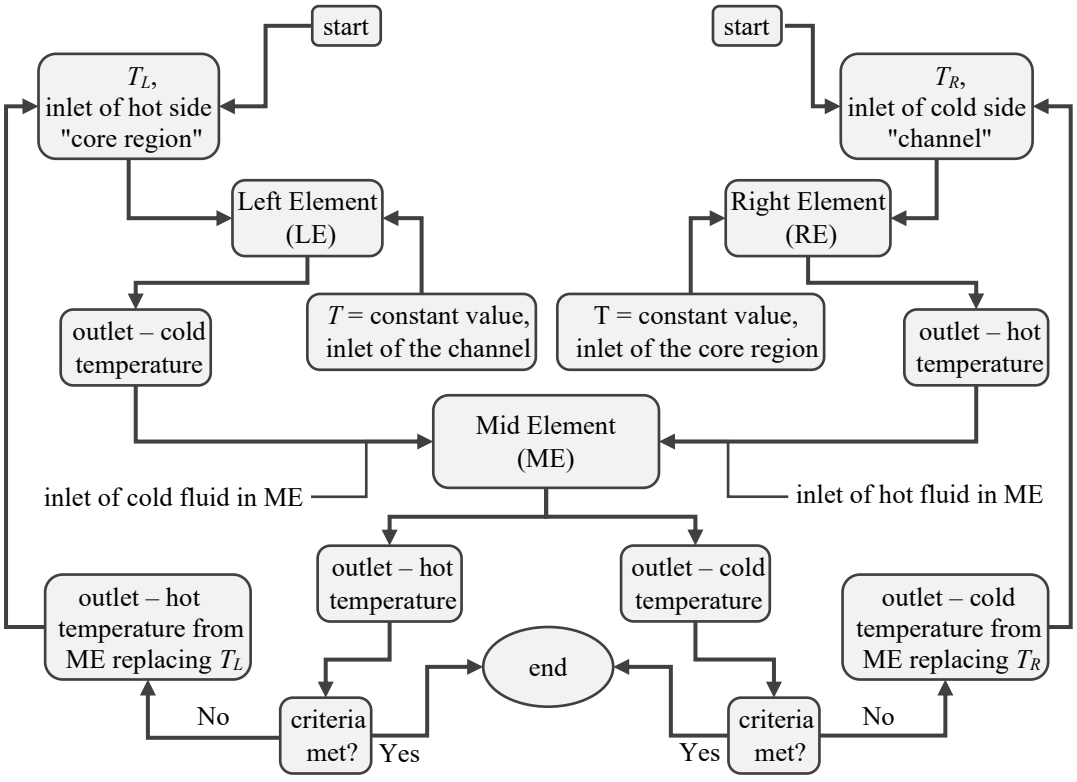

Figure 5.3: Flowchart of thermal boundary conditions applied to LE, RE, and ME.

5.1.3 Grid generation

A structured hexahedral mesh was employed in the simulations of the fluid flow and heat transfer in the ducts of ICTs. The hexahedral meshes were generated using the ICEM software tool, utilizing a multi-block topology (see Figure 5.4a). The method of creating structured blocks involves partitioning the domain into multiple regions, offering a simple and effective technique to create a structured mesh, even within complex geometries, as outlined in Section 3.4. The structured blocks are attached to each other in such a way that the faces of cells of both fluid-phase domains, namely the core region and the channel, which are adjacent to the wall surface, align with the corresponding faces of cells in the solid domain , as shown in Figure 5.4b. This alignment is particularly advantageous in

reducing interpolation errors when simulating phenomena such as heat transfer between solid and fluid domains.

The generated hexahedral meshes for both ICTs are shown in Figure 5.5. The ICT1 (ME) domain, with a length of 0.5m, was composed of a maximum of 12 million cells, while the total number of computational cells for the CHT simulations including both entrance elements (RE & LE) was around 24 million. From these cells, about 12.3 million cells were allocated to the channel, 8.5 million to the core region, and 3.2 million to the solid wall. A similar approach was used to generate the ICT2 mesh, resulting in 14 million cells for the middle element and 28 million cells for the entire domain, including both entrance elements. Approximately 14.2 million cells were assigned to the channel, 9.3 million to the core region, and the remaining 4.5 million cells to the solid wall.

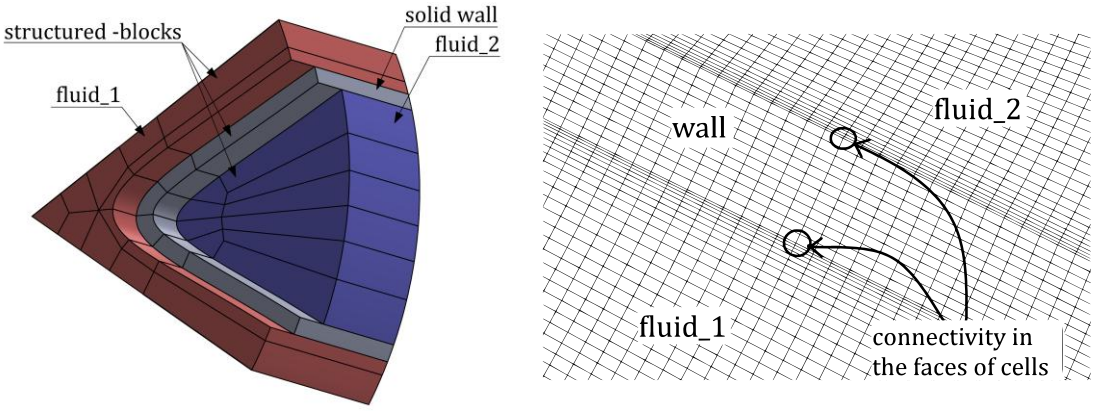

(a) (b)

Figure 5.4: Mesh topology in ICTs: illustration of decomposition of ICT1 domain into structured blocks (a); multi-block-structured mesh in the ICTs, showing faces of fluid domains coinciding with corresponding cell faces of solid domain (b).

During mesh generation, at least 3-5 cells were allocated to the viscous sub-layer to resolve the boundary layers near the wall properly. Due to the complex geometric configuration under consideration, the distances of cell centers from the wall vary. The first cell node adjacent to the wall was selected based on the maximum value of the dimensionless wall distance y^+ defined by Eq. (3.18). The value for the dimensionless parameters y^+ was approximately equal to 2.6. The presence of the walls has a significant effect on turbulent flows, as the viscosity-dominated regions are marked by large gradients of the main quantities. To ensure a smooth transition between viscous sublayers and

turbulent layers, an enhanced wall function was adopted in this work. The enhanced wall function combines two different models (laminar near the wall and turbulent in the outer layers) in the two-layer approach by using a damping function, which makes the transition between the two regions smoother (Davidson, 2004). Furthermore, the wall function approach can lead to a significant reduction in total cell number and helps to avoid high cell aspect ratios, as there is no need in extremely small y^+ values (Kader, 1981; Canli et al., 2021), as discussed in Section 3.3.3.

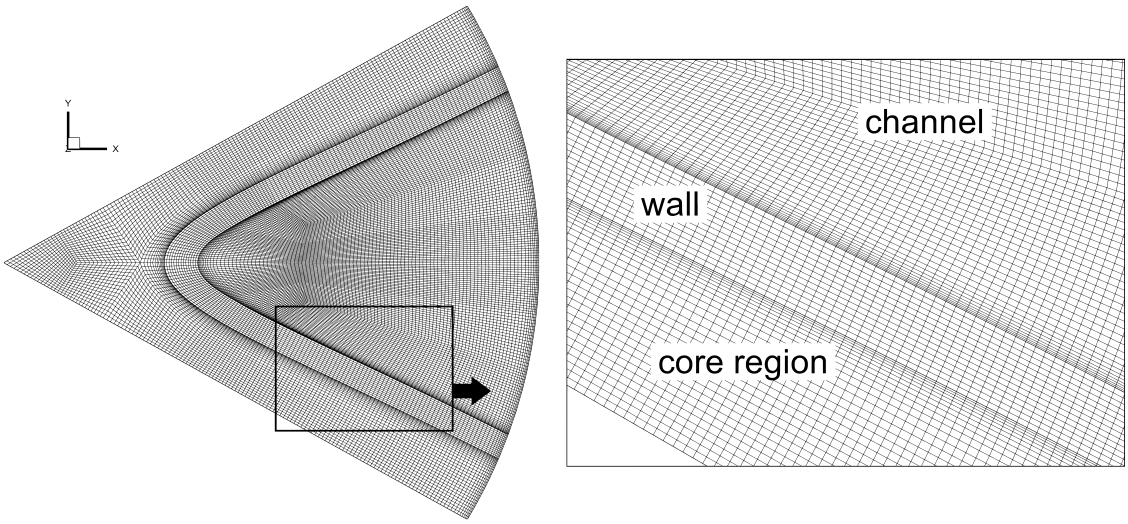

(a)

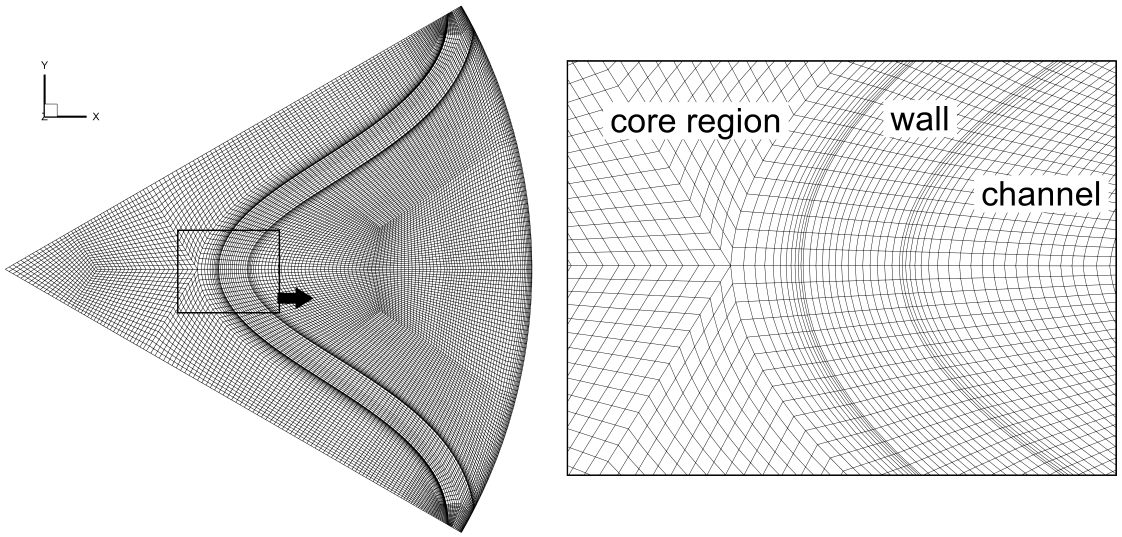

(b)

Figure 5.5: Illustration of the computational grids for the domain; ICT1 (a) and ICT2 (b).

5.1.4 Process parameters definitions

Evaluating thermal and hydraulic performance requires clear definitions of the key process parameters that describe fluid flow and heat transfer. Defining these parameters enables consistent analysis across different flow conditions. This section introduces the several key process parameters used in this study.

The Reynolds number of the flow in the ducts of ICTs is defined based on the hydraulic diameter (D_h), given by Eq. (4.7):

$$\mathrm{Re}_h = \frac{u_m D_h}{\nu} \tag{5.1}$$

Here, u_m is the mean velocity:

$$u_m = \frac{\dot{m}}{\rho A_{cs}} \tag{5.2}$$

where $\dot{m}$ represents mass flow rate, ρ is fluid density and A_{cs} is the cross-sectional area of a duct. The hydraulic diameter is based on the wetted perimeter or hydraulic perimeter P_h. A_{cs} and P_h are determined using numerical integration, as outlined in Section 4.2, based on equations Eqs. (4.3)–(4.5) and Eqs. (4.8)–(4.11), respectively.

The Fanning friction factor is expressed by:

$$f = \frac{D_h \Delta p}{2 \rho {u_m}^2 l} \tag{5.3}$$

where Δp is the difference between the surface-averaged pressure values at the inlet and outlet boundaries.

Nusselt number based on equivalent diameter (D_e) is defined as follows:

$$\mathrm{Nu}_e = \frac{h_{avg} \cdot D_e}{\lambda_f} \tag{5.4}$$

D_e is defined by Eq. (4.6) and it is based on the equivalent perimeter (cf. Section 4.2). h_{avg} represents the surface-averaged heat transfer coefficient:

$$h_{avg} = \frac{q}{T_W - T_b} \tag{5.5}$$

Here, q is heat flux per unit area [W/m^2] in the direction normal to the wall, T_W is the mean wall temperature determined as the surface average temperature of the interface between the fluid and the solid wall, and T_b is the mean bulk temperature. The latter was calculated by averaging over the cross-sections, either in the core region or in the channel, as follows:

$$T_b = \frac{\int_{A_{cs}} u\,T\,dA}{\int_{A_{cs}} u\,dA} \tag{5.6}$$

where A_{cs} indicates the cross-sectional area.

5.2 Experimental Study

Since ICT1 and ICT2 are based on similar design principles, ICT1 was selected for experimental studies to reduce research expenditure and resources. The experimental data obtained with ICT1 was used to validate the corresponding CFD model. Subsequently, the numerical results obtained from the validated CFD model for ICT1 were employed to develop new correlations which are presented in Chapter 7. These correlations were then used to evaluate the accuracy of the CFD model for ICT2.

The experimental study is conducted under both turbulent and laminar flow conditions, with a primary focus on the measurements of pressure drop and temperature in the ICT1. Before these measurements, two additional experimental investigations were performed: a study of maldistribution in the ICT1 channels and a characterization of flow type within the ICT1 ducts.

5.2.1 Manufacturing and assembly of ICT1

The ICT1 heat exchanger was manufactured using an extrusion process. This method is highly accurate and capable of producing complex cross-sections that are uniform along the entire length of the fabricated part. Additionally, it yields excellent surface finishing, resulting in smooth surfaces—a beneficial attribute that reduces pressure drops in heat exchangers and minimizes fouling or heat transfer resistance caused by surface roughness.

The extruded ICT1 configuration was created in Computer-Aided Design (CAD) software based on profiles of the inner and outer curves (cf. Chapter 4). The ICT1 fabricated for experimental testing consists of a 1-meter-long tube with six channels (cf. Figure 5.6a) and two headers at each end. The headers were fabricated separately from ICT1, and each header was partitioned into two parts produced by CNC machines (Figure 5.6b). Furthermore, there are three couplings for each header, that can be mounted on the headers using bolts (Figure 5.6c, d, f). Pipelines can be connected to couplings to supply fluid to ICT1 ducts (Figure 5.6g).

Aluminium (alloy 6063Al) was selected as the construction material for ICT heat exchanger due to its high thermal conductivity. This alloy is one of the most common materials used in aluminium extrusion processes (Abdul-Jawwad & Bashir, 2011) and it is also the most cost-effective manufacturing material. In addition to its ability to form complex shapes with remarkably smooth surfaces, this alloy has excellent thermal and mechanical properties (ASM Handbook-ASM International, 1990). The thermal conductivity of the 6063Al alloy is 202.4 W m^{-1} K^{-1}.

Following the manufacturing process, ICT1 parts were assembled using a high-quality epoxy resin (specifically Araldite type) (cf. Figure 5.6e, f, g). The use of epoxy is more practical compared to welding, as it allows for the disassembly of the header parts, facilitating easy re-installation or maintenance during experimental procedures. Moreover, epoxy provides excellent sealing for internal regions that are difficult to access, especially when welding or other methods are employed. Besides, welding would result in a rough surface on the edges which is undesirable for fluid flow. During the assembly process, synthetic clay (green color shown in Figure 5.6e) was used to prevent the epoxy resin from seeping into the channels. Once the epoxy was fully cured, the clay was easily removed, and a smooth surface finishing was achieved by sanding. A liquid sealant was applied to enhance the seal between the header and coupling, which is shown in black-colored material in Figure 5.6f.

The geometrical parameters of the ICT1 ducts (e.g., channel cross-sectional areas and hydraulic diameters) are determined using numerical integration methods. This integration is based on the inner and outer curve functions that describe the ICT channel shape (cf. Chapter 4). The detailed specifications for the dimensions and geometrical parameters of the fabricated ICT1 exchanger can be found in Table 5.1.

(a)

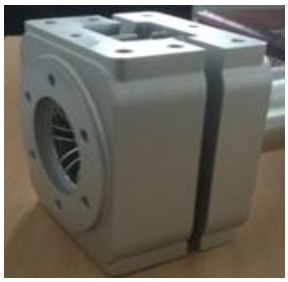

(b)

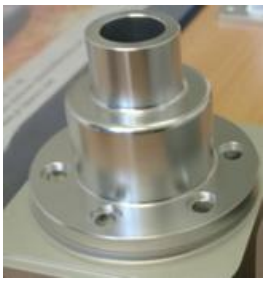

(c)

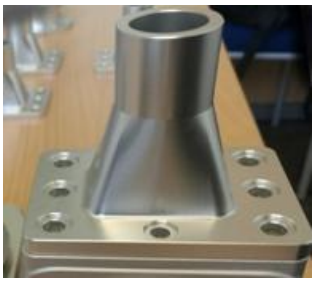

(d)

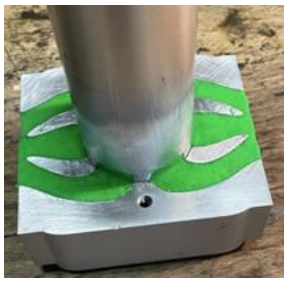

(e)

(f)

(g)

Figure 5.6: The photos of investigated ICT heat exchanger: internally channeled tube (a); header parts (b); core region coupling (c); channels coupling (d); assembling header linked with ICT using synthetic clay (green color) to prevent epoxy resin from extending into the channel (e); coupling attached to the header (f); a header ports connected to the pipe lines (g).

Table 5.1: Dimensions and parameters of the tested ICT1 exchanger

Parameter		**core region**	**per channel**
cross sectional area (A_{cs}) [mm^2]	-	501.6	96.97
hydraulic diameter (D_h) [mm]	-	9.53	9.51
inner diameter (d_1) [mm]	40		
outer diameter (d_2) [mm]	46		
wall thickness [mm]	1.00		
total length l [mm]	1000		
test section [mm]	500		

5.2.2 Experimental set-up

5.2.2.1 Turbulent flow

The experimental testing environment utilized for conducting measurements is located in the laboratory of the Chair of Fluid Process Engineering at Paderborn University. Figure 5.7 shows the experimental unit built to study the thermohydraulic performance of the ICT1 heat exchanger. The unit consists of various components, including an ICT1 heat exchanger, flow meters, differential pressure sensors, thermocouples, thermostats, a steam generator, tanks, pumps, a pipeline system, and two plate heat exchangers for controlling inlet temperatures. Additionally, a third heat exchanger is used to provide hot water by utilizing vapor from the steam generator. The LabVIEW interface is employed for data monitoring and is programmed to operate the flow meters, thermocouples, electrical control valves and pressure sensors.

The experiments were carried out in countercurrent mode using water as working fluid for both the hot and cold sides of the ICT1. The experimental facility was designed as a closed-loop system with four loops, including a hot-water loop, a cold-water loop, and two pre-cooling/heating loops. Hot water passes through the core region, whereas cold water flows in the channels of ICT1. ICT1 headers are equipped with three flow ports. At the right-side header shown in Figure 5.8a, there are two inlets for cold water (marked blue) and one outlet for hot water (marked red). The header on the left side of the ICT also has two cold water outlets (blue) and a hot water inlet (red). This allows for countercurrent flow to be defined in which the working fluids flow in opposite directions.

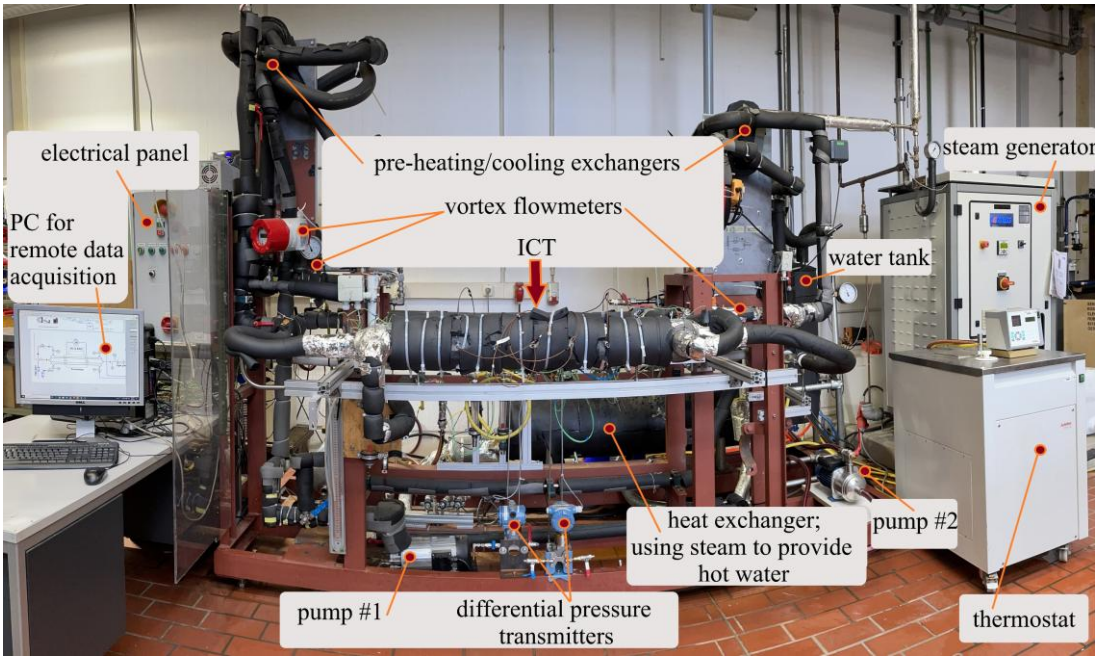

Figure 5.7: The photo of the experimental facility for testing ICT1 heat exchangers.

Vortex flowmeters with a flow capacity range of 3.5 to 50 l/min regulate the flow of cold water through the two inlets. Each inlet port provides cold water to three channels of the ICT1, so that all six channels are covered. A vortex flowmeter with a flow range of 3.3 to 82 l/min controls the hot water flow at the inlet of the left-side header (cf. Figure 5.8a). The flow inlet temperatures are regulated by the two pre-cooling loops using plate heat exchangers (see Figure 5.8a). Furthermore, proportional electric and manual valves are installed to adjust the flow passing through the flowmeters and pre-cooling/heating loops.

The experimental facility is equipped with a pair of differential pressure flow transmitters, Rosemount 3051, which are used to measure pressure losses within ICT1 ducts. Pressure losses of the fluid passing through the ICT1 heat exchanger are mainly caused by skin friction. The pressure drop is only measured in the middle part of ICT1 (Figure 5.8 “test section”), where the flow is expected to be stabilized. Consequently, pressure drop caused by the inlet and outlet ports is excluded. Further, as the ICT1 is mounted horizontally, pressure drop due to gravitational effect can be neglected. The first transmitter is connected to the core-region duct, while the second one is installed at one of the six ICT1 channels. It is assumed that the flow is to be the same across all channels. The range of the differential pressure transducers is up to 10 mbar.

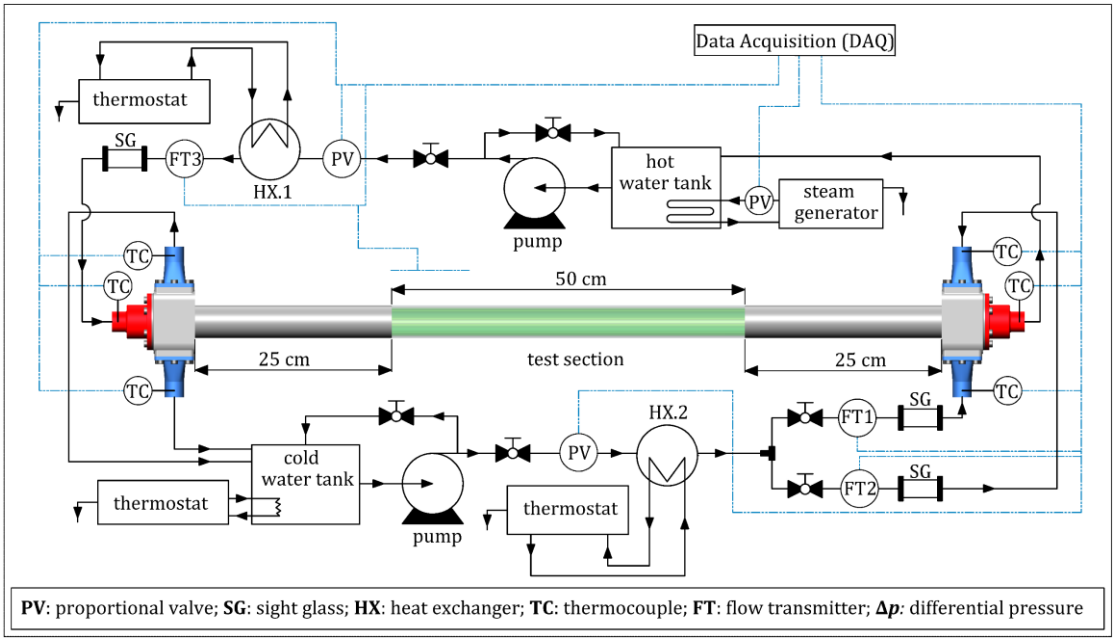

(a)

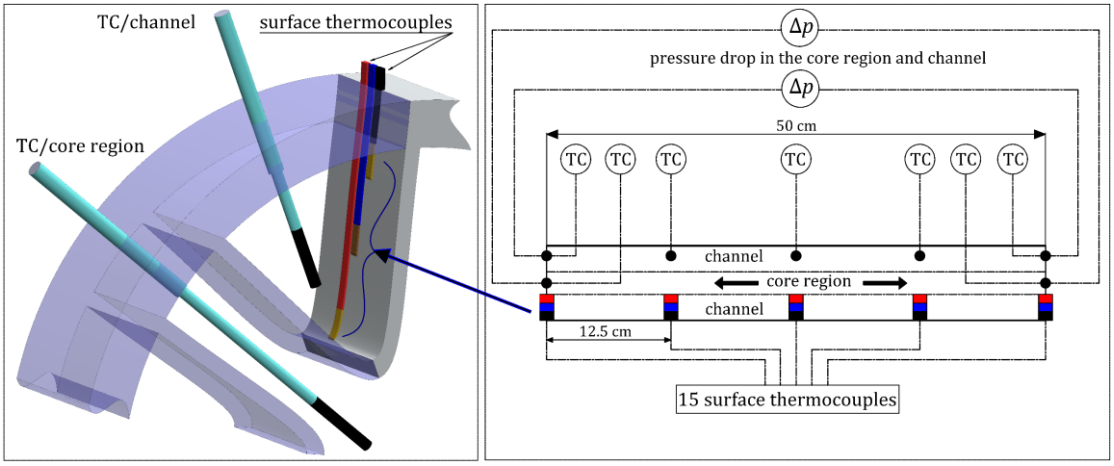

(b) (c)

Figure 5.8: Schematic of the experimental set-up: general scheme (a); installation of thermocouples in the core region and channel (b); test section (c).

The inlet and outlet bulk temperatures of hot and cold water are measured directly at the ports and within the test section of the ICT1 by using thermocouples (cf. Figure 5.8b). The surface-thermocouples are carefully installed inside the 1mm internal walls. This is done by placing them into a milled groove to prevent convective effects on the measured temperatures due to protrusions (flow obstruction). The groove is sealed with thermal adhesive of high quality and a smooth finish is achieved by brush sanding. In this way,

thermocouples can be positioned fixedly and reading stability can be ensured. Fifteen surface thermocouples are used and fixed at five positions on the channel surface along the test section to measure the wall temperatures. The distance between two longitudinal locations is 12.5cm, as illustrated in Figure 5.8c (test section). To capture the temperature distribution along the curved interior surface of the channel wall, three surface-thermocouples are mounted on the wall at each longitudinal location (cf. Figure 5.8b, c). All thermocouples used in this experiment are type K produced by THERMA GmbH. They were calibrated in our laboratory with standard thermometers.

The installation of surface thermocouples on the interior walls of ICT1 was challenging, as the channels and core region are fully enclosed. Access to the interior wall to install the thermocouple was achieved by cutting a slot of the outer surface in one of the six channels and closing this slot after installation with a precisely fitting 3D-printed aluminum cover. This was done without causing any damage to the ICT1 structure. Further, the entire outer surface of ICT1 was well insulated with three layers of rubber and fibrous insulations to minimize heat losses.

The experiments were conducted for two different temperature combinations at the header inlets, building two cases studies described in Table 5.2 (case I and case II). Fixed inlet temperatures for cold and hot water were 30ºC and 50ºC in case I and 10ºC and 65ºC in case II. The mass flow rate varied between 0.21 and 0.41 kg/s in the core region and between 0.035 and 0.068 kg/s per single channel.

Table 5.2: Conditions for turbulent flow and the fluid properties

Property/Variable	**Cold water (per single channel)**		**Hot water**	
	case I	case II	case I	case II
inlet temperature T [ºC]	30	10	50	65
specific heat c_p [J kg^{-1} K^{-1}]	4183	4188	4181	4184
density ρ [kg m^{-3}]	995.7	999.7	988	980.6
viscosity μ [Pa s]	0.000797	0.001307	0.000547	0.000433
thermal conductivity λ_f [Wm^{-1} K^{-1}]	0.6060	0.5674	0.6530	0.6455
mass flow rate [kg s^{-1}]	0.035 to 0.068		0.21 to 0.41	

During each measurement, the same mass flow rates were applied to the core region and the six channels. In both cases, the applied mass flow rates cover the Reynolds number range $2500 \leq Re \leq 18000$. The Reynolds number of the flow in the ICT1 ducts is based on the hydraulic diameter, according to Eq. (5.1). The summary of the experimental conditions along with the assumed water properties are given in Table 5.2. The water properties at each inlet temperature were assumed to be constant along the length of ICT1.

5.2.2.2 Laminar flow

In the laminar flow experiments, the experimental setup previously used for turbulent flow and described in Section 5.2.2.1, is employed for this flow condition. However, an adjustment is made to the previous setup by replacing the flowmeters with ones featuring a lower flow range. Specifically, the cold fluid pumped to the ICT1 channels through two inlets is now regulated by vortex flowmeters with a flow range of 0.5 to 10 l/min. Similarly, the hot fluid supplied to the core region is controlled by a vortex flowmeter with a flow range of 0.9 to 15 l/min.

In complex duct geometries, such as the core region, the measured bulk temperature is highly sensitive at low Reynolds numbers. Laminar flow adheres to duct walls, forming boundary layers that rarely interact, which hinders efficient mixing. In contrast, turbulent fluctuations at high Reynolds numbers enhance fluid mixing (Kadoch et al., 2020). To address potential poor mixing in laminar flow, customized thermocouples were developed specifically for measuring bulk temperatures in the core region. These thermocouples can simultaneously take three readings at different radial positions within the core region, as illustrated in Figure 5.9, ensuring reliable bulk temperature measurements.

Under the laminar flow conditions, the experiments were conducted with inlet temperatures set at 20 °C for the cold fluid and 50 °C for the hot fluid. Reynolds number varied from 1000 to 2000 in the core region and channels. The mass flow rates used in the experiments were adjusted according to Eqs. (5.1) and (5.2). These adjustments ensured that the assumed Reynolds numbers matched those employed in the simulations.

Water was selected as the process medium for the channel ducts of the ICT1. In the core region, the sensible frictional pressure drop is relatively low at small Reynolds numbers. To elevate the recorded pressure values, it became essential to increase the flow

rate, thereby ensuring precise measurements and minimizing uncertainties. Therefore, a mixture of water and glycerin was used as the working fluid in the core region to augment the viscosity of the hot fluid. This adjustment facilitates the attainment of laminar flow conditions with higher flowrates at the same given Reynolds numbers in the core region. The volume fraction of glycerin was 26%. The properties of the fluids are given in Table 5.3. They were assumed to be constant throughout the length of the ICT1. The viscosity of the water-glycerin mixture at the specified volume fraction and temperature was determined in the laboratory through the utilization of a rotational viscometer. Other mixture properties were obtained from (Glycerine Producers Association (1975); Takamura et al. (2012)).

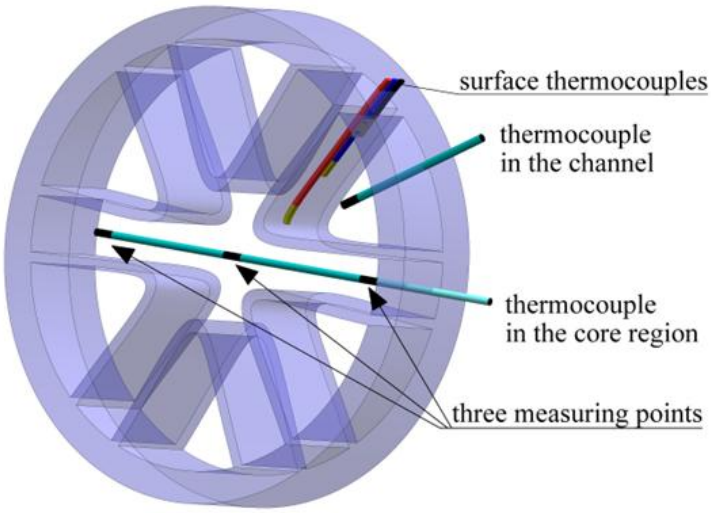

Figure 5.9: Schematic of installations of the thermocouples.

Table 5.3: Conditions for laminar flow and the fluid properties.

Duct flow	**Medium**	**Properties**					
		T [°C]	ρ [kg m^{-3}]	μ [Pa s]	c_p [J kg^{-1} K^{-1}]	λ_f [Wm^{-1} K^{-1}]	Pr [-]
core region	water-glycerin mixture	50	1120	0.0012	3700	0.55	8.14
channel	pure water	20	998.2	0.0011	4183	0.586	7.85

5.2.3 Uncertainty analysis

Uncertainty analysis is essential in scientific research for systematically evaluating and quantifying potential variations, inaccuracies, or errors in measured data and derived parameters (Willink, 2022). This analysis ensures the reliability and precision of findings by addressing the inherent limitations and variability in measurements. In this study, the uncertainty in the measured parameters was evaluated using the method developed by Kline and McClintock (1953). This method offers a systematic approach to identify the variations that might arise from various factors, thereby providing more understanding of the overall uncertainty in measurements. To minimize systematic uncertainties in flow, pressure, and temperature measurements, a calibration process was employed. This calibration procedure adjusts the measurement equipment, including thermocouples, vortex flowmeters, and pressure transducers, to correspond with known reference standards. This procedure effectively reduces biases and inaccuracies in the readings, ensuring greater precision and reliability in the experimental data.

The systematic or bias errors associated with the equipment used are given in Table 5.4. The total relative uncertainties of the calculated parameters are provided in Table 5.5 with a confidence level of 95%. These uncertainties include both the systematic errors from equipment and the statistical errors inherent in the measurements. A 95% confidence level means that the calculated uncertainties reflect the anticipated variations in the measurements, within a specified level of confidence.

Table 5.4: Ranges and accuracies of the used instruments.

Instrument	Range	Application	Bias/ Accuracy
flowmeters	3.3 to 82 l/min	turbulent/hot-sides	±0.7% of full scale
	3.5 to 50 l/min	turbulent/cold-sides	±0.55% of full scale
	0.5 to 10 l/min	laminar /cold sides	
	0.9 to 15 l/min	laminar /hot sides	
differential pressure sensors	0.0 to 10 mbar	used in both laminar and turbulent flow conditions	±0.2% of set span
wall thermocouples	- 40 to 375 °C		±0.5°C
bulk thermocouples	-100 to 1100 °C		

A detailed uncertainty analysis, along with careful calibration of flow, pressure, and temperature instruments, can ensure the accuracy and reliability of the measurements conducted on the ICT1 heat exchanger. This supports confidence in the reported data and the validity of the experimental conclusions.

Table 5.5: Uncertainties of measured quantities and calculated parameters.

Parameters	**Relative & absolute uncertainty**	
	turbulent	laminar
mass flow rate, $\dot{m}$ [kgs^{-1}]	4%	5.5%
heat transfer rate, Q [W]	4.4%	5.42%
average heat transfer coefficient, h_{avg} [Wm^{-2}K]	4.4%	5%
pressure drop, Δp [Pa]	1.1%	4%
Temperature [°C]	±0.5	±1.5

5.2.4 Maldistribution in the channels of the ICT

5.2.4.1 Set-up

Maldistribution refers to the phenomenon of nonuniform flow distribution, in either one or both branches (e.g. headers) of a heat exchanger, which can significantly reduce its performance (Niroomand et al., 2021). Improper header design or blockage in certain flow passages are the major causes of increased flow maldistribution (Kumaran et al., 2013). For this reason, the flow maldistribution in the ICT1 channels (cf. Figure 5.8 (section B-B)) was experimentally evaluated before proceeding with any pressure and temperature measurements.

The evaluation of the maldistribution was conducted only for the cold fluid flow in the channels, since each inlet in the header shown in Figure 5.8 and Figure 5.10 distributes water among three ICT1 channels (cf. Section 5.2.2). This irregular distribution may adversely affect the overall performance of the ICT1 heat exchanger, leading to a significant reduction in its efficiency (Shao et al., 2018). To enhance flow distribution within the channels and mitigate the effects of maldistribution, the header shown in Figure 5.10 is equipped with two guide blades at each inlet. This configuration promotes a more

uniform flow distribution across all channels. The guide blades shown in Figure 5.10 were optimized based on preliminary CFD simulations. The optimization included a modification of both the leading edge and blade profile along with adjusting the gap size between the blades (cf. Figure 5.10).

In the experimental set-up, an additional header with three exits was necessary to measure maldistribution within the ICT1 channels (see Figure 5.11a). This allows flow through each channel to leave the ICT independently. In this way, it was possible to measure the flow rate of fluids passing through each individual channel, as shown in the schematic of experimental set-up (Figure 5.11b). Further, since both header inlets shown in Figure 5.10 are identical, only one of them was tested (inlet_1). After having performed the maldistribution measurements, the header with three exits was removed and replaced with the second header as shown in Figure 5.8a.

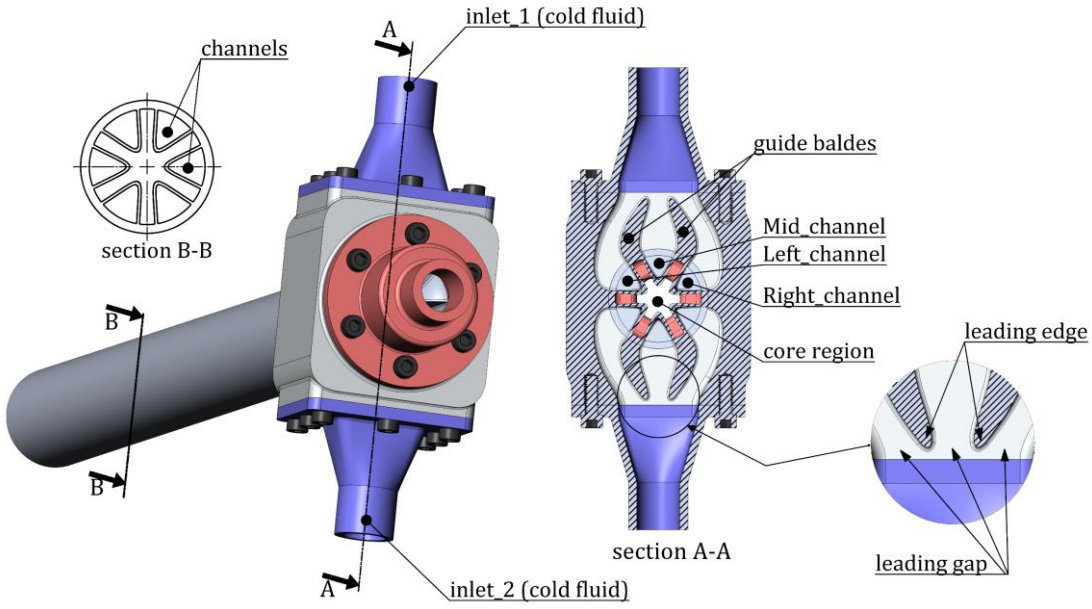

Figure 5.10: A schematic of ICT header and a cross-section of the guide blades

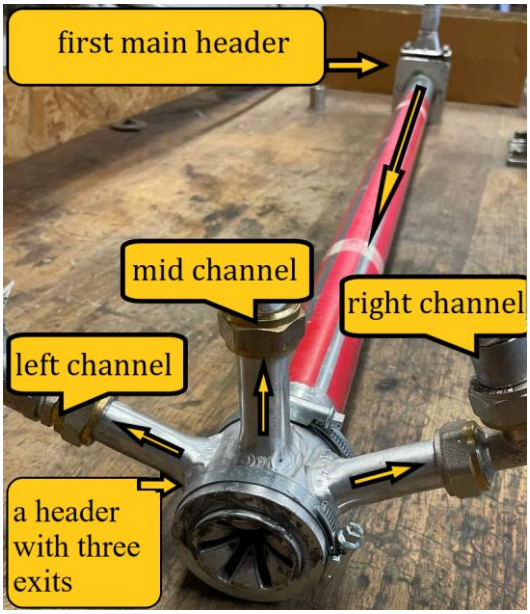

(a)

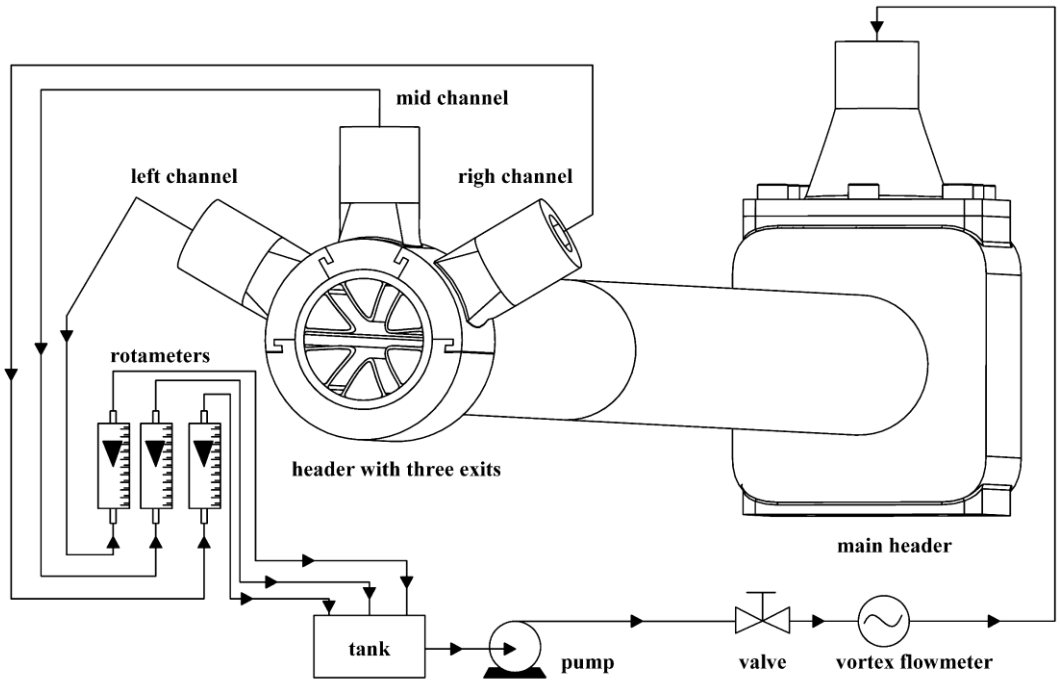

(b)

Figure 5.11: Evaluation of maldistribution in the channels of ICT: a photo of an ICT header with three exits, positioned at one end of the ICT tube, used for maldistribution measurements (a); a schematic of the experimental set-up for measuring maldistribution (b).

5.3 Results and discussion

5.3.1 Grid independence study

Grid independence study was carried out using five different grid resolutions to ensure the accuracy and reliability of the CFD simulations. The analysis of ICT1 revealed that increasing the number of cells to more than 24 million, with a refinement ratio (finer mesh to coarser mesh) of 1.3, brought about just small differences in the average heat transfer coefficients, namely 0.02 % for core region and only 0.0076 % for channel region.

A similar study was performed for ICT2, while the number of cells was increased to more than 28 million with the same refinement ratio. The differences in average heat transfer coefficients for the core and channel regions were 0.036 % and 0.0027 %, respectively. For pressure drop, the grid independence study showed similar results, namely a 0.014 % difference for core regions and a 0.003 % difference for channels, when the number of cells increased to over 24 million for ICT1 and 28 million for ICT2. The grid independence study was conducted for the highest Reynolds numbers Re ≈ 39000 in the core region and Re ≈ 9000 in the channel. The grid resolution can be assumed good for the lower Reynolds numbers applied.

Simulation convergence was determined by the order of magnitude of the residuals. The convergence criterion was considered satisfied when all scaled residuals were below 10^{-10}. Such a convergence was reached within a maximum of 300 iterations.

5.3.2 Evaluation of the domain-splitting approach in CFD simulations

As previously described in Section 5.1.1, the ICT computational domain of 1 m total length was sub-divided into three elements: a "middle" element (ME) of 0.5m and two "entrance" elements of 0.25m each. This domain-splitting approach was adopted to enable simulations to be executed on systems with limited processing capacity—whether local workstations or computational clusters—by reducing the number of processors required per run. Crucially, this was achieved without compromising mesh density or quality, thus preserving the ability to accurately capture the fluid dynamics and heat transfer behavior within the ICT ducts.

Numerical simulations were performed for both the full-length ICT domain and the partitioned-domain configuration, illustrated in Figure 5.12, ensuring consistent mesh

density and total element count across the two models. These simulations were conducted for specific Reynolds numbers under both turbulent and laminar flow conditions. For the full-length simulations—covering the entire spatial domain—the same boundary positions defined in Figure 5.2 for the domain-splitting approach were used to specify the inlet and outlet conditions, shown in Figure 5.12 (top). Specifically, boundaries at positions 1 and 7, described in Figure 5.2, were applied to the core region of the full-domain, while positions 3 and 5 were used for the channel flow boundaries. As in the split-domain model, zero-gradient conditions were applied for velocity and temperature at symmetry planes. No-slip (Dirichlet) conditions were used at walls, and an adiabatic condition was set on the outer-tube wall.

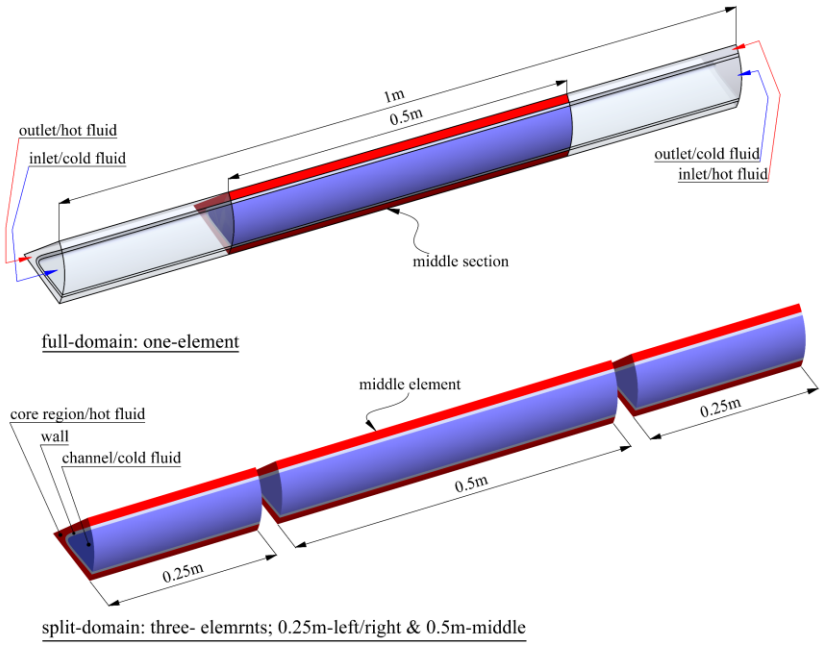

Figure 5.12: Schematic representation of full-domain (top) and splitting-domain (bottom)

The comparative results are illustrated in Figure 5.13 and Figure 5.14. The figures present the numerical friction factor and Nusselt number, each normalized with respect to its maximum value, to enable direct comparison. The numerical data for the friction factor and Nusselt number were obtained from the middle section of the full domain and the middle element (0.5 m) of the partitioned domain, both illustrated in Figure 5.12.

The comparative analysis reveals that the discrepancies between the full and partitioned domain results remain small across both laminar and turbulent flow conditions. Specifically, the friction factor predictions exhibit a maximum deviation of less than

0.04%, and the Nusselt number differs by approximately 0.05%. These quantified deviations are based on the data presented in Figure 5.13 and Figure 5.14, respectively.

Consequently, the comparative results confirm that the domain-splitting approach maintains high simulation fidelity for both friction factor and Nusselt number predictions in the ICT heat exchanger.

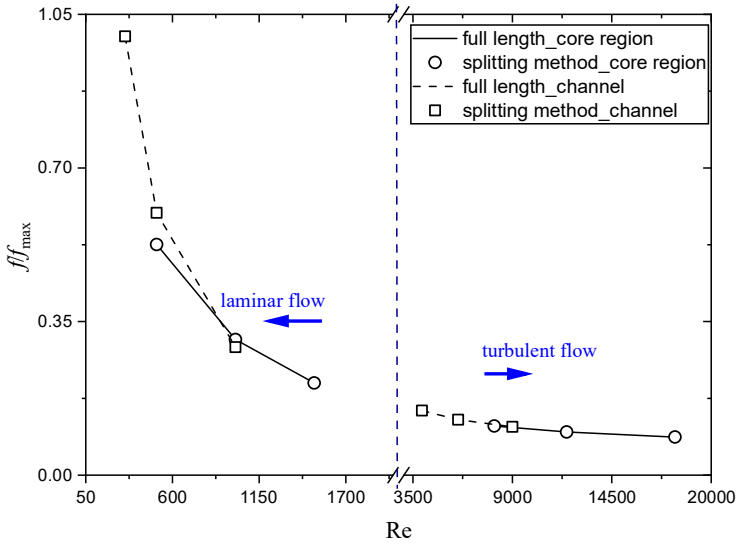

Figure 5.13: Normalized friction factor in the full domain and with splitting-domain under laminar and turbulent flow conditions.

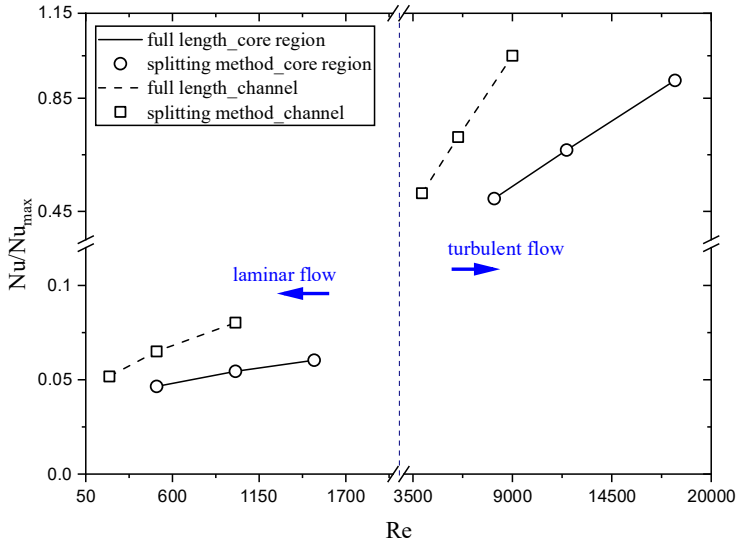

Figure 5.14: Normalized Nusselt number in the full domain and with splitting-domain under laminar and turbulent flow conditions.

5.3.3 Boundary layer distribution

In fluid dynamics, boundary layers are thin regions of fluid that interact directly with a surface (Tuncer & Bradshaw, 1977). In viscous fluids, hydrodynamic boundary layers form due to shear stress between the fluid and the solid surface, while thermal boundary layers are characterized by temperature gradients, indicating heat transfer and influencing fluid temperature during flow (Everts et al., 2023).

The insulation on the outer surface of the ICTs prevents heat transfer through that boundary, confining thermal exchange to the interior walls. This constraint modifies the thermal boundary layer structure and significantly affects the thermal behavior within the ICT ducts. As clearly seen in Figure 5.15a, thermal boundary layers are absent in the vicinity of the insulated outer walls. However, hydrodynamic boundary layers develop everywhere near all duct walls, as illustrated in Figure 5.15b. The hydrodynamic boundary layers can form even near insulated surfaces because they are driven by velocity gradients in the fluid. The thickness of these layers is determined by the fluid flow, and insulation has no significant impact on their formation.

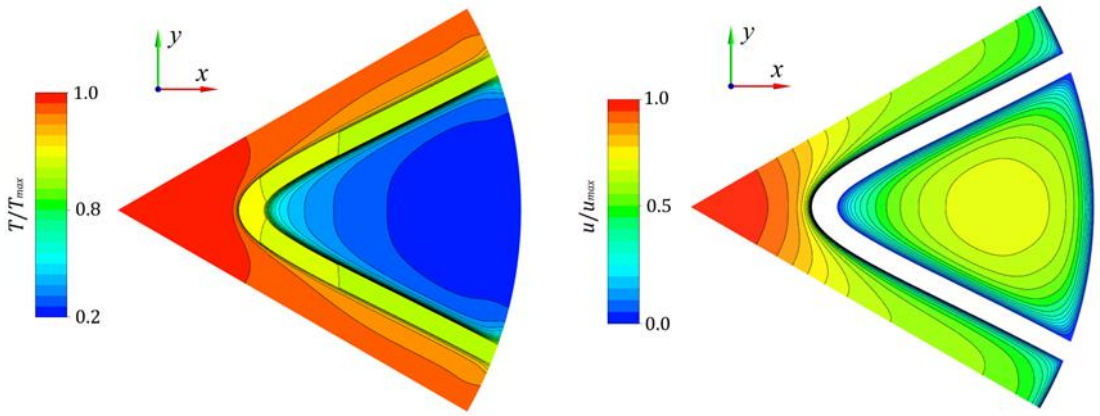

(a) (b)

Figure 5.15: Temperature and velocity contours of ICT1: thermal boundary layers (a); hydrodynamic boundary layers (b).

Thus, the insulation on the ICTs necessitates the use of two different length scales for calculating dimensionless parameters, as described in Section 4.2. For heat transfer calculations, the length scale is determined using the equivalent diameter, also referred to as the cooled or heated diameter (Duarte & Corradini, 2018), defined by Eq. (4.6). The

hydraulic diameter, given by Eq. (4.7), is used for calculating the friction factor and Reynolds number.

In this study, heat transfer within the ducts of ICTs was evaluated using the Nusselt number (cf. Section 7.2), with the length scale specifically defined to include only the perimeters or surfaces involved in heat transfer, thus ensuring precise and accurate prediction of thermal behavior.

5.3.4 Evaluation of the maldistribution

Designing an efficient header to distribute fluids across the complex geometry of ICT1 ducts was a critical step for the experimental study. As discussed in Section 5.2.4, maldistribution—uneven fluid distribution in one or both fluids within the heat exchanger branches—can significantly reduce the performance of heat exchanger. Optimizing fluid distribution within the ICT1 channels helps to minimize deviations between numerical and experimental results, enabling more accurate comparisons.

The initial phase of the experimental work focused on evaluating maldistribution exclusively within the ICT1 channels. This was essential because each of the two header ports supplies fluid to three separate channels (cf. Figure 5.16a). In this experiment, maldistribution was evaluated across a range of flow rates, covering both low-flow (laminar) and high-flow (turbulent) conditions, as characterized by a wide spectrum of Reynolds numbers. The volumetric flow rates measured in the ICT1 channels are presented in Figure 5.16. The results show that the flow rate in the mid-channel is approximately 1% to 2% higher than in the left and right channels at high Reynolds numbers. This difference increases to 4% when the total volumetric flow rate reaches 4 l/min (R≈1700) and exceeds this percentage for Reynolds numbers below 1000, reaching up to 6% at approx. R=985 (see Figure 5.16). A smaller percentage difference indicates a more uniform flow distribution.

In turbulent flow conditions at high Reynolds numbers, a 1% to 2% difference in flow rates between the mid-channel and the left-right channels is generally acceptable and has a minimal impact on the ICT1 performance. However, when the flow rate difference exceeds 6% at Reynolds numbers below 1000, it may significantly affect heat transfer processes. This issue becomes particularly critical during experiments with very low flow

rates, as some channels may receive insufficient fluid volumes. Consequently, this can lead to unbalanced heat exchange between the core region and the ICT1 channels, resulting in inadequate thermal energy distribution. Such imbalances may introduce inaccuracies in wall temperature measurements, especially since the surface thermocouples are mounted on the wall of one of the six channels, as detailed in Section 5.2.2.

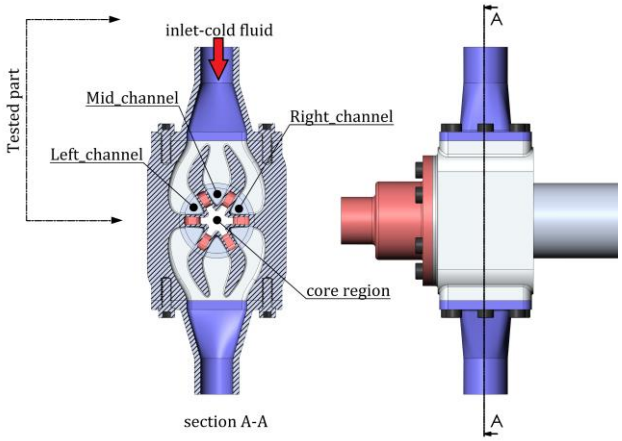

(a)

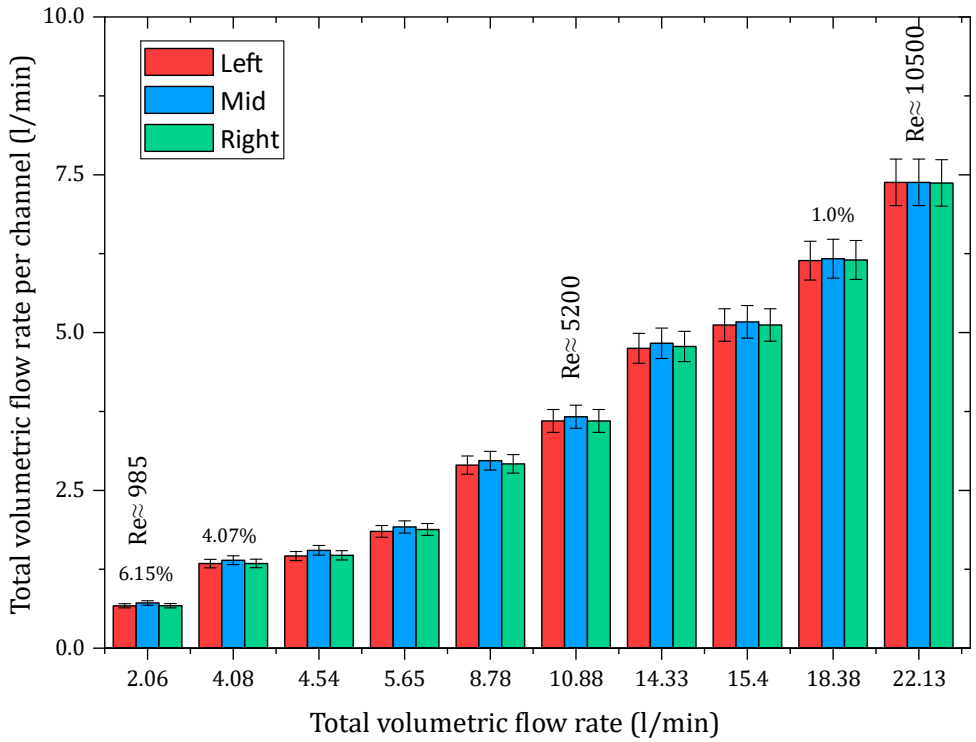

(b)

Figure 5.16: Maldistribution in the channels of ICT1: a schematic of tested part showing channels locations (a); measured volumetric flow rate distribution in individual channels of the ICT (b).

Given these challenges, the current header design may not be suitable for testing ICT1 below the Re=1000 threshold. To ensure the accuracy and reliability of experimental data, efforts were made to avoid or mitigate the effects of maldistribution by steering clear of very low flow rate conditions. As a result, a minimum Reynolds number of 1000 was maintained under laminar flow conditions during the experiments, conducted to measure pressure drop and temperatures.

5.3.5 Flow type characterization in the ICT1 ducts

The flow regime describes the specific pattern of fluid motion, which can vary from smooth and orderly (laminar) to chaotic and irregular (turbulent), with transitional phases in between (Evstigneev, 2020). Identifying the dominant flow pattern in a fluid system can be achieved through various methodologies and techniques. Flow visualization methods or pressure drop measurements are common ways (García et al., 2005; Kim et al., 2019). Visualization methods, which include adding tracer particles, or dyes and using transparent walls, offer qualitative insights into flow patterns (Kim et al., 2019). However, in the case of ICT1 ducts, visualization is challenging due to their enclosed structure and missing of transparent walls.

The second method involves pressure measurements in the core region and channels of the ICT1 ducts. These measurements provide valuable flow characteristics across different Reynolds numbers (García et al., 2005). Figure 5.17 illustrates the normalized friction factor (f/f_{max}) plotted against the Reynolds number. The friction factor is determined based on Eq. (5.3). The calculated friction factor values are normalized using the corresponding maximum value f_{max}. The latter is obtained based on the measured pressure drop in the core region and channel at Reynolds numbers of 2000 and 1500, respectively. According to Figure 5.17, the transition flow turns to turbulent flow at Re≈ 2000 in the core region, whereas the critical Reynolds number—marking the threshold at which laminar flow shifts to transitional flow—is approx. 1800. For the channels, the flow becomes turbulent at Re≈ 2150; the critical Reynolds number is Re ≈ 2000.

For a Reynolds number below the critical value, laminar conditions dominate. As a result, the friction factor demonstrates an inverse relationship with the Reynolds number, decreasing approximately in a linear fashion as the Reynolds number rises. Transitional flow is characterized by a sudden increase in friction factor due to the emergence of

disturbances in the flow. Once the flow is completely turbulent, the friction factor drops again (cf. Figure 5.17).

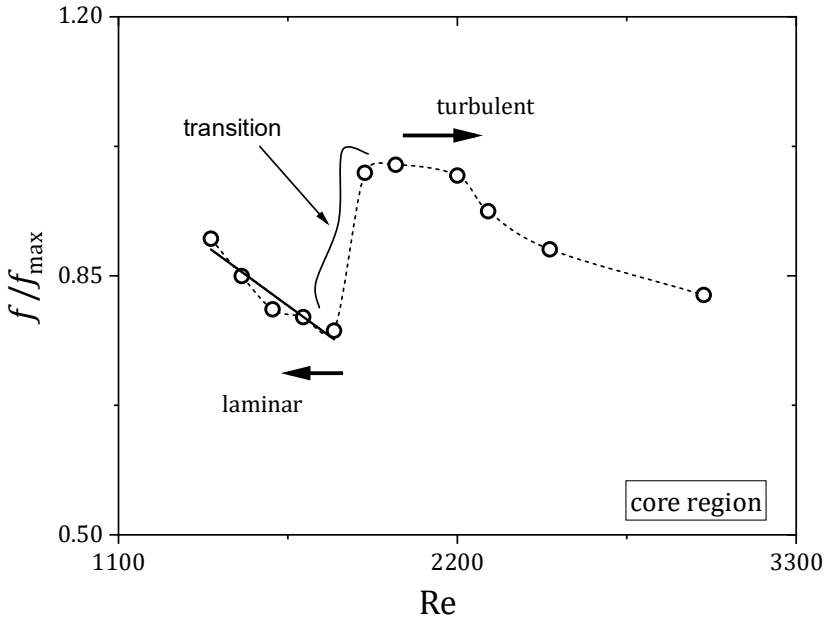

(a)

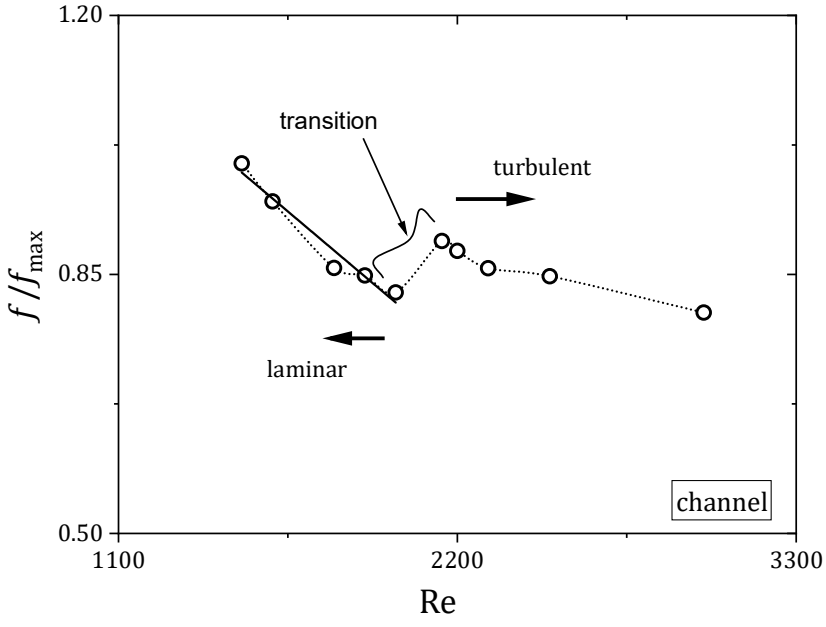

(b)

Figure 5.17: Normalized experimental friction factor vs. Reynolds number: the core region flow (a); the channel flow (b).

5.3.6 Validation of CFD model

This section presents the validation of the CFD model applied to the ICT1 heat exchanger, using experimental data obtained for both turbulent and laminar flow conditions. The evaluation of the numerical friction factor was accomplished using measured pressure drops, while the heat transfer was assessed based on the measured wall and bulk temperatures.

As mentioned in Section 5.1.1, the thermohydraulic data was collected exclusively within the 50 cm test section of the ICT exchangers, as illustrated in Figure 5.8. The flow in the ducts develops over a short entrance length, typically reaching stabilization at the mid-section of the ICTs (test section, 50 cm from the inlet). Therefore, the left and right entry regions, along with the headers (each 0.25m in length), were excluded from the pressure drop and temperature measurements.

5.3.6.1 Pressure drop

The friction factors within both the core region and channel of ICT1 were determined using Eq. (5.3), based on pressure drop values measured in the experiments. The pressure differences were determined between the inlet and outlet of the test section (mid-section, at a distance of 50 cm) using a differential pressure sensor, as described in Section 5.2.2. The measurements were conducted under the operation conditions specified in Table 5.2 and Table 5.3.

The experimentally determined friction factors under turbulent flow conditions were compared to those obtained from CFD simulations. As shown in Figure 5.18, numerical and experimental results are in a good agreement across the entire studied Reynolds numbers range ($2500 \leq Re \leq 18000$). The maximum deviation for the friction factor is less than 6.5% for both the core region and the channels. This demonstrates that the utilized CFD model effectively captures the fluid dynamics within the ICT1 ducts under turbulent flow conditions.

For laminar flow conditions, the comparison between experimental and simulated friction factors also showed acceptable agreement. The friction factor values, presented in Figure 5.19, were calculated based on measured pressure drops at Reynolds numbers ranging from 1400 to 1800 in the core region and from 1500 to 2000 in the channels. These

Reynolds number ranges were selected based on the findings discussed in Sections 5.3.4 and 5.3.5. As shown in Figure 5.19, the maximum deviation observed between numerical and experimental friction factors was 11% for both the core region and channels.

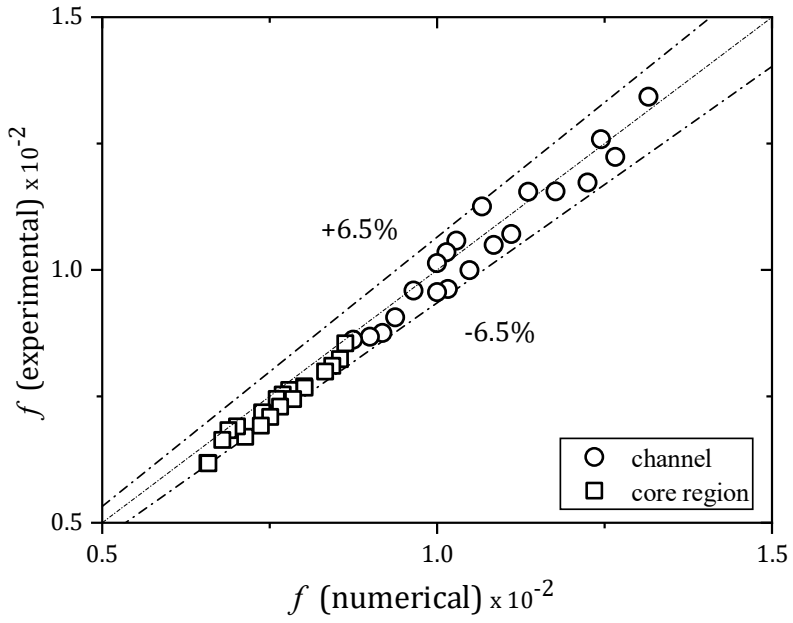

Figure 5.18: Parity plot of numerical and experimental friction factors under turbulent flow conditions.

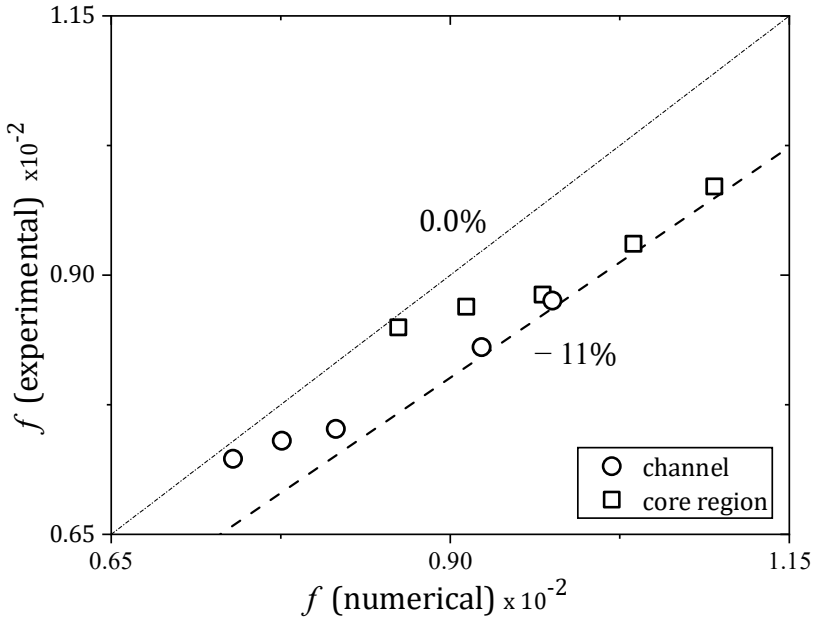

Figure 5.19: Parity plot of numerical and experimental friction factors under laminar flow conditions.

5.3.6.2 Heat transfer

The temperature distribution along the test section of the ICT1 ducts, both on the wall and in the bulk flow, was studied experimentally and compared with numerical simulations. The average deviation between the experimental and simulated temperature values was calculated using the following expression:

$$\text{average deviation (\%)} = \frac{1}{N}\sum_{i=1}^{N}\left|\frac{Y(i)_{exp} - Y(i)_{nu}}{Y(i)_{exp}}\right| \tag{5.7}$$

Here, Y_{exp} is an experimental value, Y_{nu} is the corresponding simulated value, N is the total number of data points used in the comparison, and i denotes the index of each data point.

The wall temperature on the channel surface was determined numerically by resolving the entire boundary layer, including the viscous sublayer and the buffer layer. Experimentally, as detailed in Section 5.2.2, the wall temperature distribution was measured along the curved interior surface of the channel using three surface thermocouples mounted on the channel wall at each longitudinal location of the test section. Measurements were conducted on the cold side (channel) to avoid damaging the ICT1 structure while ensuring accurate installation of the thermocouples. The wall temperature values presented in Figure 5.20 and Figure 5.21 represent the average of these three measurements for each position. Both turbulent and laminar flow conditions were studied, following specified conditions outlined in Sections 5.2.2.1 and 5.2.2.2.

Figure 5.20 illustrates the local wall temperature distributions under turbulent flow conditions for both cases given in Table 5.2. Arrows indicate the flow direction in the channels. A very good agreement between the numerical and measured wall temperatures is evident for both cases studied. In case I (Figure 5.20a), the maximum average deviation is approximately 1.5%, while in case II (Figure 5.20b), it is below 5%. The somewhat higher value in case II can probably be attributed to an increase in thermal resistance between thermocouples and thermal adhesive used. This effect can become more significant if the temperature difference between the hot and cold fluids increases as in case II (cf. Table 5.2). Similar deviations were observed across all tested inlet mass flow rates; therefore, results are presented only for four representative cases that capture the overall trend.

Figure 5.21 shows the wall temperature distributions along the test section under laminar flow conditions. The Reynolds number was maintained at a constant value of Re= 1500 in the core region, while it varied in the channel flow, with Re values of 1000, 1500, and 2000. A comparison between the measured and simulated wall temperatures revealed a maximum average deviation of approximately 7.5%.

Figure 5.22–Figure 5.24 demonstrate the measured and simulated bulk temperatures in the ICT1 ducts. The bulk temperatures in the channel were measured at five locations, whereas in the core region, they were determined using only two thermocouples placed at the ends of the test section, as described in Section 5.2. The bulk temperature is plotted along the test section of ICT1 at total mass flow rates ranging from 0.21 kg/s to 0.041 kg/s in the core region and the six channels. The results in Figure 5.22 to Figure 5.24 show a nearly linear relationship between the bulk temperature and the dimensional channel length. The temperature increases steadily with the distance from the channel inlet, while the bulk temperature in the core region decreases due to heat transfer from the hot water to the cold water during the heating process.

For the turbulent flow, a good agreement between the CFD results and measured bulk temperatures was found for both cases, with maximum average deviation of less than 5.5% for channel flow and 1% for the core region (cf. Figure 5.22 and Figure 5.23). The plots present data for only four mass flow rates, while similar deviations are observed for other values. Arrows indicate the flow direction in the core region and in channels. In the laminar flow, the maximum average deviation between the measured bulk temperature and that obtained from CFD simulations is approximately 8%.

Based on the reasonable agreement with measured temperatures, the CFD model can be considered capable of accurately capturing the thermal performance of the ICT1 ducts under both laminar and turbulent flow conditions. This thermal validation provides a reliable basis for using the model in future design studies, performance evaluations, and optimization of ICT configurations.

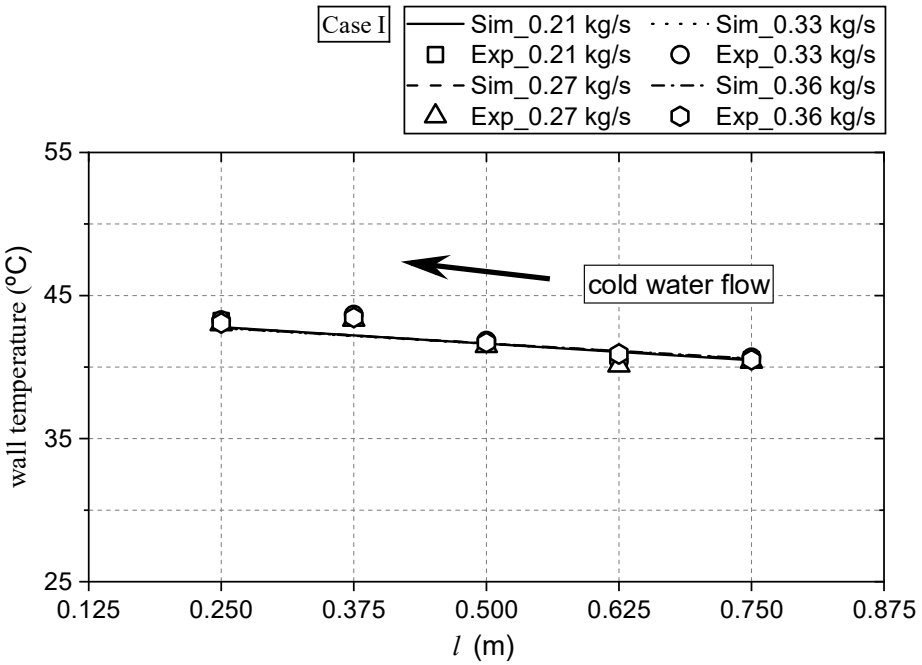

(a)

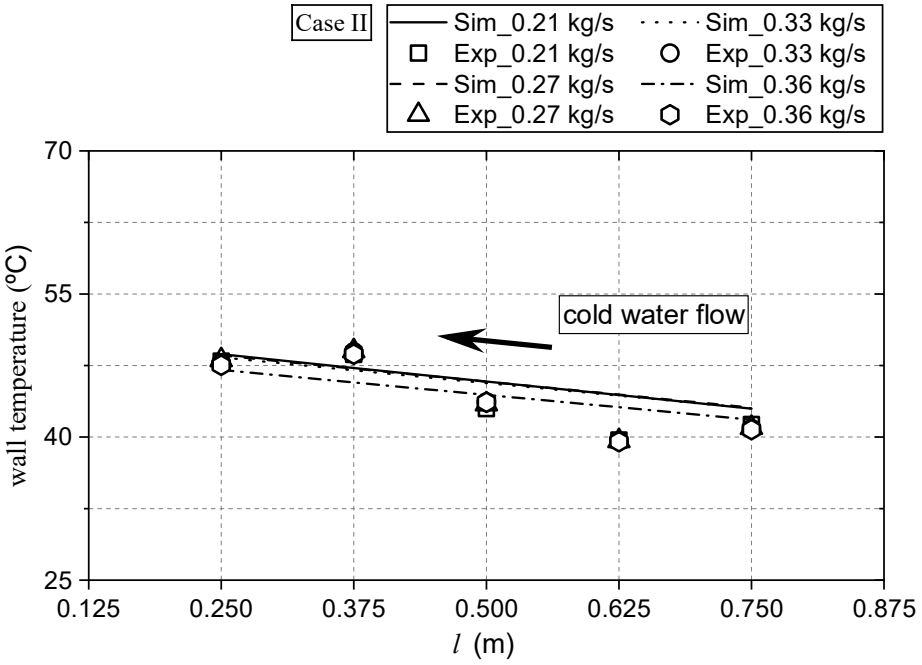

(b)

Figure 5.20: Simulated and measured wall temperatures along the ICT test section under turbulent flow conditions: case I (a); case II (b).

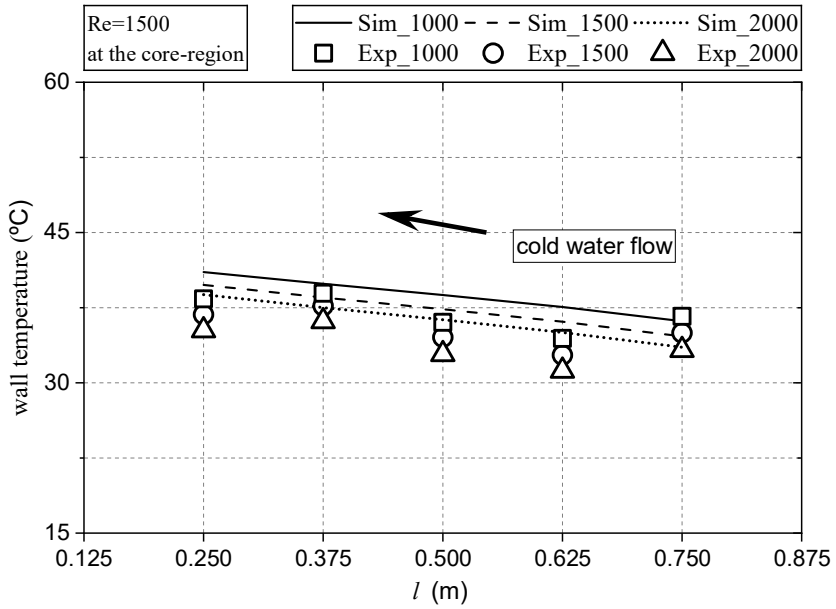

Figure 5.21: Simulated and measured wall temperatures along the ICT test section under laminar flow conditions.

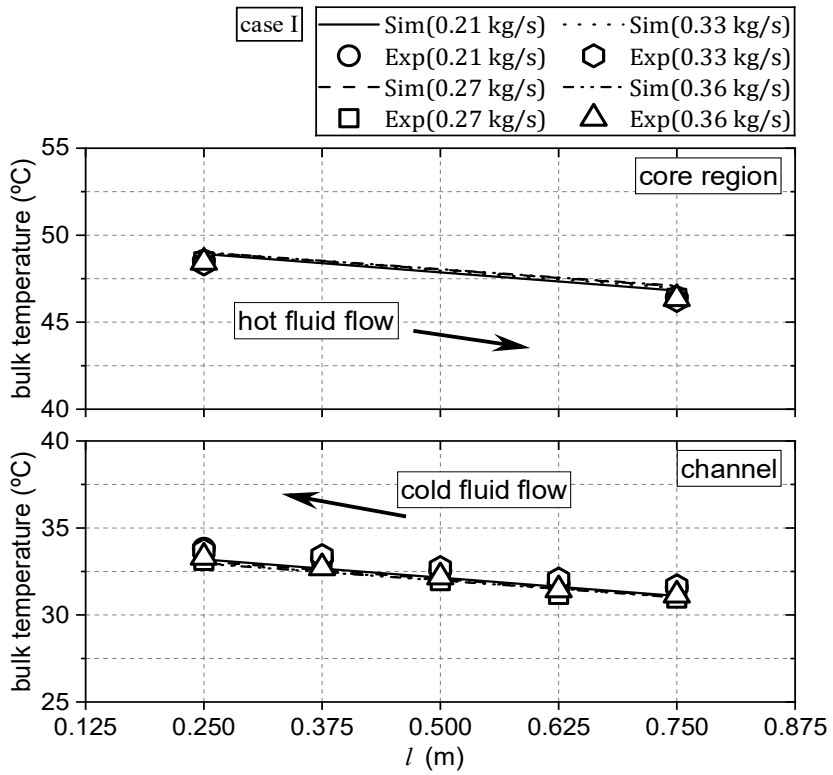

Figure 5.22: Simulated and measured bulk temperatures along the ICT test section under turbulent flow conditions for case I: core region flow (top); channel flow (bottom).

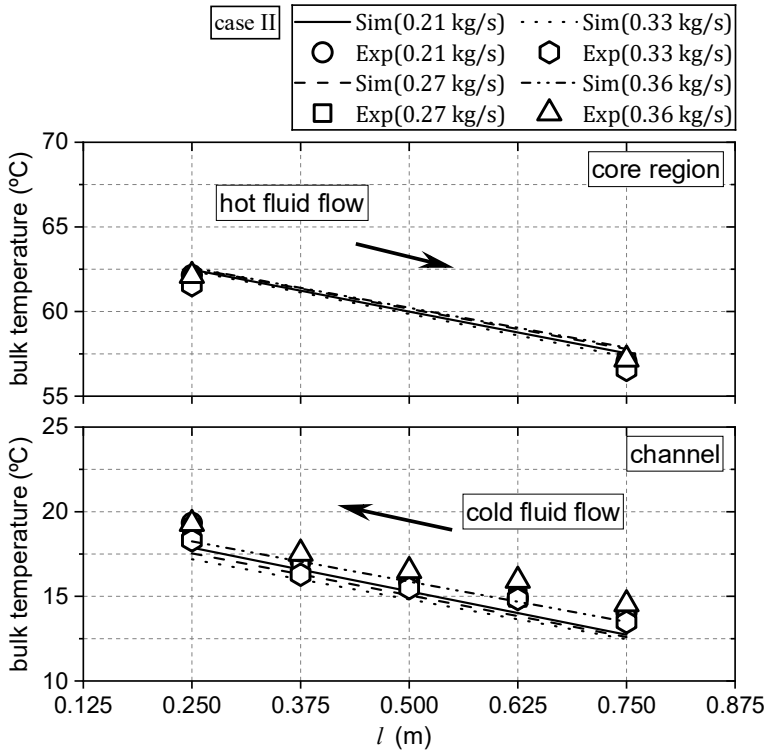

Figure 5.23: Simulated and measured bulk temperatures along the ICT test section under turbulent flow conditions for case II: core region flow (top); channel flow (bottom).

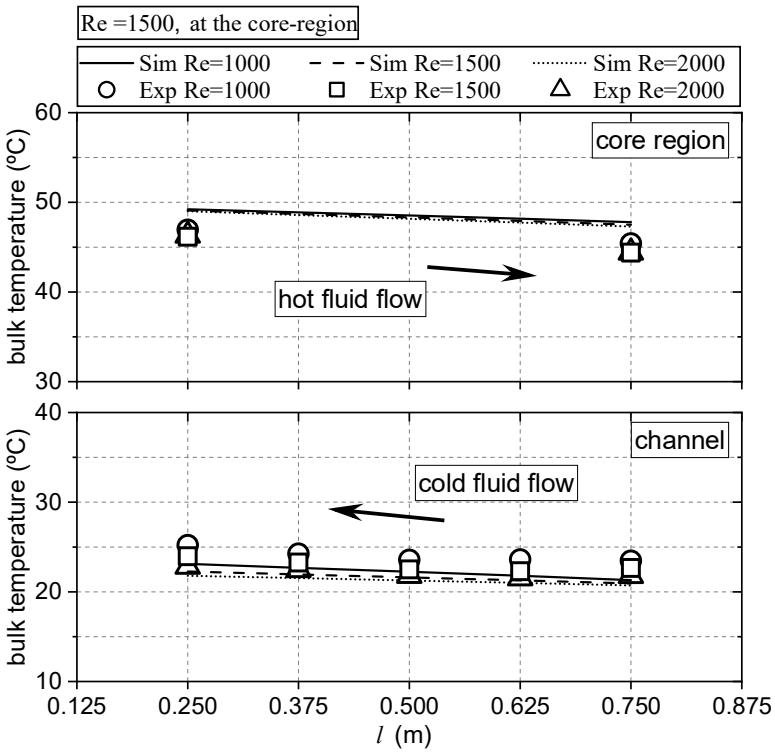

Figure 5.24: Simulated and measured bulk temperatures along the ICT test section under laminar flow conditions: core region flow (top); channel flow (bottom).

5.4 Conclusions

This chapter presented a comprehensive study of fluid dynamics and heat transfer within ICT heat exchangers through detailed CFD simulations and experimental investigations. Conjugate heat transfer (CHT) simulations, performed using ANSYS-Fluent software, enabled precise analysis of velocity, pressure, and temperature distributions within the ICT ducts. These simulations covered both turbulent and laminar flow conditions. The computational domain —comprising structured hexahedral meshes— was simplified using symmetry and domain-splitting approach. The latter subdivided the 1-meter ICT length into three elements, significantly reducing computational demands.

Experiments were conducted using the ICT1 heat exchanger, which was fabricated by the extrusion method. Two experimental setups were built to evaluate its thermal-hydraulic performance. The first setup focused on turbulent flow conditions, using water as the working fluid in both ICT1 ducts. The second setup was designed to study laminar flow conditions. In this experiment, water supplied in the ICT1 channels, and a water-glycerin mixture was used in the core region to increase the viscosity of the hot fluid.

Initial experiments focused on flow maldistribution within the ICT1 channels. The experimental results revealed that the mid-channel demonstrated a slightly higher flow rate compared to the left and right channels. This flow rate difference was observed to be 1% at higher Reynolds numbers, increasing to 4% at Re = 1700, and exceeding 4% for Reynolds numbers below 1000. To ensure accuracy and reliability of measured data, thermal-hydraulic experiments were conducted at Reynolds numbers of 1000 and above, at which flow maldistribution effect is minimal. The flow type in the ICT1 ducts was determined through a subsequent experiment by tracking the pressure drop along the test section. Laminar flow shifts to transitional flow at approximately $Re \approx 1800$ in the core region and $Re \approx 2000$ in the channels, with turbulence onset occurring around $Re \approx 2000$ in the core and $Re \approx 2150$ in the channels.

The experimentally determined pressure drop and temperature values provided a validation basis for the CFD model. The maximum deviation between experimental and simulated values for pressure drop was ±6.5% in the turbulent flow and 11% in the laminar. For heat transfer, the average deviations between measured and simulated temperatures were up to 5% for turbulent flow and 8% for laminar flow.

6 Evaluation of thermal-hydraulic performance of ICTs

This chapter presents a detailed evaluation of the thermal-hydraulic performance of the two ICT heat exchanger designs under different operating conditions. It also includes a numerical comparative evaluation of ICT1 and ICT2 exchangers against a traditional double-pipe heat exchanger (DPHE), which helps to give an appraisal of their performance.

6.1 Thermal performance evaluation of ICTs

In this study, the thermal performance of ICT heat exchangers was evaluated to determine their economic feasibility and to provide insights into the comparative performance metrics of the ICT1 and ICT2. To conduct this evaluation, additional simulations were performed, covering four practical operating conditions.

The simulations were conducted with an inlet temperature of 65°C for the core region (hot side) and 10°C for the channels (cold side) of the ICTs. Water was chosen as the process medium on both the hot and cold sides. Its properties at the specified temperatures are provided in Table 5.2. Mass flowrates were carefully selected to enable a meaningful comparison between the two heat exchangers. Four different cases (C1–C4) were defined based on varying flowrate relationships:

- **Case C1**: Identical mass flowrates were applied in the core region and the six channels of the ICTs.
- **Cases C2, C3, and C4**: The mass flowrates in the channels were increased to two, three, and four times the rate applied in the core region, respectively.

The primary objective of these adjustments was to increase the Reynolds number within the channels to a value approximately equal to that in the core region. A summary of the flowrates for the four cases, under both turbulent and laminar flow conditions, is given in Table 6.1. The cases are labeled with their corresponding numbers (C1–C4), with the indices "*t*" and "*l*" denoting turbulent and laminar flow, respectively.

Table 6.1: Values of the mass flowrates of the investigated cases.

	Mass flow rate [kg s^{-1}]							
flow	Turbulent				laminar			
case	$C1_t$	$C2_t$	$C3_t$	$C4_t$	$C1_l$	$C2_l$	$C3_l$	$C4_l$
core region	0.21	0.33	0.45	0.6	0.009	0.012	0.015	0.021
channels	0.21	0.66	1.35	2.4	0.009	0.024	0.045	0.084

Figure 6.1–Figure 6.4 illustrate the distribution of local heat flux over the internal channel wall and along a segment of 2cm in the middle of the ICTs under both turbulent and laminar flow conditions. According to Figure 6.1 and Figure 6.2, the maximum heat transfer rate under turbulent flow is achieved in case $C4_t$ for both ICT1 and ICT2. A similar trend in heat flux distribution is observed under laminar flow conditions (see Figure 6.3 and Figure 6.4).

According to Figure 6.1–Figure 6.4, the region of poor heat transfer is clearly marked by a blue area near the center of the tube (sharpest turn of the channel surface) and the corner regions, where separation of the flow from the channel surface may occur. On the other hand, the maximum heat flux is seen in the vicinity of the narrow gaps between the channels. This location indicates where the flow re-attaches to the wall, as shown by the thin hydrodynamic layers in the velocity contour presented in Figure 6.5. At the sharpest turn (i.e. vertex of a parabola), the ICT2 exhibits better in terms of heat flux distribution compared to ICT1 (see Figure 6.1–Figure 6.4). This is because the sharpest turn in ICT2 is slightly wider, leading to thinner hydrodynamic boundary layers compared to those observed at the similar location in ICT1 (cf. Figure 6.5).

Based on the channel shape parameters a_l and b_l (illustrated in Figure 4.2), heat transfer efficiency in the channel wall can be enhanced by increasing b_l while keeping a_l

constant. This adjustment widens the sharpest turn of the channel wall near the tube center, reducing flow separation and improving thermal performance. Conversely, increasing a_1 while keeping b_1 constant narrows the sharpest turn, amplifying flow separation and diminishing heat transfer efficiency. These geometric effects and their implications for the ICTs will be examined in detail in the following chapter, which explored design methods and optimization possibilities.

In the corner regions, however, heat transfer in the ICT1 is relatively less weakly affected by proximity of corners compared to ICT2. In ICT2, a significant portion of the corner area does not effectively contribute to heat transfer (cf. Figure 6.1–Figure 6.4).

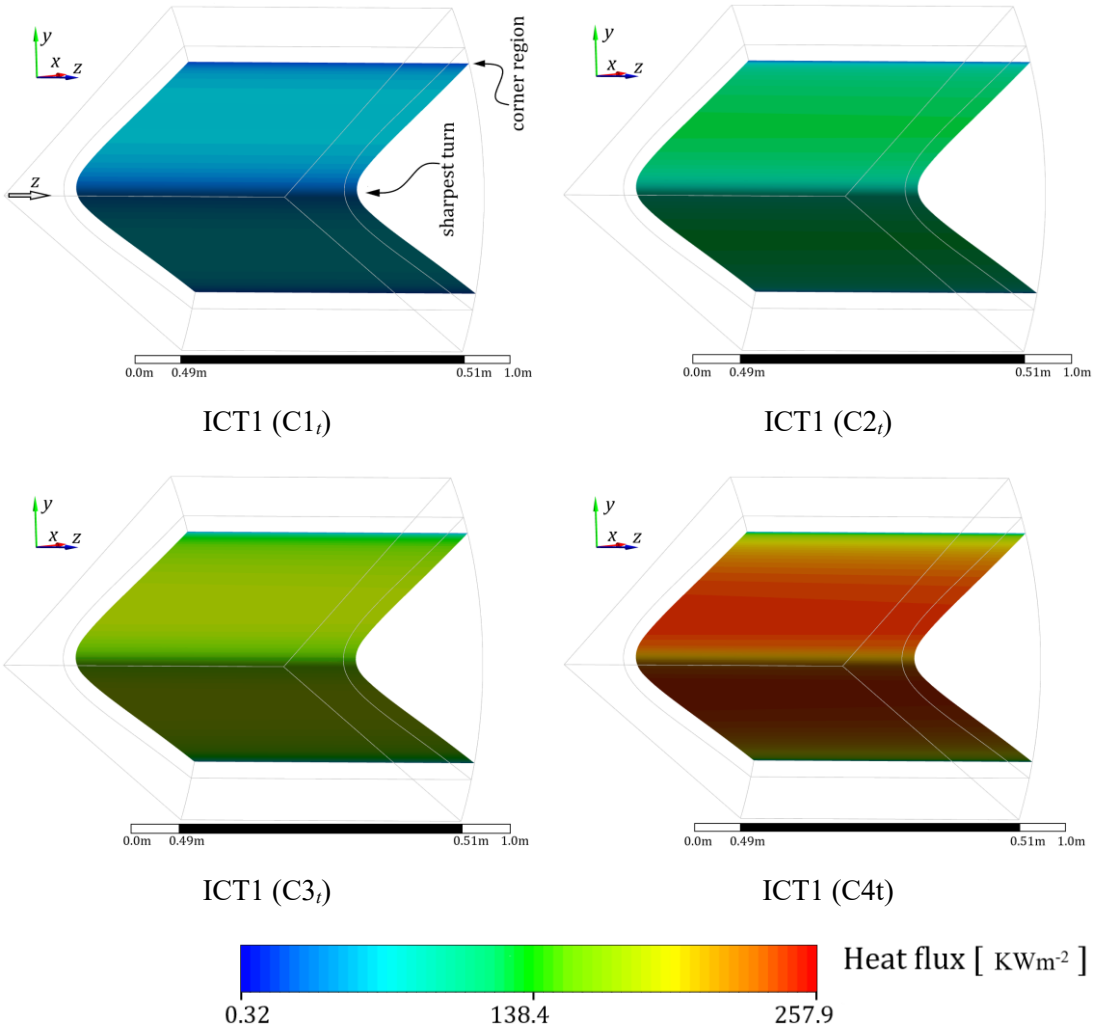

Figure 6.1: Contour plots of local heat flux distributions over the channel wall and a 2 cm mid-segment of ICT1 length under turbulent flow for $C1_t$ to $C4_t$.

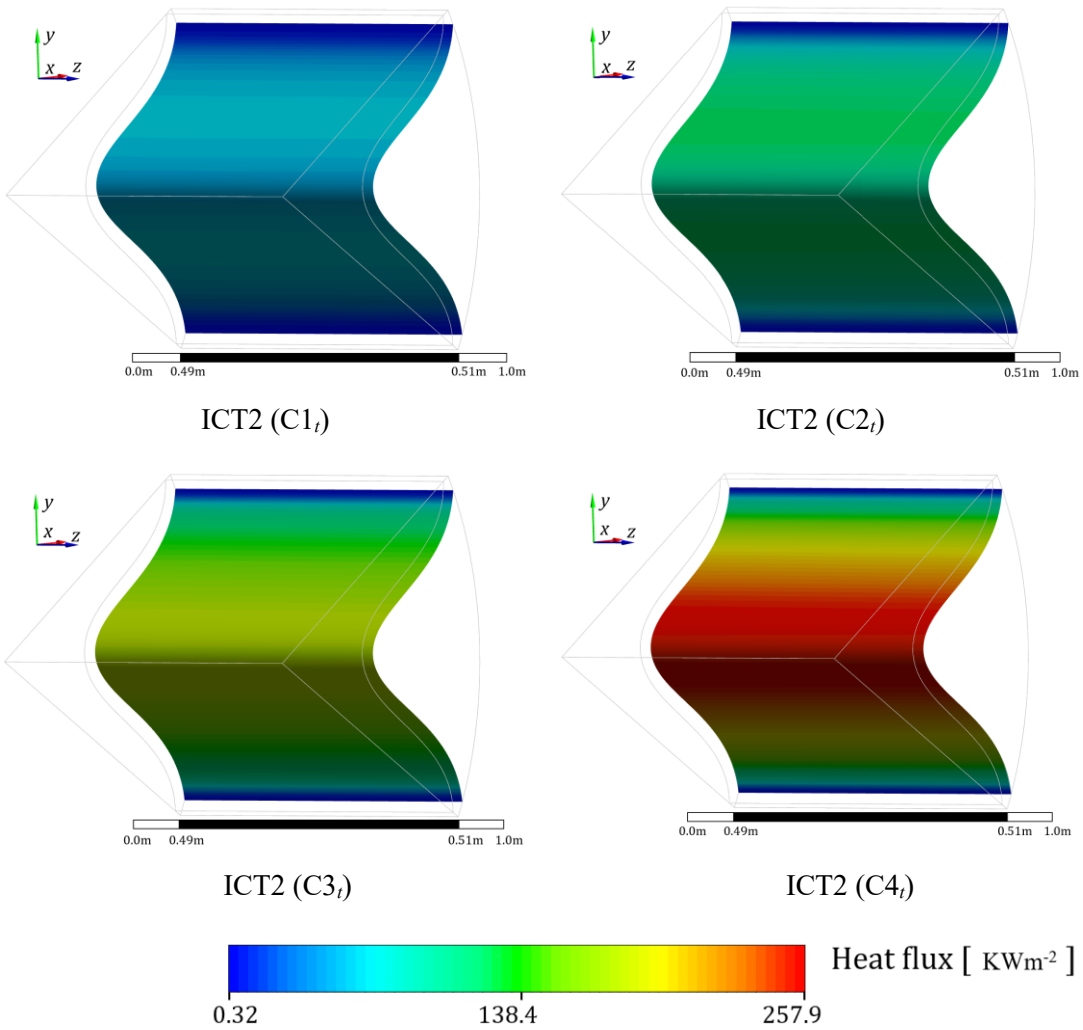

Figure 6.2: Contour plots of local heat flux distributions over the channel wall and a 2 cm mid-segment of ICT2 length under turbulent flow for C1$_t$ to C4$_t$.

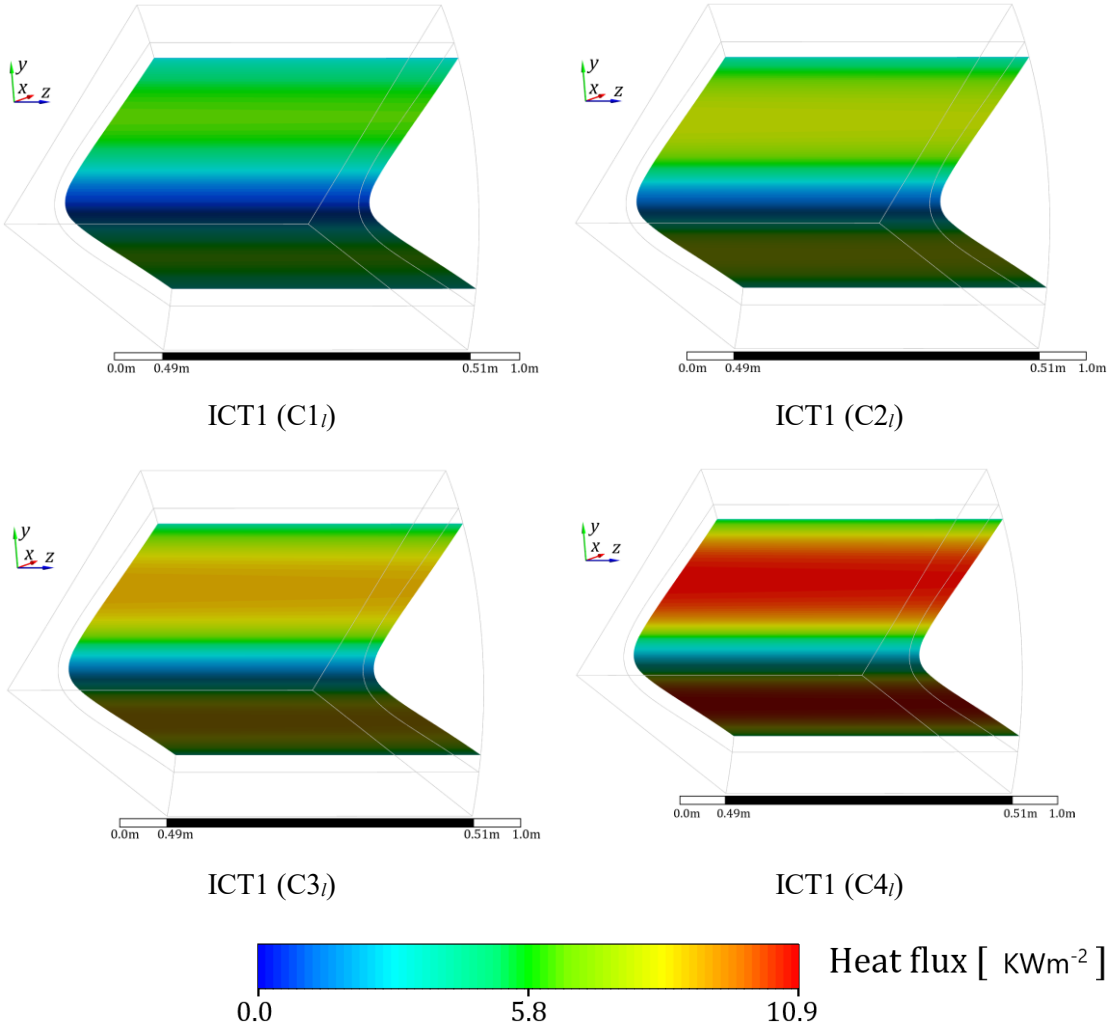

Figure 6.3: Contour plots of local heat flux distributions over the channel wall and a 2 cm mid-segment of ICT1 length under laminar flow for $C1_l$ to $C4_l$.

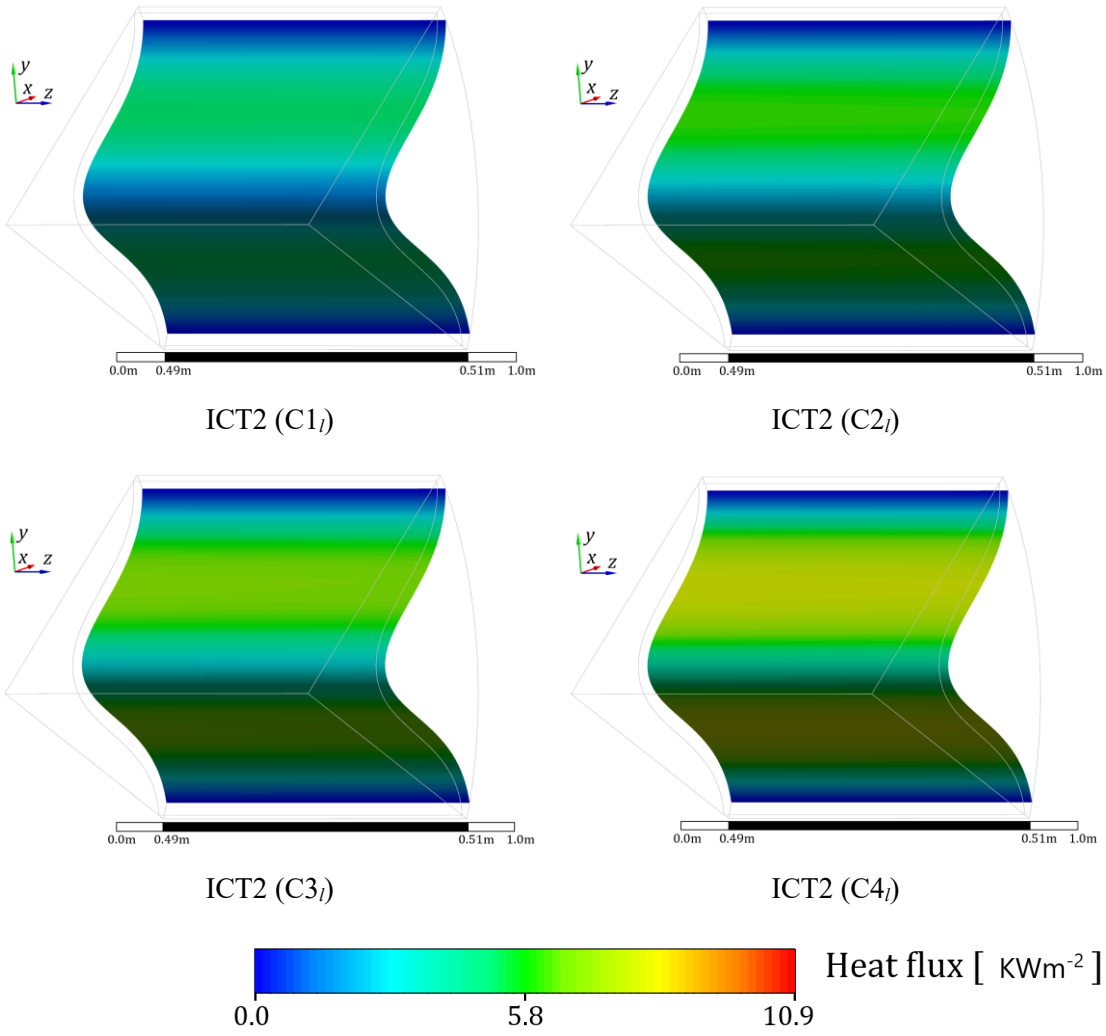

Figure 6.4: Contour plots of local heat flux distributions over the channel wall and a 2 cm mid-segment of ICT2 length under laminar flow for $C1_l$ to $C4_l$.

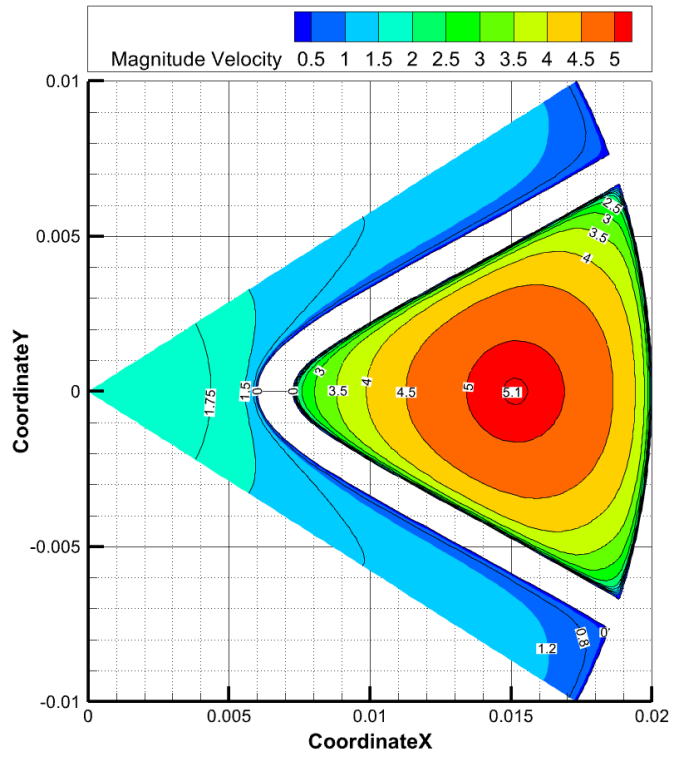

(a)

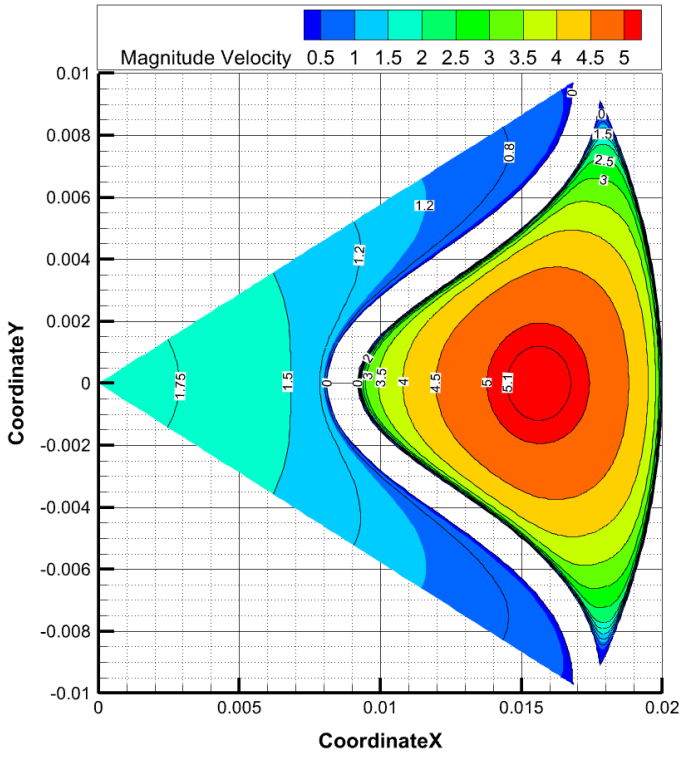

(b)

Figure 6.5: Velocity contour in the ICT channel (case C4$_t$), showing hydrodynamic boundary layers: ICT1 (a); ICT2 (b).

6.2 Performance comparison study

This section presents a comparative study to evaluate the efficiency of ICTs relative to a double pipe heat exchanger (DPHE), providing a practical approach for performance assessment. The DPHE represents a simple and widely used heat exchanger comprising two concentric pipes. As mentioned in Chapter 2, the innovative ICT heat exchangers share similar fundamental flow characteristics with the DPHE, particularly the use of a single outer pipe, making the DPHE an appropriate benchmark for evaluating thermal-hydraulic performance of ICTs.

The performance comparison of different heat exchangers was conducted under the following constraints: identical computational domain length (l), the same tube diameters (d_1 and d_2) (cf. Figure 4.1 and Figure 6.6), and equal wall thickness (δ). The ratios (A_{ch}/A_{cr}), and ($A_{annulus}/A_{inner\ pipe}$) of the cross-sectional areas of the cold and hot fluid ducts were kept at a constant value of 1.16. The mass flowrates in the studied cases (C1 to C4) were applied to the inner pipe and annulus regions of the DPHE in a similar manner as they were applied to the core region and channels of the ICTs. For this comparison, the inner pipe of the DPHE (representing the hot side) was considered analogous to the core region of the ICTs, while the annulus region (representing the cold side) was comparable to the channels. Furthermore, the same inlet temperatures and fluid properties were applied to both the inner pipe (hot side) and the annulus region (cold side) of the DPHE.

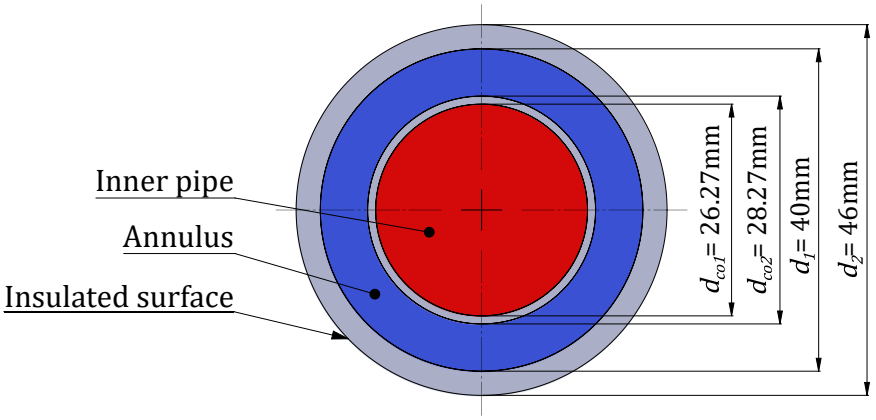

Figure 6.6: Cross-sectional view of the DPHE.

For both ICTs and DPHE, heat transfer rate is determined by:

$$Q = \dot{m} c_p \Delta T \tag{6.1}$$

Here ΔT represents the temperature difference between the outlet and inlet of the middle element ME, and c_p is specific heat of water.

A comparison of the heat transfer rates of the ICTs and DPHE heat exchangers is presented in Figure 6.7. The comparison reveals significantly higher heat transfer rates for the ICTs compared to the DPHE. Specifically, under turbulent flow conditions, ICT1 exhibited an enhancement of up to 52%, while ICT2 shows a 43% increase relative to the DPHE (cf. Figure 6.7a). This enhancement in thermal performance can be attributed to the nearly doubled contact area between the hot and cold fluids in the ICTs. Under laminar flow conditions with low Reynolds numbers, ICT1 demonstrated a heat transfer rate enhancement of up to 60%, whereas ICT2 achieved a 38% improvement compared to DPHE, as shown in Figure 6.7b. Across all cases (C1 to C4), the ICTs consistently outperformed DPHE, with the maximum improvement observed in case C4.

The comparative study also revealed that both ICT1 and ICT2 experienced higher pressure drops than DPHE. This is attributed to the larger internal wall surface area of the ICTs, which is an expected trade-off for intensified heat transfer. Typically, enhanced heat transfer rate is accompanied by increased pressure drop, necessitating higher pump power (Karimi et al., 2020). In the core regions of both the ICT exchangers, the pressure drop was approximately 74% higher than in the inner pipe of the DPHE (cf. Figure 6.8a). Notably, the pressure drop increases with rising Reynolds numbers.

ICT2 exhibited a lower pressure drop in its core region compared to ICT1 due to the removal or reduction of insulated surfaces between the channels. This modification decreases the hydraulic perimeter by 22% in the core region of ICT2, as described in Chapter 4. In the channels of ICTs, the pressure drop increase was smaller, approximately 25% higher than in the annular region of DPHE (see Figure 6.8b).

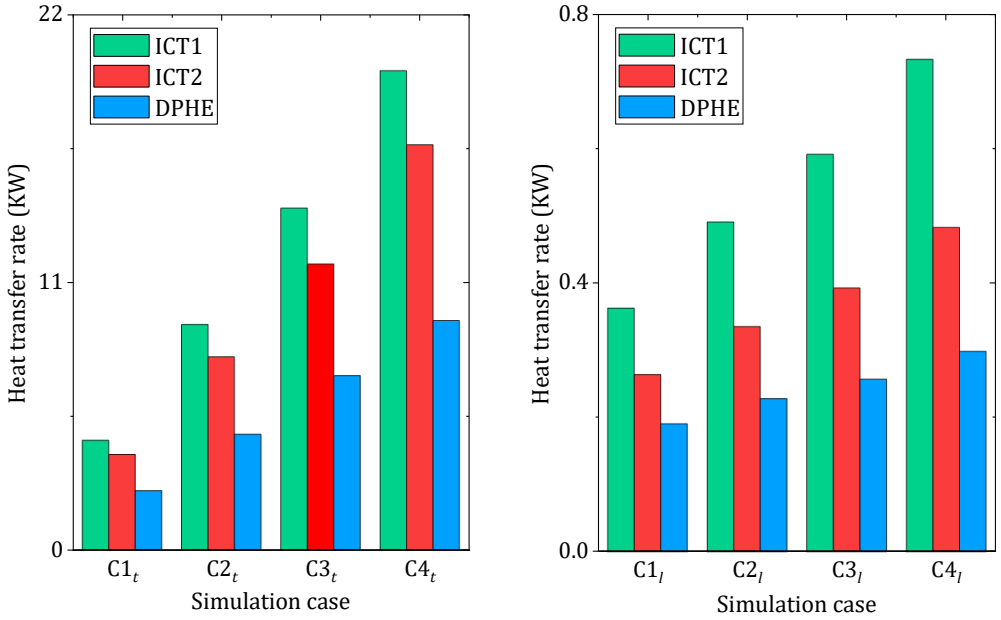

(a) (b)

Figure 6.7: Comparison of heat transfer rate in the ICT1, ICT2, and DPHE: turbulent flow (a); laminar flow (b).

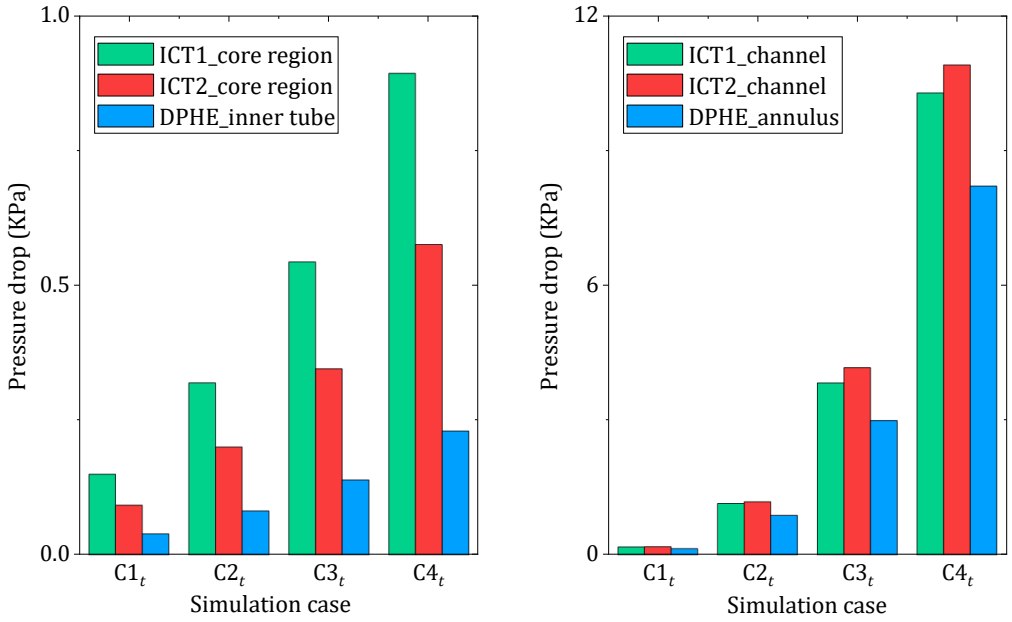

(a) (b)

Figure 6.8: Comparison of pressure drop of ICT1, ICT2, and DPHE under turbulent flow: in the core-regions of the ICTs and inner pipe of DPHE (a); in the channels of the ICTs and annulus of DPHE (b).

Under laminar flow conditions, the pressure drop in the core region of the ICTs is significantly higher compared to that in the inner tube of the DPHE. The pressure drop increases by approximately 87% in ICT1 and 70% in ICT2. In contrast, the pressure drop increase in the channel flow is much smaller, at around 4% compared to the annulus flow in the DPHE. The overall trends can be seen in Figure 6.9a and Figure 6.9b.

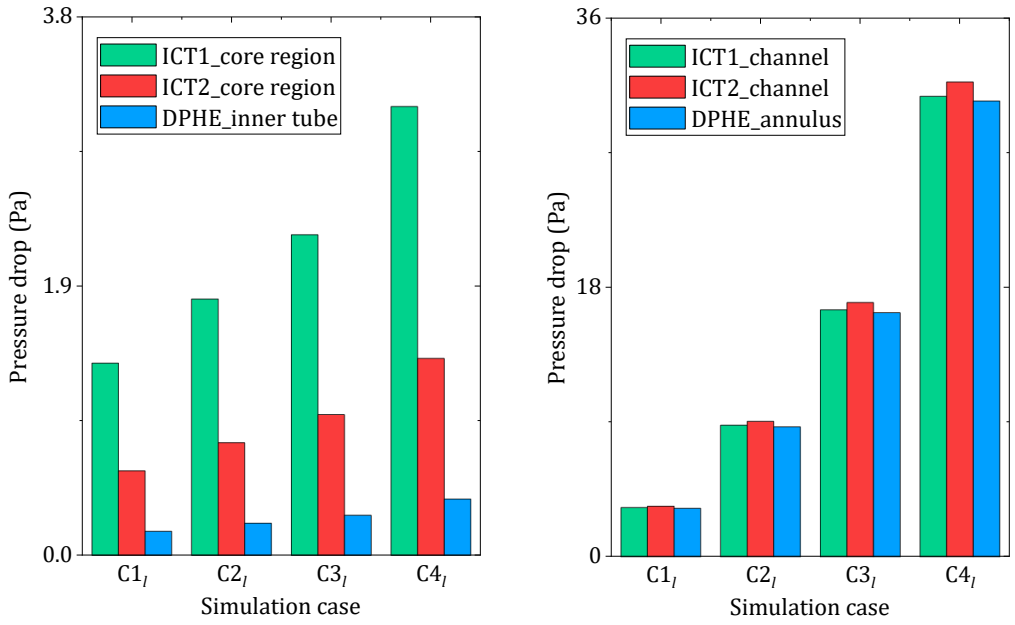

Figure 6.9: Comparison of pressure drop of ICT1, ICT2, and DPHE under laminar flow: in the core-regions of the ICTs and inner pipe of DPHE (a); in the channels of the ICTs and annulus of DPHE (b).

To evaluate the thermal-hydraulic efficiency of ICTs, a more practical approach was adopted in this study, based on the ratio of the total heat exchanged between the core region and channels to the overall pressure drop in these ducts (effectively capturing the total energy expended on pumping power). The efficiency can be expressed by:

$$\dot{\varepsilon} = \frac{Q}{\dot{W}} = \frac{Q}{\dot{V}\,\Delta p} \tag{6.2}$$

Here, Q is heat transfer rate, calculated using Eq. (6.1), and $\dot{V}$ is volumetric flowrate.

For a more convenient comparison with the DPHE, a performance evaluation criterion (PEC) can be employed. The PEC relates the thermal-hydraulic efficiency ($\dot{\varepsilon}$) of the ICTs to the efficiency of DPHE, providing a reasonable indicator for comparing different exchanger types. It is essential that the PEC includes both heat transfer performance and pressure drop, i.e. the crucial quantities for practical applications (Fan et al., 2009; Lu et al., 2011; Wang et al., 2019). The PEC index can be expressed as follows:

$$\mathrm{PEC} = \frac{(\dot{\varepsilon})_{ICT}}{(\dot{\varepsilon})_{DPHE}} = \frac{Q_{ICT}/Q_{DPHE}}{(\dot{W})_{ICT}/(\dot{W})_{DPHE}} \tag{6.3}$$

$$(\dot{W})_{ICT} = (\dot{V}\Delta p)_{core\ region} + (\dot{V}\Delta p)_{channel} \tag{6.4}$$

$$(\dot{W})_{DPHE} = (\dot{V}\Delta p)_{inner\ pipe} + (\dot{V}\Delta p)_{annulus} \tag{6.5}$$

Q_{ICT}, and Q_{DPHE} represent the average heat transfer rates in the ICTs and DPHE, respectively. $\dot{W}_{ICT}$ is the overall pumping power in the core-region and channels of the ICTs, while $\dot{W}_{DPHE}$ denotes the overall pumping power in the inner pipe and annulus of DPHE.

Figure 6.10 illustrates the PEC index of ICTs, using the DPHE as the reference exchanger, across the four simulation cases under both turbulent and laminar flow conditions. The PEC values exceed unity, with the highest value observed in case C4. Specifically, for ICT1, the PEC values reach approximately 1.64 in turbulent flow and 2.3 in laminar flow (see Figure 6.10). For ICT2, the maximum PEC values in case C4 are approximately 1.32 in turbulent flow and 1.54 in laminar flow.

When the PEC exceeds one, there is a comparative advantage in terms of heat transfer efficiency at the same pumping power cost. PEC values greater than unity indicate that the increase in heat transfer rate outweighs the pressure drop penalty for the ICTs compared to DPHE. Conversely, when the PEC index falls below one, the use of the ICTs may

become unfavorable due to the higher pumping power cost (Al-Sammarraie & Vafai, 2019).

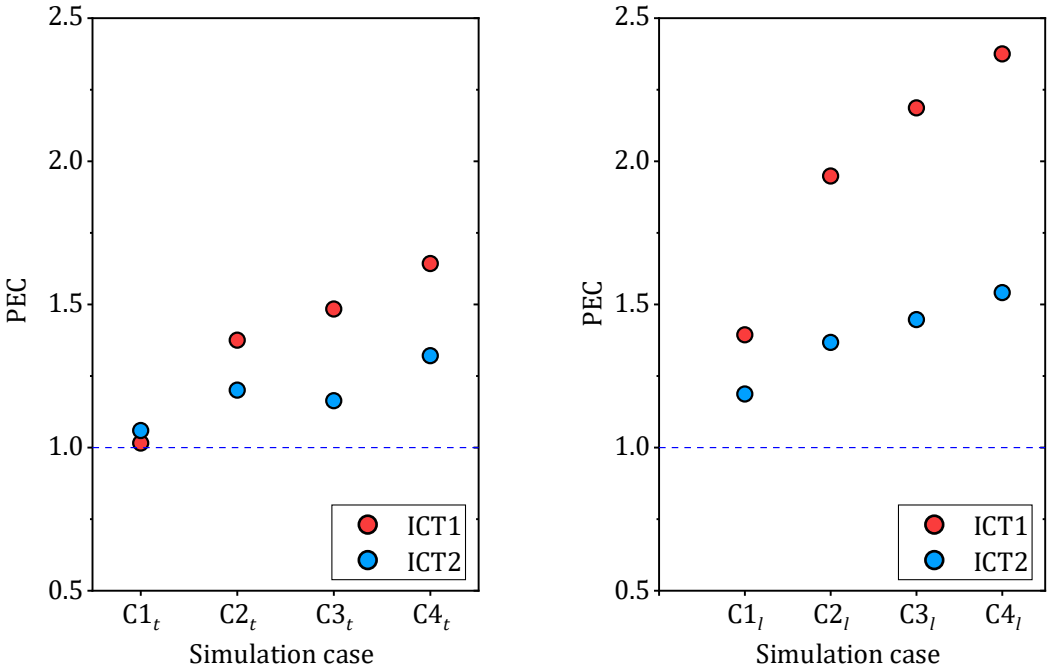

Figure 6.10: Performance evaluation index (PEC) of the ICTs with DPHE as reference heat exchanger: turbulent flow (a); laminar flow (b).

The higher PEC values can be explained by a significant increase in the total heat transfer rate —up to 60%—observed in the ICTs (see Figure 6.7). This is accompanied by only a minor pressure drop in the channels, as illustrated in Figure 6.8 and Figure 6.9. In cases (C2-C4) under both flow conditions, as shown in Figure 6.10, ICT1 outperforms ICT2, achieving PEC values of 1.9–2.3. This superior performance is primarily due to the higher heat transfer rate in ICT1, with a nearly equivalent overall pressure drop in both ICTs. Furthermore, the channel configurations of ICT1 demonstrated more effective heat flux distribution near the corner regions compared to ICT2, contributing to its enhanced overall thermal performance.

6.3 Conclusions

This chapter presented a CFD-based comparison between the ICT1 and ICT2 heat exchanger designs under varying mass flowrate conditions. In case C1, equal mass flowrates were applied to both the core region and the channels, while in subsequent cases (C2 to C4), the channel mass flowrate was increased to 2, 3, and 4 times that of the core, respectively. The results showed that increasing channel mass flowrates enhanced heat transfer, with case C4 under turbulent flow delivering the highest performance. A similar trend was found under laminar flow conditions. The comparison revealed design-specific trade-offs, as each configuration demonstrated strengths in different regions of the flow path.

Building on this, a comparative numerical analysis with conventional double pipe heat exchangers (DPHE) further highlighted the thermal advantages of ICT designs. The superior performance of ICTs was confirmed by a Performance Evaluation Criterion (PEC) value greater than one, reflecting improved thermal-hydraulic efficiency at similar pumping power requirements. These results reinforce the potential of ICT heat exchangers as high-efficiency alternatives for advanced thermal management applications.

7 Design methods for ICTs

Existing correlations for predicting pressure drop and heat transfer in turbulent flow conditions when applied to non-circular conduits often have just limited design flexibility. They are primarily developed for specific cross-sectional geometries, which may not directly be applicable to ICT duct geometries. This justifies the need for more reliable and effective methods for ICT heat exchangers.

As an initial approach, and in the absence of experimental validation, published correlations developed for circular geometries were applied to the ICT ducts in Ref. Al-Lami et al. (2023). These correlations served as a means to qualitatively evaluate the feasibility of the CFD model. An experimental validation was subsequently conducted in a later study (Al-Lami & Kenig, 2023); it is detailed in Section 5.3.6. Existing correlations developed for circular tubes were adapted to non-circular ducts (e.g., ICT ducts) with specific modifications to the length scale parameters. In this case, the diameter in friction factor correlations (provided in Appendix A, Table A1) was replaced with the hydraulic diameter of the ICT ducts. The hydraulic diameter (D_h) can be mathematically expressed as four times the cross-sectional area of the duct divided by its wetted perimeter, according to Eq. (4.7).

Further, in the calculations of the Nusselt number, a specific adjustment was applied to the existing correlations (given in Appendix A, Table A2). As explained in Section 4.2, the Nusselt number includes the equivalent diameter (D_e), which is determined using Eq. (4.6). This diameter can differ significantly from the hydraulic (D_h) diameter due to the particular geometry of the ICTs with insulated walls. As discussed in Section 5.3.3, due to this insulation, no thermal boundary layers are encountered near these insulated walls,

whereas hydrodynamic boundary layers are present everywhere in the vicinity of the duct walls. For an accurate evaluation of heat transfer in ICT ducts, the equivalent diameter must be applied (Duarte & Corradini, 2018). To ensure proper application of these correlations (Appendix A, Table A2) to ICT ducts, a recasting was performed using the Dirker methodology (Dirker & Josua, 2002), as detailed in Ref. (Al-Lami et al., 2023). This recasting included a conversion from the hydraulic diameter to the equivalent diameter as follows:

$$\mathrm{Nu}_e = \mathrm{Nu}_h \cdot \frac{P_h}{P_e} \tag{7.1}$$

Here Nu_h and Nu_e are Nusselt numbers based on hydraulic and equivalent diameter, respectively. The correlations explored in (Al-Lami et al., 2023), presented in Appendix A, were proposed by Drew and McAdams (1932), Nikuradse (1950), and Gnielinski (1976) for the friction factor and by Petukhov, (1970), Gnielinski, (1976), and Dittus and Boelter, (1985) for the Nusselt number.

The need for new correlations for ICT heat exchangers that duly account for their specific, non-circular geometry and cover realistic flow and boundary conditions remains. One of the essential reasons is the presence of insulated outer surface in ICT, which makes the direct application of existing published correlations to the ICT ducts unfeasible. It is why in Ref. Al-Lami et al. (2023), a special adjustment was made for the Nusselt number correlations taken from Refs. Petukhov (1970), Gnielinski (1976), and Dittus and Boelter (1985). The adjustment was deemed necessary due to a difference between the length scale used in these correlations and the appropriate length scale for calculating the Nusselt number for the ICT ducts. The adjusted correlations were applied in Ref. (Al-Lami et al., 2023) to the ducts of ICT1 and ICT2, and their performance was reasonably good. However, this cannot be guaranteed for further ICT modifications toward their optimization, for instance when the duct shape or the number of channels change. To cover a wider range of geometrical parameters and avoid significant inaccuracy, appropriate novel correlations must be developed.

In this chapter, the derivation of such correlations for the thermohydraulic design of ICT1 under turbulent forced convection and countercurrent flow conditions is presented. The correlations were developed based on the results obtained by the CFD simulations for

wide range of geometrical parameters and the Reynolds numbers range ($2500 \leq Re_h \leq 40000$). Preliminary sensitivity studies were conducted to identify the geometrical parameters of ICT1 ducts that have a significant impact on both the friction factor and the Nusselt number. This helped to integrate the most influential parameters into the developed correlations thus improving their predictivity.

7.1 Design equations for friction factor

The pressure drop in the middle part of the ICT1 (test section) is primarily caused by fluid-wall friction. Its value is quantified as the differential pressure between the inlet and outlet of the middle part of ICT1, as shown in Figure 7.1.

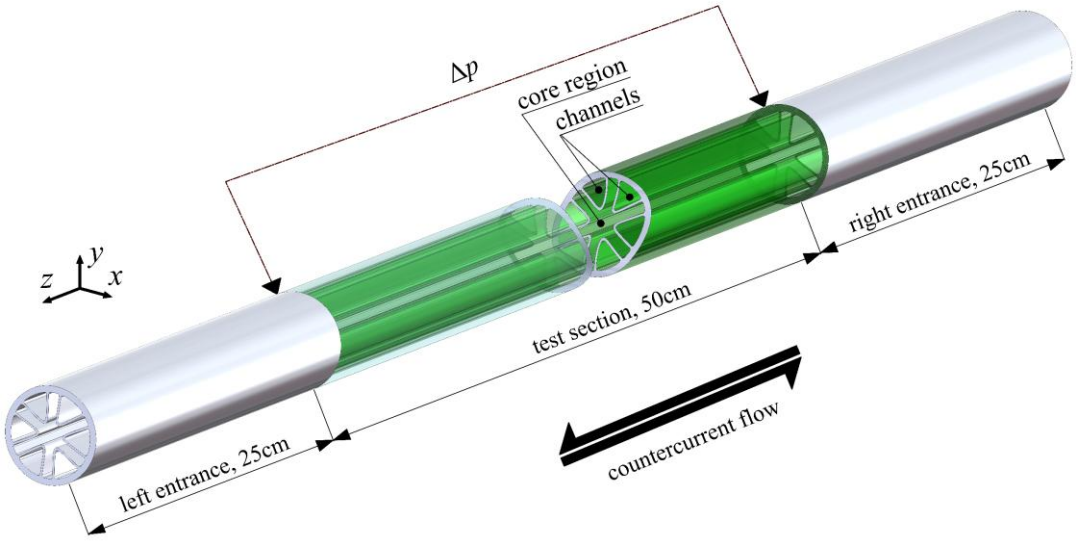

Figure 7.1: A schematic of an ICT heat exchanger. The green-colored length illustrates the mid-element (test section).

In this study, the frictional loss is defined by the Fanning friction factor—a dimensionless parameter representing flow resistance (see Eq. (5.3)). It is equal to the ratio of wall shear stress to dynamic pressure ($0.5\ \rho v^2$), where ρ is the fluid density and v is the fluid velocity. Gravitational effects are negligible due to the assumption of the horizontal orientation of ICT1 heat exchanger. In addition, the left and right entrance elements are excluded from the friction factor calculation because a more stable flow within the middle part is expected (cf. section 5.2.2).

As detailed in Section 5.3.6, the CFD model demonstrates a good agreement with experimental measurements across the entire studied Reynolds number range ($2{,}500 \leq Re_h \leq 18{,}000$). The maximum deviation for friction factors was below 6.5%, for both core region and channel flow of ICT1, as demonstrated in Figure 5.18.

7.1.1 Effect of duct geometry on friction factor

The power law function ($f = mRe^j$, where m and j are constants) is widely used to estimate friction factors in circular ducts (Branco et al., 2001). It is a straightforward approach to incorporate the substantial influence of the Reynolds number. However, in non-circular ducts, the friction factor can also be influenced by the duct geometry (Wang et al., 2008; Muzychka & Yovanovich, 2009, 2012). In a number of studies, friction factors in non-circular ducts were correlated by employing geometrical parameters. Duan & Yovanovich (2009), and Duan (2012) developed correlations to predict pressure drop in arbitrary-shape ducts based on the aspect ratio, defined as the minor axis length to the major axis length of the duct. It was found that duct cross-sections can have a significant influence on the friction factor. Correlations to predict pressure loss in turbulent flow within the inner channel of a pillow-plate heat exchanger were established by Piper et al. (2017), including geometrical parameters of the channel.

It is, therefore, necessary to establish correlations for ICT ducts, with due considerations of geometrical parameters (e.g., a_1, b_1, b_2, c_2), so that ICT can be designed and optimized accordingly. The geometrical parameters a_1, b_1, b_2, c_2, s_1, P_h and e shown in Figure 7.2 were identified in this study as having an impact on friction factor in the ICT1 ducts. The influence of the characteristic geometrical parameters on the friction factor was analyzed using the CFD simulations. Dimensionless parameter combinations can be built in relation to the inner radius of the tube as follows:

$$\vartheta = (a_1 + s_1)/r \tag{7.2}$$

$$\eta = 2b_1/r \tag{7.3}$$

$$\gamma = 2b_2/r \tag{7.4}$$

$$\psi = c_2/r \tag{7.5}$$

$$\varphi = e/r \tag{7.6}$$

$$\beta_h = P_h/r \tag{7.7}$$

Here r is a half of the inner diameter (d_1) (cf. Figure 7.2).

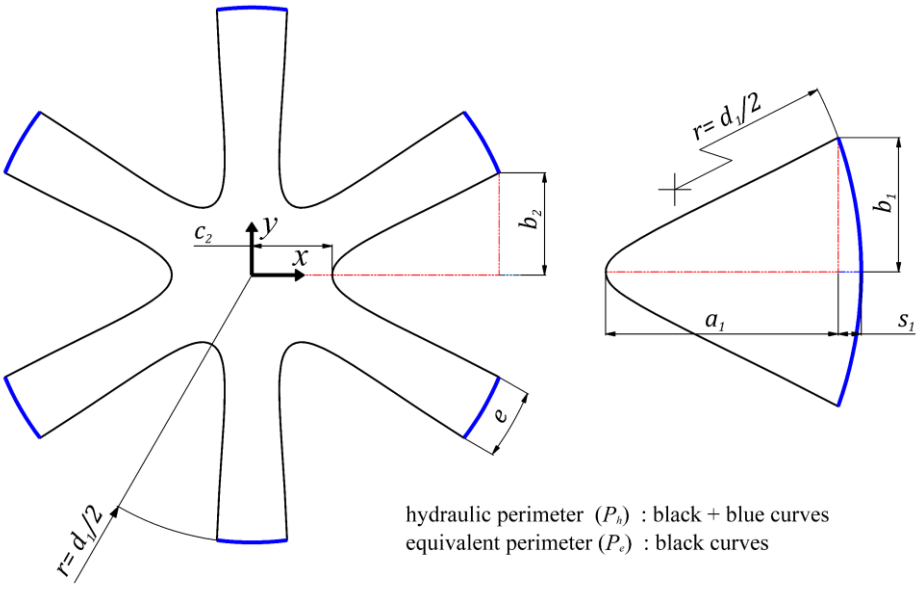

Figure 7.2: Cross-section of the ICT1 ducts with characteristic geometries: core region (left); channel (right).

The influence of characteristic geometry parameters on the Fanning friction factor in the ICT1 ducts is demonstrated in Figure 7.3 and Figure 7.4. Figure 7.3 reveals a substantial impact of the parameters ψ and γ on the friction factor in the core region at Re_h= 12000. The graphs illustrate the effects of varying ψ while keeping γ constant at

0.764 (Figure 7.3a), and varying γ while maintaining ψ at 0.3 (Figure 7.3b), both under conditions of Re_h= 12000.

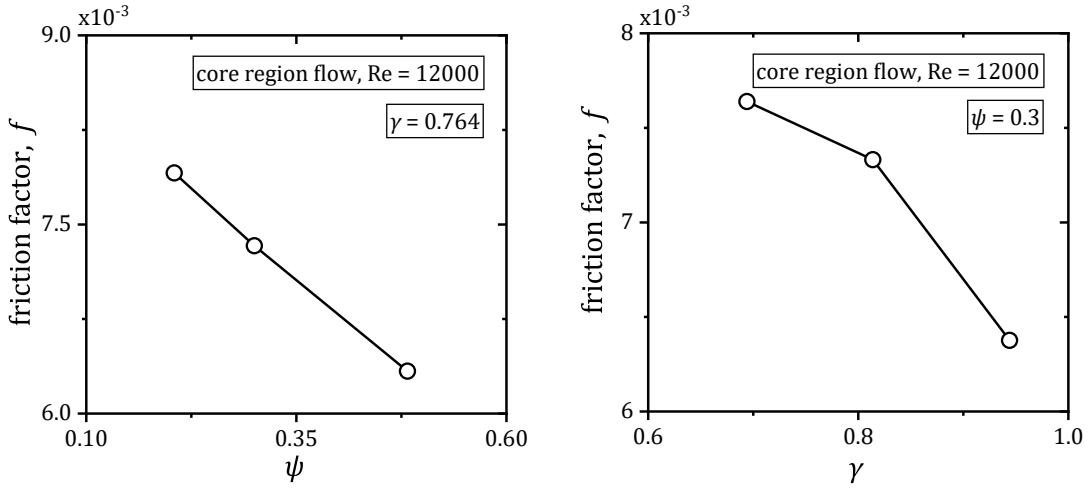

Figure 7.3: Influence of the dimensionless geometrical parameters: ψ (a); and γ (b) on the Fanning friction factor in the core region of ICT1.

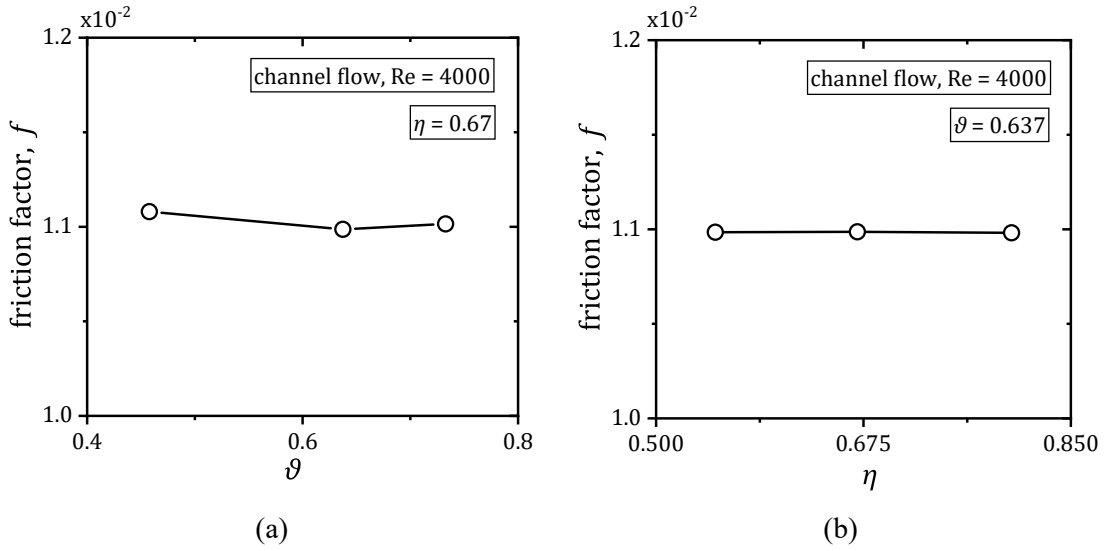

Figure 7.4: Influence of the dimensionless geometrical parameters: ϑ (a); and η (b) on the Fanning friction factor in the channel region of ICT1.

In contrast, the geometrical parameters have nearly no influence in the channel region, as can be seen in Figure 7.4. This figure presents results for the varied ϑ at a constant values of $\eta = 0.67$ (Figure 7.4a) and for the varied η at $\vartheta = 0.637$ (Figure 7.4b), both at

Re_h= 4000. The parameters φ and β_h exhibited a comparable influence on the friction factor, demonstrating trends similar to those observed for the parameters ψ and γ, as illustrated in Figure 7.3.

7.1.2 New friction factor correlations

The following correlations are proposed for the friction factor in the ICT1 ducts under turbulent flow conditions.

for the core region:

$$f_{cr} = n_1 \mathrm{Re}_h^{n_2} (\gamma)^{n_3-\varphi} (\beta_h)^{n_4} \tag{7.8}$$

for the channels:

$$f_{ch} = n_5 \mathrm{Re}_h^{n_6} (\beta_h)^{n_7} \tag{7.9}$$

Here $n_1$to n_7 are the coefficients of the correlations.

The coefficients n_1 to n_7 of the correlations Eqs. (7.8) and (7.9) are determined by nonlinear regression analysis. This well-known numerical method uses input values (Reynolds numbers and geometrical parameters of ICT1 ducts) and fitting correlations, Eqs. (7.8), (7.9); their results are compared with the values obtained by CFD simulations. Minimization of the residual sum of squares (RSS) yields the values n_1 to n_7. The obtained coefficients of Eq. (7.8), (7.9) are presented in Table 7.1. The CFD data used in this analysis is based on the pressure drop values extracted from the simulations.

According to the trend shown above in Figure 7.4, the dimensionless combination η is omitted in Eq. (7.9). The ratio β_h of the hydraulic perimeter to the radius is included in both correlations to obtain accurate predictions for various geometries. This inclusion helps to capture the impact of the complex wall curvature more precisely, as this cannot be done properly using the parameters a, b, c only. Moreover, Eq. (7.8), contains an additional exponent φ, which represents the ratio of the peripheral distance between every two channels in the core region to the inner radius, $\varphi = e/r$. The variation ranges of the geometrical parameters in this study are summarized in Table 7.1.

The developed correlations, Eqs. (7.8), (7.9), are compared with the CFD results in Figure 7.5. With the proposed equations, the Fanning friction factor in ICT1 ducts can be reproduced with good accuracy, with the maximum deviation being 7.5% for the core region and 7% for the channel flow. Nearly 95% of the data falls within a maximum deviation of less than 5%. The validity range for the Reynolds number is $6000 \leq \mathrm{Re}_h \leq 40000$ for core region flow and $2500 \leq \mathrm{Re}_h \leq 15000$ for channel flow.

Table 7.1: Summary of coefficients of Eqs. (7.8), (7.9) and geometrical parameter ranges for the friction factor.

	Core region flow			**Channel flow**	
	$f = n_1 \,\mathrm{Re}_h^{n_2} (\gamma)^{n_3 - \varphi} (\beta_h)^{n_4}$			$f = n_5 \,\mathrm{Re}_h^{n_6} (\beta_h)^{n_7}$	
	$0.5 \leq \gamma \leq 1\,,\ 8 \leq \beta_h \leq 13,\ \ 0 \leq \varphi \leq 0.4$			$0.5 \leq \eta \leq 1,\ \ 1.7 \leq \beta_h \leq 2.6$	
	$0.2 \leq \psi \leq 0.32$	$0.34 \leq \psi \leq 0.5$		$0.35 \leq \vartheta \leq 0.56$	$0.58 \leq \vartheta \leq 0.70$
n_1	0.0414	0.1650	n_5	0.25350	0.240
n_2	-0.3175	-0.3040	n_6	-0.34360	-0.360
n_3	0.1400	0.2250	n_7	-0.45800	-0.128
n_4	0.5190	-0.1570			

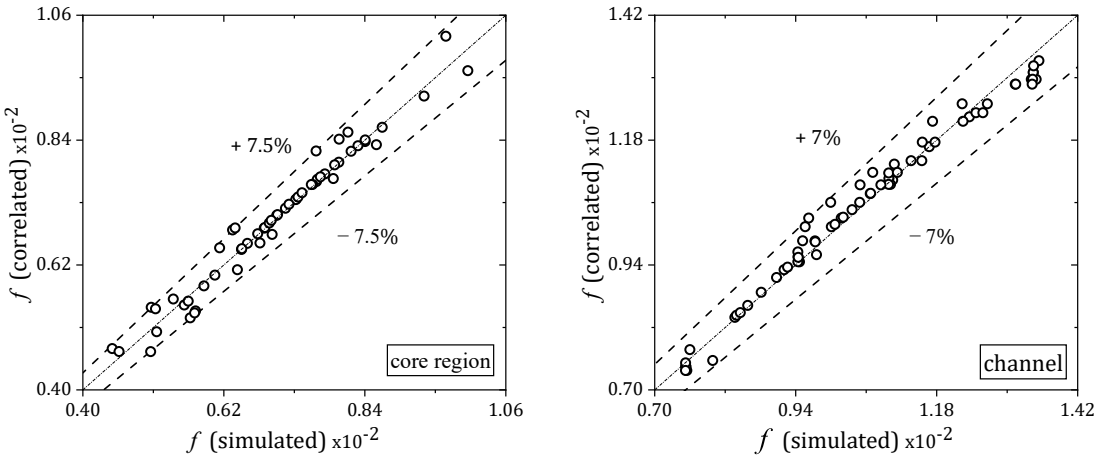

(a) (b)

Figure 7.5: Comparison between friction factors obtained by simulations and those calculated by Eq. (7.8) (a) and Eq. (7.9) (b) with coefficients from Table 7.1.

7.2 Design equations for Nusselt number

The Nusselt number correlations are commonly represented in a simple form of Dittus-Boelter (Dittus & Boelter, 1985) which is a power-law equation. This form is used for turbulent flows in smooth pipes and describes the dependence of the Nusselt number on the Reynolds and Prandtl numbers. However, the power-law form may not sufficiently capture the behavior of the Nusselt number for complex geometries found in non-circular ducts (Sahin, 2007; Emrich, 2016). The complex shape of non-circular ducts has a direct impact on the velocity and temperature distributions. This results in a particular fluid flow and heat transfer behavior, which differs from what can be typically observed in circular ducts (Wang et al., 2016). Thus, a straightforward application of the Dittus-Boelter (Dittus & Boelter, 1985) correlation to non-circular ducts is hardly possible; rather, it has to be modified and adapted by incorporating relevant geometric parameters of the specific non-circular duct.

The Nusselt number obtained from CFD simulations can be determined using Eq. (5.4), based on average heat transfer coefficient (h_{avg}). The latter was validated by comparing it with the heat transfer coefficient calculated from the experimentally temperatures measured under turbulent flow conditions during each steady-state test run (cf. Section 5.3.6.2).

The average heat transfer coefficient (h_{avg}) is defined as follows:

$$h_{avg} = \frac{Q}{A \cdot \left(T_{avg,w} - T_{avg,b}\right)} \tag{7.10}$$

where $T_{avg,w}$ is the average inner wall temperature, $T_{avg,b}$ is the average bulk temperature of the test section, A is heat transfer area, and Q is the heat transfer rate obtained from:

$$Q = \dot{m} c_p (T_{out} - T_{in}) \tag{7.11}$$

Here $\dot{m}$ is mass flow rate, $(T_{out} - T_{in})$ is the temperature difference between the outlet and inlet of the test section, and c_p is specific heat of water.

The heat transfer coefficients determined experimentally were compared with the values obtained from the CFD simulations. As can be seen in Figure 7.6, they are in a good agreement over the entire range of studied Reynolds numbers ($2500 \leq Re \leq 18000$) of both cases, with a maximum deviation of 13%.

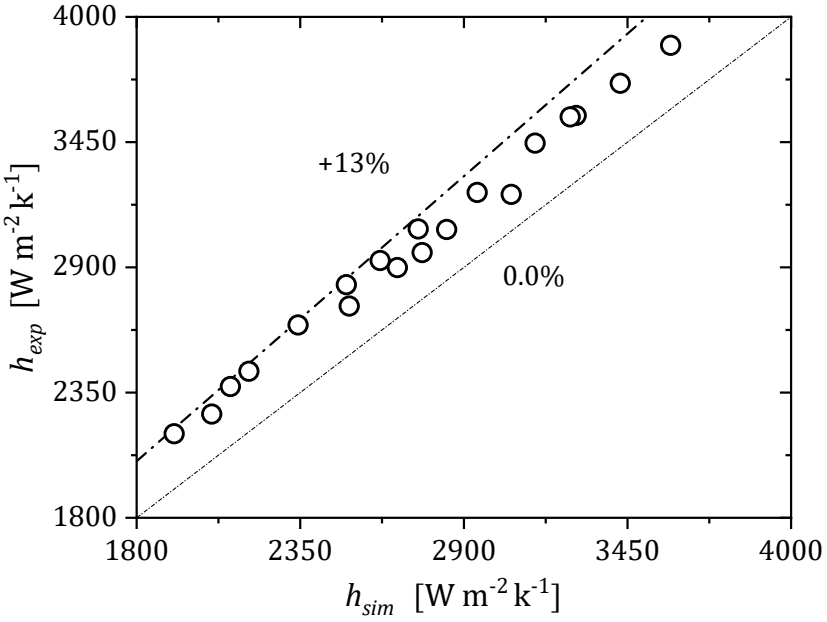

Figure 7.6: Comparison of numerically and experimentally evaluated heat transfer coefficients.

7.2.1 Effect of duct geometry on Nusselt number

In this study, numerical analysis was performed to examine the impact of geometrical parameters shown in Figure 7.2 on the Nusselt number. This analysis was carried out in a similar way as for the friction factor (cf. Section 7.1), and the geometrical parameters were subsequently incorporated into the power-law form of Dittus and Boelter (1985).

Figure 7.7 and Figure 7.8 demonstrate the relationship between the Nusselt number and various combinations of ICT1 geometrical parameters. The qualitative trends shown on Figure 7.7 for the core region flow are similar to those visible on Figure 7.3. This similarity does not hold for the dependencies of the Nusselt number on geometrical parameters ϑ and η at $Re_h = 4000$ (cf. Figure 7.8). It is clearly seen that the geometrical parameters of ICT1 ducts have a substantial impact on the Nusselt number.

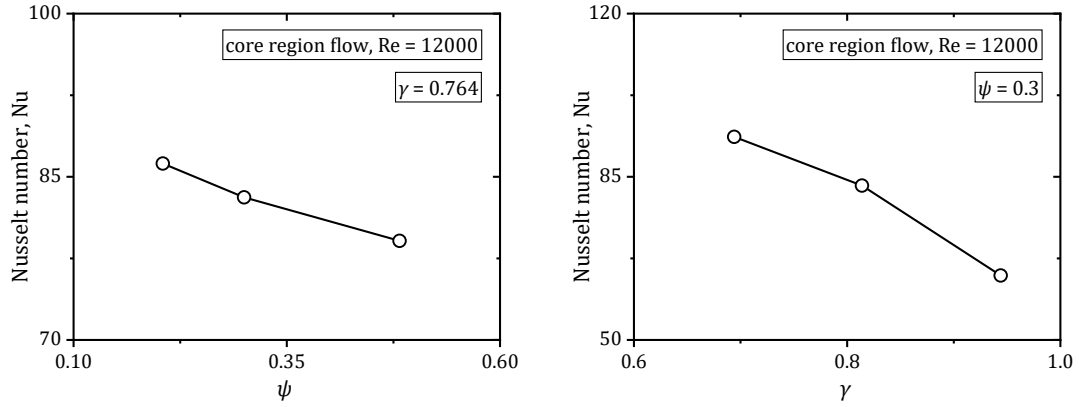

(a) (b)

Figure 7.7: Influence of the dimensionless geometrical parameters:ψ (a); and γ (b) on the Nusselt number in the core region of ICT1.

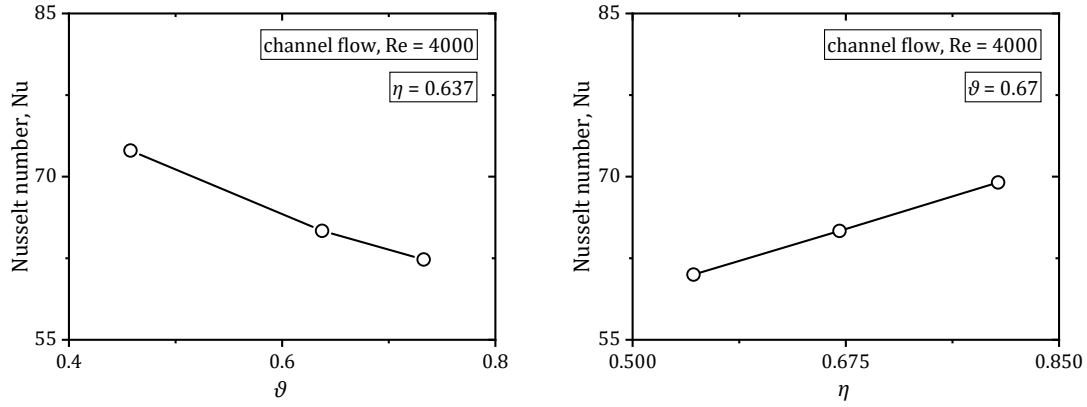

(a) (b)

Figure 7.8: Influence of the dimensionless geometrical parameters: ϑ (a); and η (b) on the Nusselt number in the channel of ICT1.

7.2.2 New Nusselt number correlations

For single-phase, fully developed and turbulent flows, the following new correlations for the Nusselt number in the ICT1 ducts are proposed:

for the core region:

$$Nu_{cr} = m_1 \mathrm{Re}_h^{m_2} \, (\gamma)^{m_3-\varphi} (\beta_e)^{m_4} \, \mathrm{Pr}^{0.3} \tag{7.12}$$

for the channel:

$$Nu_{ch} = m_5 \, \mathrm{Re}_h^{m_6} (\eta)^{m_7} (\beta_e)^{m_8} \, \mathrm{Pr}^{0.4} \tag{7.13}$$

Here m_1 to m_8 are the coefficients evaluated by the regression analysis in a similar way as described in Section 7.1.2. This evaluation was performed based on the Nusselt numbers obtained from the CFD simulations. The obtained coefficients (m_1 to m_8) and geometrical parameter ranges are presented in Table 7.2.

It should be mentioned that the Nusselt number correlations represented by Eqs. (7.12) and (7.13) include a different geometrical parameter than that used in the correlations for the friction factor, Eqs. (7.8), (7.9). The latter utilize the hydraulic perimeter, while Eqs. (7.12), (7.13) use the equivalent perimeter (P_e) defined as follows:

$$\beta_e = P_e / r \tag{7.14}$$

Calculation of the equivalent diameter Eq. (4.6) is based only on the perimeter of the fluid faces taking part in heat transfer (cf. Section 5.3.3). In Eqs. (7.12), (7.13), Prandtl number exponents are kept as specified in the formulation given by Dittus and Boelter (1985) for the cold side (0.4) and for the hot side (0.3). For water used as a working fluid, the Prandtl number range is limited to $2 \leq \mathrm{Pr} \leq 10$.

Table 7.2: Summary of coefficients of Eqs. (7.12), (7.13) and geometrical parameter ranges for the Nusselt number

	Core region flow		**Channel flow**	
	$Nu = m_1 \, \mathrm{Re}_h^{m_2} (\gamma)^{m_3 - \varphi} (\beta_e)^{m_4} \, \mathrm{Pr}^{0.3}$		$Nu = m_5 \, \mathrm{Re}_h^{m_6} (\eta)^{m_7} (\beta_e)^{m_8} \, \mathrm{Pr}^{0.4}$	
	$0.5 \leq \gamma \leq 1, \quad 7 \leq \beta_e \leq 12, \quad 0 \leq \varphi \leq 0.40$		$0.5 \leq \eta \leq 1, \quad 1 \leq \beta_e \leq 1.6$	
	$0.2 \leq \psi \leq 0.35$	$0.38 \leq \psi \leq 0.50$	$0.35 \leq \vartheta \leq 0.56$	$0.58 \leq \vartheta \leq 0.70$
m_1	0.0695	0.166	m_5 0.0400	0.020
m_2	0.8120	0.811	m_6 0.8025	0.872
m_3	0.0460	-1.120	m_7 0.5180	0.175
m_4	-0.4550	-1.010	m_8 0.2480	0.180

Figure 7.9 shows a comparison of Nusselt number values for ICT1 ducts obtained by the CFD simulations and by the developed correlations, Eqs. (7.12) and (7.13). The simulated Nusselt numbers are accurately reproduced, within a maximum deviation of ±15% for both the core region and channel of ICT, while nearly 95% of the data falls within a maximum deviation of less than 10%. The validity range for the Reynolds number is $2500 \leq Re_h \leq 15000$ for channel flow and $6000 \leq Re_h \leq 40000$ for core region flow, while the Prandtl number is varied between 2 and 10.

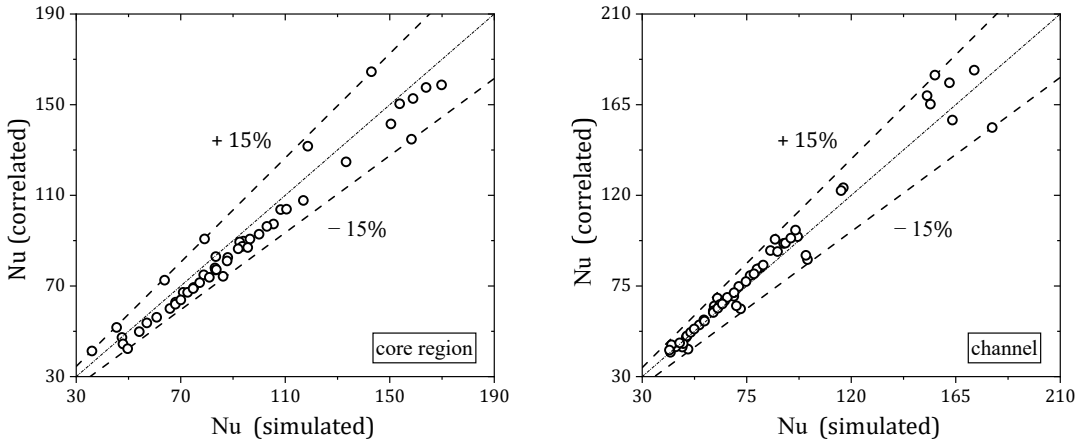

Figure 7.9: Comparison between Nusselt number obtained by simulations of ICT1 and Nusselt numbers calculated by Eq. (7.12) (a) and Eq. (7.13) (b) with coefficients from Table 7.2.

7.3 Evaluation of the ICT2 CFD model using ICT1 correlations

This section presents a comparative analysis of the CFD results for ICT2 and the correlations previously established in Sections 7.1 and 7.2 for ICT1. Given the similarities in design concepts between ICT1 and ICT2 (as detailed in Chapter 4) and their comparable fluid dynamic and heat transfer behaviour (cf. Chapter 6), the correlations developed for ICT1 (Eqs. (7.8), (7.9), (7.12), and (7.13)) were directly applied to the ducts of ICT2. This comparison aims to provide a qualitative evaluation of the feasibility and applicability of the CFD model for ICT2 in capturing the relevant physical phenomena.

The dimensionless parameters for ICT2 were formulated using the same methodology as that applied to ICT1, ensuring a consistent approach for both ICT configurations. These parameters were then applied to the established correlations (Eqs. (7.8), (7.9), (7.12), and

(7.13)), The dimensionless parameters were defined in relation to the inner radius of the tube as follows:

$$\vartheta = (a_3 + s_2)/r \tag{7.15}$$

$$\eta = 2b_3/r \tag{7.16}$$

$$\gamma = 2b_4/r \tag{7.17}$$

$$\psi = (\zeta_2 - a_4)/r \tag{7.18}$$

Here r is a half of the inner diameter (d_1) (cf. Figure 7.10).

In the correlations for the core region, the exponent φ, which represents the ratio of the peripheral distance between two channels in the core region to the inner radius ($\varphi = e/r$), is set to zero. This is because the insulated peripheral spacing between every two channels is eliminated in ICT2 ($e = 0$). As a result, either hydraulic or equivalent diameter can be used when calculating the Nusselt number in the core region (see Figure 7.10):

$$\beta_h = \beta_e = \frac{P_h}{r} = \frac{P_e}{r} \tag{7.19}$$

As illustrated in Figure 7.11, the friction factor values obtained from simulations can be predicted with good accuracy using the proposed equations (Eqs. (7.8) and (7.9)), with a maximum relative deviation of 5%. For the Nusselt number, the deviation is 11% when using the proposed equations (Eqs. (7.12) and (7.13)), as shown in Figure 7.12. Given that the established correlations presented in Sections 7.1.2 and 7.2.2 have an accuracy range of ±7.5% for friction factor and ±15% for Nusselt number, it can be concluded that

simulation results for ICT2 fall well within this accuracy range, validating the reliability of the CFD model.

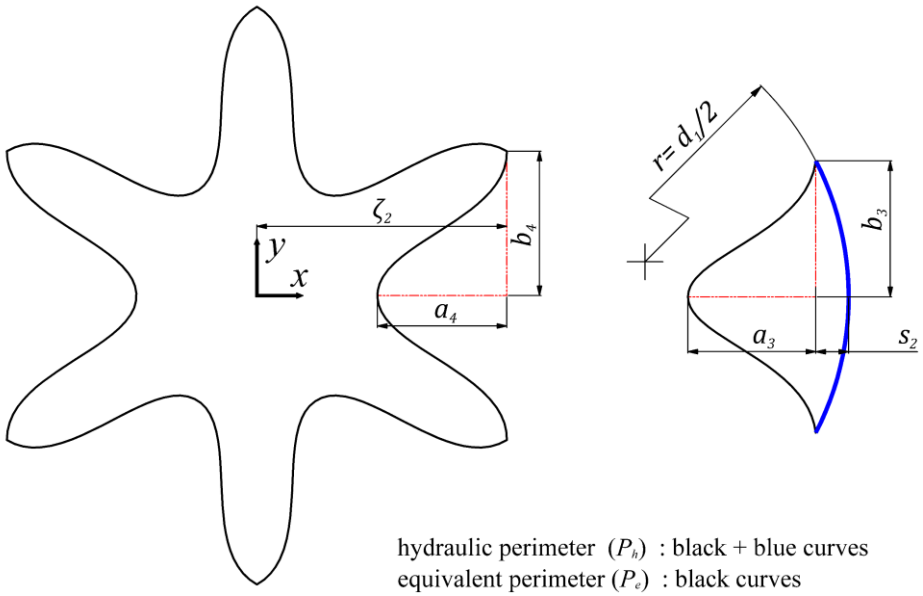

Figure 7.10: Cross-section of the ICT2 ducts with characteristic geometries: core region (left); channel (right).

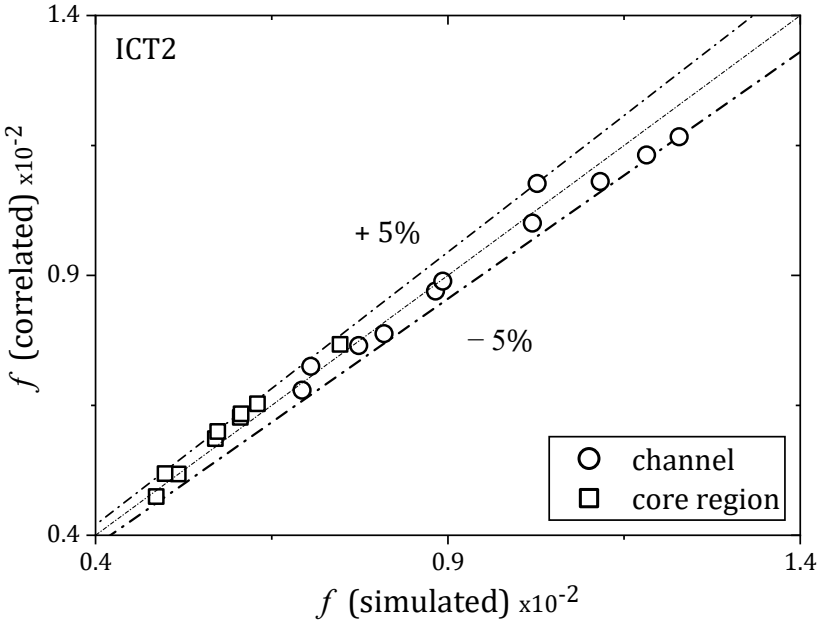

Figure 7.11: Comparison between friction factors obtained by simulations of ICT2 and those calculated by Eqs. (7.8), (7.9).

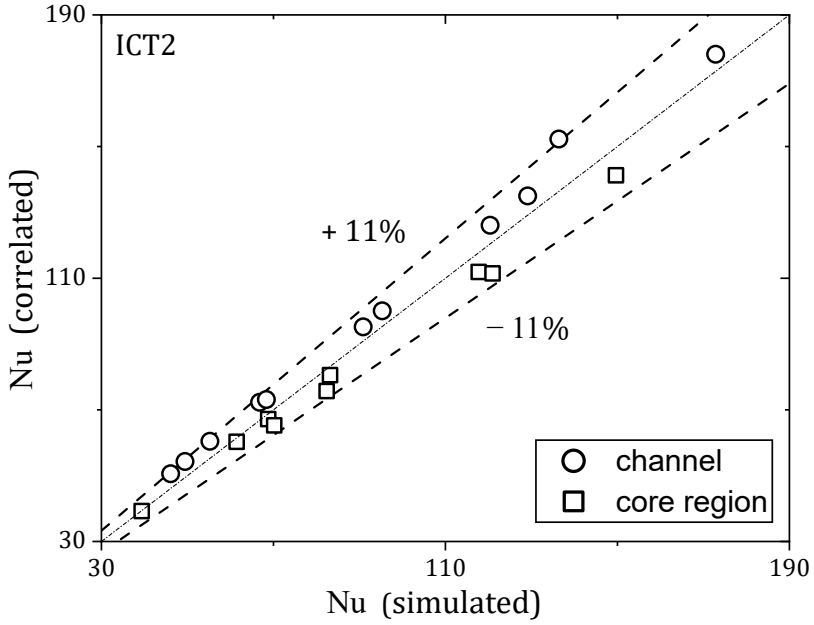

Figure 7.12: Comparison between Nusselt number obtained by simulations of ICT2 and Nusselt numbers calculated by Eqs. (7.12), (7.13).

7.4 Conclusions

In this study, new correlations were developed for predicting friction factors and Nusselt numbers in turbulent forced convection flows within ICT1 ducts. These correlations were derived from numerical data generated using the validated CFD model. They are crucial for designing reliable ICT systems due to the non-circular geometry of the ICT, challenging flow conditions, and insulated outer surface. A sensitivity analysis of the CFD results was conducted to examine the influence of various geometrical parameters of ICT1 ducts on friction factor and Nusselt number. This analysis revealed that certain parameters within the ICT geometry exert a notable impact on both friction factors and Nusselt numbers.

The proposed correlations employ a power-law form that incorporates relevant geometrical parameters. The inclusion of geometrical parameters enables accurate representation of flow and heat transfer behavior in complex duct geometries. Comparison between the correlated friction factor and the CFD data showed a maximum deviation of 7.5% in the core region flow and 7% in the channel flow. For the Nusselt number, the maximum deviation in both ICT1 ducts was 15%. The correlations are valid for broad ranges of ICT1 geometrical parameters and Reynolds numbers.

Given the similar design concept between the two ICT configurations, the CFD results for ICT2 were compared with the developed correlations for ICT1 to evaluate the feasibility of the CFD model applied to ICT2. The dimensionless parameter combinations for ICT2 were determined using the same methodology as applied to ICT1. The results revealed maximum deviations of 5% for the friction factor and 11% for the Nusselt number between simulated and correlated values. Both deviations fall within acceptable limits of the established correlations, suggesting that the correlations can be effectively applied to ICT2.

8 Conclusions

This study includes both numerical and experimental investigations to explore the fluid dynamics and heat transfer characteristics of a novel design concept, so-called internally channeled tube (ICT) heat exchanger. The ICT design is based on a tubular geometry fitted with specially designed curved channels along the tube length. This configuration enhances thermal performance and enables a more compact heat exchanger, offering a promising alternative to traditional equipment. The numerical study formed the core of this work. Experiments, meanwhile, were primarily conducted for validation and to identify flow characteristics and maldistribution in the ICT ducts, what CFD could not easily resolve. Both numerical and experimental studies were conducted under turbulent and laminar flow conditions.

The ICT concept was realized through an iterative design process using preliminary CFD analysis. This led to the definition of two different geometries of ICTs, namely ICT1 and ICT2. Each geometry was precisely defined by mathematical functions that describe the shape of the channels. These functions enabled accurate calculation of key geometrical parameters such as cross-sectional areas and perimeters.

CFD analysis of fluid dynamics and heat transfer in the ICTs was conducted using the commercial software ANSYS-Fluent. Steady-state simulations were employed to model single-phase flow and conjugate heat transfer, using a novel approach based on fluid domain splitting. This method partitions the original 1-meter ICT domain into three elements, significantly reducing the computational domain size and associated demands.

The validity of this innovative approach was successfully verified by comparing its results with simulations of the full-length domain, demonstrating consistent accuracy.

For experimental investigations, the ICT1 heat exchanger was fabricated using an extrusion method. This method enables the production of objects with complex cross-sections, highly precise geometrical details, and smooth surfaces. Before performing the thermal-hydraulic evaluation of ICT1, two preliminary experiments were carried out. The first experiment focused on measuring flow maldistribution to assess the efficiency of the designed headers, which play a crucial role in ensuring uniform fluid distribution across the channels. Each header branch supplied fluid to three channels, with the mid-channel exhibiting a 1% higher flow rate than the left and right channels at high Reynolds numbers, increasing up to 4% at a Re =1700 and exceeding 4% for Re < 1000.To ensure data reliability, experiments on thermal-hydraulic evaluation were conducted at Reynolds numbers of 1000 and above, as small flowrate variations at higher Reynolds numbers minimally affect ICT1 performance. Larger differences—typically observed below 1000—may significantly impact heat transfer, especially at low flow rates where some channels may receive insufficient fluid. The second experiment was performed to characterize flow regimes within the ICT1 ducts by measuring pressure drop. It revealed that the critical Reynolds number in the core region was 1800, while in channel flow it was 2000. For a Reynolds number below the critical value, laminar conditions dominate.

The CFD results were successfully validated against experimental data using two set-up configurations designed to measure pressure drop and temperatures in the ICT1 exchanger: one configuration for turbulent flow and the other for laminar flow. The validation revealed that the maximum deviation between the experimental and simulated pressure drop values was 6.5% for turbulent flow and 11% for laminar flow. For heat transfer, the maximum average deviations between measured temperatures and simulated values were up to 5% for turbulent flow and 8% for laminar flow. Based on this reasonable agreement, the CFD model can be considered capable of effectively capturing fluid dynamic behavior and thermal performance in both ICT ducts under turbulent and laminar flow conditions.

Furthermore, the numerical study revealed that the ICT heat exchangers offer a notable enhancement in thermal performance compared to traditional Double Pipe Heat Exchangers (DPHE). The ICTs exhibited significantly higher heat transfer rates, with ICT1

generally outperforming ICT2, although this comes with a trade-off of increased pressure drop. Performance Evaluation Criterion (PEC) analysis confirmed the superior overall efficiency of the ICTs, with PEC values exceeding 1 across all tested cases and reaching maximums of 1.64 in turbulent flow and 2.3 in laminar flow for ICT1. The improved heat transfer is attributed to the increased contact area between hot and cold fluids, while the increased pressure drop results from the larger internal wall surface area. These findings demonstrate that ICTs offer a promising solution for heat exchanger applications, particularly where enhanced heat transfer performance offsets the increased pumping power demands.

The ICT heat exchanger is an innovative and promising design concept; however, the lack of established design methods may hinder its practical application. Because of the non-circular geometry of ICT and the presence of an insulated outer surface, its rigorous description under typically complex flow conditions presents a considerable challenge. To address this issue, new correlations for pressure drop and heat transfer characteristics in ICT1 ducts were developed specifically for turbulent forced convection. The correlations were derived from extensive CFD simulation results obtained using the developed CFD model, which was validated against experimental data. A sensitivity analysis of the CFD results was carried out to find relevant geometrical parameters of ICT1 ducts to be included in the correlations for the friction factor and Nusselt number. The developed correlations demonstrated maximum deviations of 7.5 % from the numerical results for the friction factor; for the Nusselt number, this value is 15 %. They effectively cover a broad range of ICT geometrical parameters and Reynolds numbers. Furthermore, when comparing the developed correlations with CFD results for ICT2, which is based on the same design concept as ICT1, the comparison demonstrated maximum deviations of 5% for the friction factor and 11% for the Nusselt number. These deviations fall within an acceptable accuracy range, suggesting that the developed correlations have potential for practical use for both ICT designs.

The ICT heat exchangers can offer promising solutions for a wide range of thermal management challenges in both domestic and industrial applications (e.g., waste heat recovery, solar energy systems, and space-constrained HVAC installations). Their potential for high-performance operation makes them particularly well-suited for many applications. This versatility highlights the need for further research into the ICT heat

exchangers, as they could play a significant role in addressing the thermal management demands of diverse applications.

Future research should focus on advancing the design and manufacturing processes of the ICT heat exchangers. Increasing the channel number to eight or ten could enhance compactness and thermal performance. Additionally, the development of tube-bank configurations may reduce the length of the ICTs, making them more suitable for compact installations while improving their economic feasibility. Shortening ICT lengths could also streamline the extrusion process, enhancing cost-effectiveness. These innovations will optimize the ICT heat exchangers for a variety of applications, leading to improvements in energy efficiency and thermal control across different operational environments.

References

Abdul-Jawwad, A. K., & Bashir, A. A comprehensive model for predicting profile exit temperature of industrially extruded 6063 aluminum alloy. Materials and Manufacturing Processes. 26 (2011). pp. 193–201. https://doi.org/10.1080/10426914.2010.505618

Ackermann, R. A. Regenerative heat exchanger theory, in: Cryogenic regenerative heat exchangers. Springer, Boston, MA. (1997). https://doi.org/10.1007/978-1-4757-9891-3_2

Afgan, N., & Da Graça Carvalho, M. Sustainability assessment of heat exchanger design, in: Sustainable assessment method for energy systems. (1st ed.). Springer, New York. (2000). pp. 127–138. https://doi.org/10.1007/978-1-4615-4479-1_6

Ali, Z., Tyacke, J., Tucker, P. G., & Shahpar, S. Block topology generation for structured multi-block meshing with hierarchical geometry handling. Procedia Engineering. 163 (2016). pp. 212–224. https://doi.org/10.1016/j.proeng.2016.11.050

Al-Lami, A. J., Inguva, V., & Kenig, E. Y. Numerical analysis of conjugate heat transfer within internally channeled tubes. Applied Thermal Engineering. 223 (2023). pp. 1–15. https://doi.org/10.1016/j.applthermaleng.2022.119596

Al-Lami, A. J., & Kenig, E. Y. Experimental study of an internally channeled tube heat exchanger under turbulent flow conditions. International Journal of Heat and Mass Transfer. 214 (2023). pp. 1–10. https://doi.org/10.1016/j.ijheatmasstransfer.2023.124425

Al-Mamun, M. R., Roy, H., Islam, M. S., Ali, M. R., Hossain, M. I., Saad Aly, M. A., Khan, M. Z. H., Marwani, H. M., Islam, A., Haque, E., Rahman, M. M., & Awual, M. R. State-of-the-art in solar water heating (SWH) systems for sustainable solar energy utilization: A comprehensive review. Solar Energy. 264 (2023). https://doi.org/10.1016/j.solener.2023.111998

Al-Sammarraie, A. T., & Vafai, K. Thermal-hydraulic performance analysis of a convergent double pipe heat exchanger. ASME Journal of Heat and Mass Transfer. 141 (2019). pp. 51001. https://doi.org/10.1115/1.4042487

Anderson, J. D. Computational fluid dynamics: the basics with applications. (1st ed.). McGraw-Hill Inc., New York. (2010). pp. 1-547.

ASM Handbook-ASM International. Properties and selection: Nonferrous alloys and special-purpose materials. (10th ed.). (1990). pp. 62-122. https://doi.org/10.31399/asm.hb.v02.9781627081627

Aupoix, B. Statistical theory and modeling for turbulent flows. Journal of Turbulence. 3 (2002). https://doi.org/10.1088/1468-5248/3/1/703

Azadeh, G. Nano and bio heat transfer and fluid flow. (1st ed.). Academic Press. (2017). pp. 1-162.

Azam, M. W., Cattani, L., Malavasi, M., & Bozzoli, F. Experimental study of the corrugation profile effect on the local heat transfer coefficient. Energies. 16 (2023). pp. 1–21. https://doi.org/10.3390/en16207181

Baker, A. J. Finite element computational fluid mechanics. (1st ed.). McGraw Hill Higher Education. (1983). pp. 1-510.

Balaji, C., Srinivasan, B., & Gedupudi, S. Heat exchangers, in: Heat transfer engineering fundamentals and techniques. (1st ed.). Academic Press. (2020). pp. 199-231. https://doi.org/10.1016/B978-0-12-818503-2.00007-1

Balaras, C. A. A review of augmentation techniques for heat transfer surfaces in single-phase heat exchangers. Energy. 15 (1990). pp. 899–906. https://doi.org/10.1016/0360-5442(90)90071-9

Bern, M., & Plassmann, P. Mesh generation, in: Handbook of computational geometry. North-Holland. (2000). pp. 291–332. https://doi.org/10.1016/B978-044482537-7/50007-3

Bird, R. B., Warren, E. & Edwin N. Lightfoot. Transport phenomena. (2nd ed.). Wiley. (2007). pp. 1-928.

Blazek, J. Turbulence modeling, in: Computational fluid dynamics: principles and applications. (3rd ed.). Butterworth-Heinemann. (2015). pp. 213-252. https://doi.org/10.1016/B978-0-08-099995-1.00007-5

Branco, J. F., Pinho, C., & Figueiredo, R. d. A. From a power-law equation for the friction factor in smooth pipes to a controversy on the overlap layer. The 6th International Conference on Energy and Environment Research. Brazil. pp. 1-8.

Brodnianská, Z., & Kotšmíd, S. Heat transfer enhancement in the novel wavy shaped heat exchanger channel with cylindrical vortex generators. Applied Thermal Engineering. 220 (2023). pp. 119720. https://doi.org/10.1016/j.applthermaleng.2022.119720

Brogan, R. J. Heat exchangers. Thermopedia. (2011). (accessed: 10.12.2023). https://www.thermopedia.com/content/1121/

Canli, E., Ates, A., & Bilir, Ş. Developing turbulent flow in pipes and analysis of entrance region. Academic Platform Journal of Engineering and Smart Systems. 9 (2021). pp. 332–353. https://doi.org/10.21541/apjes.818717

Chen, X., & Han, P. A note on the solution of conjugate heat transfer problems using SIMPLE-like algorithms. International Journal of Heat and Fluid Flow. 21 (2000). pp. 463–467. https://doi.org/10.1016/S0142-727X(00)00028-X

Christopher, G., & Weller, H. Notes on computational fluid dynamics: general principles. CFD Direct Ltd. (2022). pp. 1- 314.

Coker, A. K. Petroleum refining design and applications handbook. (1st ed., Vol. 5). Wiley & Scrivener. (2023). pp. 1-1053. https://doi.org/10.1002/9781119827696

Cole, K. D. Heat transfer from a flush-mounted heat source-limiting cases and the conjugate Peclet number. ASME 1996 International Mechanical Engineering Congress and Exposition. November 17–22, 1996. Atlanta, Georgia, USA. pp. 145-157. https://doi.org/10.1115/IMECE1996-1347

Dastbelaraki, A. H., Yaghoubi, M., Tavakol, M. M., & Rahmatmand, A. Numerical analysis of convection heat transfer from an array of perforated fins using the Reynolds averaged Navier–Stokes equations and large-eddy simulation method. Applied Mathematical Modelling. 63 (2018). pp. 660–687. https://doi.org/10.1016/J.APM.2018.06.005

Davidson, P. A. Turbulence: An introduction for scientists and engineers. (2nd ed.). Oxford University Press, UK. (2004).

Dirker, J., & Josua, P. M. Heat transfer coefficients in concentric annuli. ASME Journal of Heat and Mass Transfer. 124 (2002). pp. 1200–1203. https://doi.org/10.1115/1.1517266

Dittus, F. W., & Boelter, L. M. Heat transfer in automobile radiators of the tubular type. International Communications in Heat and Mass Transfer. 12 (1985). pp. 3–22. https://doi.org/10.1016/0735-1933(85)90003-X

Drew, T., & McAdams, W. The friction factor for clean round pipe. American Institute of Chemical Engineers (AIChE). 28 (1932). pp. 56–72.

Duan, L., Xiang Ling, & Peng, H. Flow and heat transfer characteristics of a double-tube structure internal finned tube with blossom shape internal fins. Applied Thermal Engineering. 128 (2018). pp. 1102–1115. https://doi.org/10.1016/j.applthermaleng.2017.09.026

Duan, Z. New correlative models for fully developed turbulent heat and mass transfer in circular and noncircular ducts. ASME Journal of Heat Transfer. 134 (2012). https://doi.org/10.1115/1.4004855

Duan, Z., & Yovanovich, M. M. Pressure drop for laminar flow in microchannels of arbitrary cross-sections. 25th Annual IEEE Semiconductor Thermal Measurement and Management Symposium. (2009). pp. 111–120. https://doi.org/10.1109/STHERM.2009.4810751

Duarte, J. P., & Corradini, M. L. Hydraulic and heated equivalent diameters used in heat transfer correlations. Nuclear Technology. 201 (2018). pp. 99–102. https://doi.org/10.1080/00295450.2017.1389594

Eiamsaard, S., Thianpong, C., & Promvonge, P. Experimental investigation of heat transfer and flow friction in a circular tube fitted with regularly spaced twisted tape elements. International Communications in Heat and Mass Transfer. 33 (2006). pp. 1225–1233. https://doi.org/10.1016/j.icheatmasstransfer.2006.08.002

Emrich, W. Principles of nuclear rocket propulsion. (1st ed.). Elsevier Inc. (2016). https://doi.org/10.1016/C2015-0-02220-1

Esmaeilzadeh, E., Almohammadi, H., Nokhosteen, A., Motezaker, A., & Omrani, A. Study on heat transfer and friction factor characteristics of γ-Al2O3/water through circular tube with twisted tape inserts with different thicknesses. International Journal of Thermal Sciences. 82 (2014). pp. 72–83. https://doi.org/10.1016/j.ijthermalsci.2014.03.005

Everts, M., Mahdavi, M., Meyer, J. P., & Sharifpur, M. Development of the hydrodynamic and thermal boundary layers of forced convective laminar flow through a horizontal tube with a constant heat flux. International Journal of Thermal Sciences. 186 (2023). pp. 1–21. https://doi.org/10.1016/J.IJTHERMALSCI.2022.108098

Evstigneev, N. M. On the classification of the laminar-turbulent transition process using the methods of nonlinear dynamics: general analysis and the future. Journal of Physics: Conference Series. 1698 (2020). pp. 1–14. https://doi.org/10.1088/1742-6596/1698/1/012022

Fan, J. F., Ding, W. K., Zhang, J. F., He, Y. L., & Tao, W. Q. A performance evaluation plot of enhanced heat transfer techniques oriented for energy-saving. International Journal of Heat and Mass Transfer. 52 (2009). pp. 33–44. https://doi.org/10.1016/j.ijheatmasstransfer.2008.07.006

Feng, Z., Luo, X., Guo, F., Li, H., & Zhang, J. Numerical investigation on laminar flow and heat transfer in rectangular microchannel heat sink with wire coil inserts. Applied Thermal Engineering. 116 (2017). pp. 597–609. https://doi.org/10.1016/j.applthermaleng.2017.01.091

Forsberg, C. H. Heat exchangers, in: Heat transfer principles and applications. (1st ed.). Academic Press. (2021). pp. 305-341. https://doi.org/10.1016/B978-0-12-802296-2.00008-1

García, A., Vicente, P. G., & Viedma, A. Experimental study of heat transfer enhancement with wire coil inserts in laminar-transition-turbulent regimes at different Prandtl numbers. International Journal of Heat and Mass Transfer. 48 (2005). pp. 4640–4651. https://doi.org/10.1016/j.ijheatmasstransfer.2005.04.024

Ghani, S., Gamaledin, S. M. A., Rashwan, M., & Atieh, M. A. Experimental investigation of double-pipe heat exchangers in air conditioning applications. Energy and Buildings. 158 (2018). pp. 801–811. https://doi.org/10.1016/J.ENBUILD.2017.10.051

Glycerine Producers Association. Physical properties of glycerin and its solutions. (1975). pp. 1-27.

Gnielinski, V. New equations for heat and mass transfer in turbulent pipe and channel flow. International Chemical Engineering. 16 (1976). pp. 359–368). https://ci.nii.ac.jp/naid/10024972801/

Guo, C., Lan, M., Li, M., Tang, S., Zhang, D., Song, J., & Li, H. H. Studying the advantages of equal curvature curved fin to enhance phase change heat storage. Journal of Energy Storage. 57 (2023). pp. 2–18. https://doi.org/10.1016/j.est.2022.106212

Hanshik, C., Jeong, H., Jeong, K. W., & Choi, S. H. Improved productivity of the MSF (multi-stage flashing) desalination plant by increasing the TBT (top brine temperature). Energy. 107 (2016). pp. 683–692. https://doi.org/10.1016/j.energy.2016.04.028

Harleß, A., Franz, E., & Breuer, M. Heat transfer and friction characteristics of fully developed gas flow in cross-corrugated tubes. International Journal of Heat and Mass Transfer. 107 (2017). pp. 1076–1084. https://doi.org/10.1016/j.ijheatmasstransfer.2016.10.129

Hensley, J. C. Cooling tower fundamentals. (2nd ed.). SPX cooling Technologies, Kansas, USA. (2009). pp. 1-117.

Herraiz, L., Hogg, D., Cooper, J., Gibbins, J., & Lucquiaud, M. Reducing water usage with rotary regenerative gas/gas heat exchangers in natural gas-fired power plants with post-combustion carbon capture. Energy. 90 (2015). pp. 1994–2005. https://doi.org/10.1016/J.ENERGY.2015.07.032

Hesselgreaves, J. E. Compact heat exchangers: selection, design, and operation. (1st ed.). Elsevier Science and Technology Books, NY, USA. (2001). pp. 1-398.

Jing, H., Quan, Z., Zhao, Y., Wang, L., Ren, R., & Liu, Z. Thermal performance and energy saving analysis of indoor air–water heat exchanger based on micro heat pipe array for data center. Energies. 13 (2020). pp. 1–24. https://doi.org/10.3390/en13020393

Jokar, S. M., Rahimpour, M. R., & Shariati, A. Heat exchanger application for environmental problem-reducing in flare systems of an oil refinery and a petrochemical plant: Two case studies. Applied Thermal Engineering. 106 (2016). pp. 796–810. https://doi.org/10.1016/j.applthermaleng.2016.06.050

Jouhara, H., Khordehgah, N., Almahmoud, S., Delpech, B., Amisha Chauhan, & Tassou, S. Waste heat recovery technologies and applications. Thermal Science and Engineering Progress. 6 (2018). pp. 268–289. https://doi.org/10.1016/j.tsep.2018.04.017

Kadam, S. V., Patil, S. S., & Mohite, S. S. Numerical analysis of wire coil inserted corrugated tube for laminar flow. Materials Tody: Proceedings. 62 (2022). pp. 6837–6843. https://doi.org/10.1016/j.matpr.2022.05.021

Kader, B. A. Temperature and concentration profiles in fully turbulent boundary layers. International Journal of Heat and Mass Transfer. 24 (1981). pp. 1541–1544. https://doi.org/10.1016/0017-9310(81)90220-9

Kadoch, B., Bos, W. J. T., Schneider, K., & Bos, W. J. Efficiency of laminar and turbulent mixing in wall-bounded flows. Physical Review E. 101 (2020). pp. 1–8. https://doi.org/10.1103/PhysRevE.101.043104

Kanaś, P., Jedlikowski, A., Karpuk, M., Anisimov, S., & Vager, B. Heat transfer in the regenerative heat exchanger. Applied Thermal Engineering. 215 (2022). pp. 118922. https://doi.org/10.1016/j.applthermaleng.2022.118922

Karimi, S., Heyhat, M. M., Isfahani, A. H. M., & Hosseinian, A. Experimental investigation of convective heat transfer and pressure drop of SiC/water nanofluid in a shell and tube heat exchanger. Heat and Mass Transfer. 56 (2020). pp. 2325–2331. https://doi.org/10.1007/s00231-020-02844-7

Katz, A., & Sankaran, V. Mesh quality effects on the accuracy of CFD solutions on unstructured meshes. Journal of Computational Physics. 230 (2011). pp. 7670–7686. https://doi.org/10.1016/J.JCP.2011.06.023

Kim, S. Y., Shin, D. H., Kim, C. S., Park, G. C., & Cho, H. K. Flow visualization experiment in a two-side wall heated rectangular duct for turbulence model assessment in natural convection heat transfer. Nuclear Engineering and Design. 341 (2019). pp. 284–296. https://doi.org/10.1016/j.nucengdes.2018.11.012

Kline, S. J., & McClintock, F. A. Description of uncertainties in single sample experiments. Mechanical Engineering. 17 (1953). pp. 3–8.

Komfovent. Rotary heat exchangers. (2018). (accessed: 28/02/2025). https://www.komfovent.com/en/news/products/komfovent-rotary-heat-exchangers-59

Kumaran, R. M., Kumaraguruparan, G., & Sornakumar, T. Experimental and numerical studies of header design and inlet/outlet configurations on flow mal-distribution in parallel micro-channels. Applied Thermal Engineering. 58 (2013). pp. 205–216. https://doi.org/10.1016/j.applthermaleng.2013.04.026

Legros, A., Guillaume, L., Diny, M., Zaïdi, H., & Lemort, V. Comparison and impact of waste heat recovery technologies on passenger car fuel consumption in a normalized driving cycle. Energies. 7 (2014). pp. 5273–5290. https://doi.org/10.3390/en7085273

Liebenberg, L., & Meyer, J. P. In-tube passive heat transfer enhancement in the process industry. Applied Thermal Engineering. 27 (2007). pp. 2713–2726. https://doi.org/10.1016/j.applthermaleng.2007.06.003

Lienhard, J. H. A Heat Transfer Textbook. (6th ed.). Cambridge Massachusetts, Houston. (2020). pp. 1-784). http://ahtt.mit.edu

Liu, W., Xu, G., Fu, Y., Wen, J., & Zhang, N. Numerical investigation on forced, natural, and mixed convective heat transfer of n-decane in laminar flow at supercritical pressures. International Journal of Heat and Mass Transfer. 209 (2023). https://doi.org/10.1016/J.IJHEATMASSTRANSFER.2023.124129

Liu, X., & Jensen, M. K. Geometry effects on turbulent flow and heat transfer in internally finned tubes. ASME Journal of Heat and Mass Transfer. 123 (2001). pp. 1035–1044. https://doi.org/10.1115/1.1409267

Lu, C., Huang, J., Nien, W. C., & Wang, C. A numerical investigation of the geometric effects on the performance of plate finned-tube heat exchanger. Energy Conversion and Management. 52 (2011). pp. 1638–1643. https://doi.org/10.1016/j.enconman.2010.10.026

Luna, N., Endez, F. M., & Trevi, C. Conjugated heat transfer in circular ducts with a power-law laminar convection fluid flow. International Journal of Heat and Mass Transfer. 45 (2002). pp. 655–666. https://doi.org/10.1016/S0017-9310(01)00147-8

Luyben, W. L. Series versus parallel reboilers in distillation columns. Chemical Engineering Research and Design. 133 (2018). pp. 294–302. https://doi.org/10.1016/j.cherd.2018.03.025

Ma, T., Lin, M., Zeng, M., Ji, Y. P., & Wang, Q. W. Numerical study of internally finned bayonet tubes in a high temperature bayonet tube heat exchanger with inner and outer fins. ASME Turbo Expo: Power for Land, Sea, and Air. 5 (2010). pp. 329–338. https://doi.org/10.1115/GT2010-22360

Maradiya, C., Vadher, J., & Agarwal, R. The heat transfer enhancement techniques and their thermal performance factor. Beni-Suef University Journal of Basic and Applied Sciences. 7 (2018). pp. 1–21. https://doi.org/10.1016/j.bjbas.2017.10.001

Mehendale, S. Single-phase heat exchangers, in: Handbook of thermal science and engineering. (1st ed.). Springer. (2018). pp. 1447–1472. https://doi.org/10.1007/978-3-319-26695-4_21

Mousa, M. H., Miljkovic, N., & Nawaz, K. Review of heat transfer enhancement techniques for single phase flows. Renewable and Sustainable Energy Reviews. 137 (2021). pp. 110566. https://doi.org/10.1016/J.RSER.2020.110566

Mridha, R. H., & Hasanuzzaman, M. Heat exchanger for solar thermal energy, in: Technologies for solar thermal energy; theory, design, and optimization. (1st ed.). Academic Press. (2022). pp. 55–91. https://doi.org/10.1016/B978-0-12-823959-9.00009-X

Muzychka, Y. S., & Yovanovich, M. M. Pressure drop in laminar developing flow in noncircular ducts: A scaling and modeling approach. Journal of Fluids Engineering. 131 (2009). pp. 1–11. https://doi.org/10.1115/1.4000377

Muzychka, Y. S., & Yovanovich, M. M. Modeling Nusselt numbers for thermally developing laminar flow in non-circular ducts. 7th AIAA/ASME Joint Thermophysics and Heat Transfer Conference. 15-18 June 1998. Albuquerque, NM, USA. https://doi.org/10.2514/6.1998-2586

Navickaitė, K., Cattani, L., Bahl, C. R., & Engelbrecht, K. Elliptical double corrugated tubes for enhanced heat transfer. International Journal of Heat and Mass Transfer.

128 (2019). pp. 363–377. https://doi.org/10.1016/j.ijheatmasstransfer.2018.09.003

Nazif, H. R., & Tabrizi, H. B. Applying a non-equilibrium wall function in k–ε turbulent modelling of hydrodynamic circulating flow. Applied Mathematical Modelling. 38 (2014). pp. 588–598. https://doi.org/10.1016/J.APM.2013.06.038

Nikuradse, J. Laws of flow in rough pipes. NACA. (1950). pp. 1–62.

Niroomand, R., Saidi, M. H., & Hannani, S. K. A new multiscale modeling framework for investigating thermally-induced flow maldistribution in multi-stream plate-fin heat exchangers. International Journal of Heat and Mass Transfer. 180 (2021). pp. 1–17. https://doi.org/10.1016/j.ijheatmasstransfer.2021.121779

Pal, S., & Saha, S. K. Laminar fluid flow and heat transfer through a circular tube having spiral ribs and twisted tapes. Experimental Thermal and Fluid Science. 60 (2015). pp. 173–181. https://doi.org/10.1016/j.expthermflusci.2014.09.005

Parisher, R. A., & Rhea, R. A. Mechanical equipment, in: Pipe Drafting and Design. (4th ed.). Gulf Professional Publishing. (2022). pp. 119–153. https://doi.org/10.1016/B978-0-12-822047-4.00011-X

Patankar, S. V. Numerical heat transfer and fluid flow. (1st ed.). CRC Press, Boca Raton. (2018). pp. 1-214. https://doi.org/10.1201/9781482234213

Petukhov, B. S. Heat transfer and friction in turbulent pipe flow with variable physical properties. Advances in Heat Transfer. 6 (1970). pp. 503–564. https://doi.org/10.1016/S0065-2717(08)70153-9

Piper, M., Zibart, A., Djakow, E., Springer, R., Homberg, W., & Kenig, E. Y. Heat transfer enhancement in pillow-plate heat exchangers with dimpled surfaces: A numerical study. Applied Thermal Engineering. 153 (2019). pp. 142–146. https://doi.org/10.1016/j.applthermaleng.2019.02.082

Piper, M., Zibart, A., & Kenig, E. Y. New design equations for turbulent forced convection heat transfer and pressure loss in pillow-plate channels. International Journal of Thermal Sciences. 120 (2017). pp. 459–468. https://doi.org/10.1016/j.ijthermalsci.2017.06.012

Pope, S. B. Turbulent flows. (1st). Cambridge University Press, Cambridge. (2000). pp. 1- 802.

Promvonge, P., Suwannapan, S., Pimsarn, M., & Thianpong, C. Experimental study on heat transfer in square duct with combined twisted-tape and winglet vortex generators. International Communications in Heat and Mass Transfer. 59 (2014). pp. 158–165. https://doi.org/10.1016/j.icheatmasstransfer.2014.10.005

Rahimi, M., Shabanian, S. R., & Alsairafi, A. A. Experimental and CFD studies on heat transfer and friction factor characteristics of a tube equipped with modified twisted tape inserts. Chemical Engineering and Processing: Process Intensification. 48 (2009). pp. 762–770. https://doi.org/10.1016/j.cep.2008.09.007

Rao, G. A., & Levy, Y. A Semi Empirical Methodology for Performance Estimation of a Double Pipe Finned Heat Exchanger. ASME 2008 9th Biennial Conference on Engineering Systems Design and Analysis. July 7–9, 2008. Haifa, Israel. pp. 167–177. https://doi.org/10.1115/ESDA2008-59124

Reppich, M. Use of high-performance plate heat exchangers in chemical and process industries. International Journal of Thermal Sciences. 38 (1999). pp. 999–1008. https://doi.org/10.1016/S1290-0729(99)00109-X

Reynolds, A. J. The prediction of turbulent Prandtl and Schmidt numbers. International Journal of Heat and Mass Transfer. 18 (1975). pp. 1055–1069. https://doi.org/10.1016/0017-9310(75)90223-9

Roache, P. J. Computational fluid dynamics. (6th ed.). Hermosa Pub, Michigan, USA. (1976). pp. 446.

Rozzi, S., Massini, R., Paciello, G., Pagliarini, G., Rainieri, S., & Trifirò, A. Heat treatment of fluid foods in a shell and tube heat exchanger: comparison between smooth and helically corrugated wall tubes. Journal of Food Engineering. 79 (2007). pp. 249–254. https://doi.org/10.1016/j.jfoodeng.2006.01.050

Saha, S., & Saha, S. K. Thermal and friction characteristics of laminar flow through rectangular and square ducts with transverse ribs and wire coil inserts. Experimental Thermal and Fluid Science. 34 (2010). pp. 63–72. https://doi.org/10.1016/j.expthermflusci.2009.09.003

Sahin, B. A Taguchi approach for determination of optimum design parameters for a heat exchanger having circular-cross sectional pin fins. Heat and Mass Transfer. 43 (2007). pp. 493–502. https://doi.org/10.1007/s00231-006-0224-5

Savaş, A. F., & Kocabas, C. Reducing surface heat loss in steam boilers. Open Chemistry. 20 (2022). pp. 1458–1466. https://doi.org/10.1515/chem-2022-0241

Shao, H., Zhang, M., Zhao, Q., Wang, Y., & Liang, Z. Study of improvements on flow maldistribution of double tube-passes shell-and-tube heat exchanger with rectangular header. Applied Thermal Engineering. 144 (2018). pp. 106–116. https://doi.org/10.1016/j.applthermaleng.2018.08.014

Shih, T. H., Liou, W. W., Shabbir, A., & Yang, Z. Z. A new k-ϵ Eddy Viscosity model for high Reynolds number turbulent flows. Computers & Fluids. 24 (1995). pp. 277-238. https://doi.org/10.1016/0045-7930(94)00032-T

SimuTech Group. Mesh optimization with Ansys software. (2020). (accessed: 22.09.2023). https://simutechgroup.com/why-is-meshing-important-for-fea-fluid-simulations

Singh, A., Aravind, S., Srinadhi, K., & Kannan, B. T. Assessment of turbulence models on a backward facing step flow using OpenFOAM. IOP Conference Series: Materials Science and Engineering. pp. 1–8. https://doi.org/10.1088/1757-899X/912/4/042060

Sivashanmugam, P., & Suresh, S. Experimental studies on heat transfer and friction factor characteristics of turbulent flow through a circular tube fitted with regularly spaced helical screw-tape inserts. Applied Thermal Engineering. 27 (2007). pp. 1311–1319. https://doi.org/10.1016/J.APPLTHERMALENG.2006.10.035

SSG AERO - Agile aerodynamic design. Structured meshes. (2017). (accessed: 01.04.2024). https://www.ssg-aero.com/news/archives/10-2017

Stehlik, P., & Jegla, Z. Heat exchangers for waste heat recovery. (1st ed). MDPI AG. (2020). pp. 1-110. https://doi.org/10.3390/books978-3-03936-476-3

Takamura, K., Fischer, H., & Morrow, N. R. Physical properties of aqueous glycerol solutions. Journal of Petroleum Science and Engineering. 98-99 (2012). pp. 50–60. https://doi.org/10.1016/j.petrol.2012.09.003

Templeton, J. D., Hassani, F., & Madiseh, S. A. G. Study of effective solar energy storage using a double pipe geothermal heat exchanger. Renewable Energy. 86 (2016). pp. 173–181. https://doi.org/10.1016/J.RENENE.2015.08.024

Teralba Industries. Industrial monotube heat exchangers. (2024). (accessed: 06.05.2024). https://teralba.com/products/heat-exchangers/dimpleflo-heat-exchangers/dimpleflo-double-tube/industrial-monotube-heat-exchangers/

Torq N Seal Plugs. Scaling in heat exchangers. (2022). (accessed: 15.04.2024). https://www.torq-n-seal.com/scaling-in-heat-exchangers-how-to-remove-and-prevent/

Tuncer, C., & Bradshaw, P. Momentum transfer in boundary layers. (1st ed.). McGraw-Hill Inc.,US. (1977). pp. 1-416.

Vakylabad, A. B. Heat generation and exchange systems safety: furnaces, heat exchangers, reformers, etc., in: Crises in Oil, Gas and Petrochemical Industries. (1st ed.). Elsevier. (2023). pp. 77–124. https://doi.org/10.1016/B978-0-323-95163-0.00001-3

Wang, H., Chen, Z., & Gao, J. Influence of geometric parameters on flow and heat transfer performance of micro-channel heat sinks. Applied Thermal Engineering. 107 (2016). pp. 870–879. https://doi.org/10.1016/j.applthermaleng.2016.07.039

Wang, Q. W., Lin, M., Zeng, M., & Tian, L. Investigation of turbulent flow and heat transfer in periodic wavy channel of internally finned tube with blocked core tube. ASME Journal of Heat and Mass Transfer. 130 (2008). pp. 1–7. https://doi.org/10.1115/1.2891219

Wang, Q. Q., Chen, Q., Chen, G., & Zeng, M. M. Numerical investigation on combined multiple shell-pass shell-and-tube heat exchanger with continuous helical baffles. International Journal of Heat and Mass Transfer. 52 (2009). pp. 1214–1222. https://doi.org/10.1016/j.ijheatmasstransfer.2008.09.009

Wang, W., Zhang, Y., Lee, K., & Li, B. Optimal design of a double pipe heat exchanger based on the outward helically corrugated tube. International Journal of Heat and

Mass Transfer. 135 (2019). pp. 706–716. https://doi.org/10.1016/j.ijheatmasstransfer.2019.01.115

Wang, W., Zhang, Y., Li, Y., Han, H., & Li, B. Numerical study on fully-developed turbulent flow and heat transfer in inward corrugated tubes with double-objective optimization. International Journal of Heat and Mass Transfer. 120 (2018). pp. 782–792. https://doi.org/10.1016/j.ijheatmasstransfer.2017.12.079

Wehbi, Z., Taher, R., Faraj, J., Lemenand, T., Mortazavi, M., & Khaled, M. Waste water heat recovery systems types and applications: Comprehensive review, critical analysis, and potential recommendations. Energy Reports. 9 (2023). pp. 16–33. https://doi.org/10.1016/j.egyr.2023.05.243

Willink, R. An enhanced method for the evaluation of measurement uncertainty. Measurement: Sensors. 24 (2022). pp. 1–16. https://doi.org/10.1016/j.measen.2022.100373

Wolfshtein, M. The velocity and temperature distribution in one-dimensional flow with turbulence augmentation and pressure gradient. International Journal of Heat and Mass Transfer. 12 (1969). pp. 301–318. https://doi.org/10.1016/0017-9310(69)90012-X

Yang, Z., Liu, X., Cao, X., Gao, Z., & Ding, M. Numerical analysis of FLiBe laminar convective heat transfer characteristics in tubes fitted with coaxial cross twisted tape inserts. Frontiers in Energy Research. 8 (2020). https://doi.org/10.3389/fenrg.2020.00178

Zehnder, M. Efficient air-water pumps for high temperature lift residential heating, including oil migration aspects [doctoral thesis]. EPFL, Lausanne University, Switzerland. (2004). https://doi.org/10.5075/epfl-thesis-2998

Zhai, Z. Computational fluid dynamics for built and natural environments. (1st ed.). Springer Singapore. (2020). pp. 1-263. https://doi.org/10.1007/978-981-32-9820-0

Zhang, F., Zhou, Z., Zhang, H., & Yang, X. A new single formula for the law of the wall and its application to wall-modeled large-eddy simulation. European Journal of Mechanics - B/Fluids. 94 (2022). pp. 350–365. https://doi.org/10.1016/j.euromechflu.2022.03.013

Zhang, J., Zhu, X., Mondejar, M. E., & Haglind, F. A review of heat transfer enhancement techniques in plate heat exchangers. Renewable and Sustainable Energy Reviews. 101 (2019). pp. 305–328. https://doi.org/10.1016/J.RSER.2018.11.017

Zhang, L., Guo, H., Wu, J., & Du, W. Compound heat transfer enhancement for shell side of double-pipe heat exchanger by helical fins and vortex generators. Heat and Mass Transfer. 48 (2012). pp. 1113–1124. https://doi.org/10.1007/s00231-011-0959-5

Zhiyin, Y. Large-eddy simulation: Past, present and the future. Chinese Journal of Aeronautics. 28 (2015). pp. 11–24. https://doi.org/10.1016/j.cja.2014.12.007

Zhou, L. Modeling of Single-Phase, in: Theory and modeling of dispersed multiphase turbulent reacting flows. (1st ed.). Butterworth-Heinemann. (2018). pp. 89-120. https://doi.org/10.1016/B978-0-12-813465-8.00005-3

Zibart, A., & Kenig, E. Y. Numerical investigation of conjugate heat transfer in a pillow-plate heat exchanger. International Journal of Heat and Mass Transfer. 165 (2021), 120567. https://doi.org/10.1016/j.ijheatmasstransfer.2020.120567

Zohuri, B. Thermal-hydraulic analysis of nuclear reactors. (2nd ed. 2017). Springer International Publishing; Imprint: Springer. (2017). pp. 835-453.

Zuccato Energia. Waste heat recovery ORC system. (2023). (accessed: 10.04.2024). https://zuccatoenergia.it/orc-system-for-biomass/

Appendix

Appendix A

Published correlations used in Ref. Al-Lami et al. (2023) and applied to both core region and channel ducts of ICTs under turbulent flow conditions.

Table A1

No.	Friction factor correlations	Reference
1	$f = 0.0014 + 0.125\, Re_h^{-0.32}$	(Drew & McAdams, 1932)
2	$\frac{1}{\sqrt{f}} = 4log\left(Re_h\sqrt{f}\right) - 0.4$	(Nikuradse, 1950)
3	$f = [1.58\, ln\, Re_h - 3.28]^{-2}$	(Gnielinski, 1976)
Here: $\mathrm{Re_h} = \frac{u_m D_h}{\nu}$, $\mathrm{Re_A} = \frac{u_m \sqrt{A_{cs}}}{\nu}$, $D_h = \frac{4A_{cs}}{P_h}$		

Table A2

No.	Nusselt number correlations	Reference
1	$Nu_h = \left(\left(\frac{f}{2}\right) Re_h Pr\right) \Big/ \left(1.07 + 12.7\left(\frac{f}{2}\right)^{0.5}\left(Pr^{2/3} - 1\right)\right)$	(Petukhov, 1970)
2	$Nu_h = \left(\frac{f}{2}\right)(Re_h - 1000)Pr \Big/ \left(1 + 12.7\left(\frac{f}{2}\right)^{0.5}\left(Pr^{2/3} - 1\right)\right)$	(Gnielinski, 1976)
3	$Nu_h = 0.024 {Re_h}^{0.8} Pr^n$ n=0.3 (cooling), =0.4 (heating)	(Dittus & Boelter, 1985)
here: $\mathrm{Nu_h} = \frac{h_{avg} \cdot D_h}{\lambda_f}$, $D_h = \frac{4A_{cs}}{P_h}$		

Erklärung zur Zitation von Inhalten aus studentischen Arbeiten

In Ergänzung zu meinem Antrag auf Zulassung zur Promotion in der Fakultät für Maschinenbau der Universität Paderborn erkläre ich gemäß §11 der Promotionsordnung und unter Beachtung der Regelung zur Zitation studentischer Arbeiten:

Die von mir vorgelegte Dissertation habe ich selbstständig verfasst, und **ich habe keine anderen** als die dort angegebenen Quellen und Hilfsmittel benutzt. Es sind **keine Inhalte** studentischen Ursprungs (studentische Arbeiten) in dieser Dissertation enthalten.

Ich habe die verwendeten Arbeiten entsprechend der Regelung „Zitation aus studenti-schen Arbeiten in Dissertationen“ zitiert.

Paderborn, Datum: 25.06.2025